THE FLORIDA STATE UNIVERSITY
COLLEGE OF ARTS AND SCIENCES

DIRECT PHOTON PRODUCTION AND SEARCH FOR EXCITED QUARKS WITH THE DØ DETECTOR

By
ROBERT MADDEN

A Dissertation submitted to the
Department of Physics
in partial fulfillment of the
requirements for the degree of
Doctor of Philosophy

FERMILAB
LIBRARY

Degree Awarded:
Fall Semester, 1995

AAE4757

The members of the Committee approve the Dissertation of ROBERT MADDEN defended on July 31, 1995.

Horst Wahl
Professor Directing Dissertation

Daniel Oberlin
Outside Committee Member

Joseph Owens
Committee Member

Steven Linn
Committee Member

David Lind
Committee Member

This thesis is dedicated to Jesus Christ the Son of God;
a prayer of thanks for my atonement.

ACKNOWLEDGEMENTS

Thank you my parents Wayne and Joyce for your patient and unfailing support, and thank you my sisters Carol and Lori. Thank you Steven Linn and Horst Wahl for your invaluable guidance. Thank you members of my committee; David Lind, Daniel Oberlin, and Joseph Owens. Special thanks Ian Bertram, Mark Paterno, and Harrison Prosper for your advice on the mass fitting analysis. Thank you Ian Adam, Jerry Blazey, Howie Baer, Direct Photon group, Sal Fahey, Larisa Fisher, Florida State HEP group, Steve Jerger, Tim Jones, Asher Klatchko, Robert Mitchell, Freedy Nang, Nance, Henryk Piekarz, Prerna, Eduardo Roa, Paul Rubinov, Lea Shanley, Guoliang Wang, John Womersley, David Zack, and everyone else who helped me to further my education and to complete this work. You are all much appreciated!

CONTENTS

List of Tables ix

List of Figures xi

Abstract xvi

1 Introduction 1

1.1 A Brief History of Particle Physics 1

1.2 Thesis Outline 4

2 Theoretical Background on Excited Quarks 6

2.1 Quark and Lepton Compositeness and Excited States 6

3 The DØ Detector 12

3.1 The Central Tracking System 15

3.1.1 The Vertex Drift Chamber (VTX) 15

3.1.2 The Transition Radiation Detector (TRD) 17

3.1.3 The Central and Forward Drift Chambers (CDC and FDC) . . 20

3.2 The Calorimetry 23

3.2.1 The Central Calorimeter and End Calorimeters (CC and EC) 28

3.2.2 The Intercryostat Detectors (ICD) and Massless Gap Detectors (MG) 36

3.3 The Muon System 36

4 Data Selection 42

4.1 Cross Sections and Luminosity 42

4.2 The DØ Trigger System 46
4.2.1 Level Zero (L0) 46
4.2.2 Level One (L1) 47
4.2.3 Level Two (L2) 48
4.3 Photon Triggers 49
4.4 Offline Event Reconstruction and Storage 54
4.4.1 STA and DST Data Formats 56
4.4.2 Streaming 57
4.4.3 Ntuples 57

5 Offline Analysis **58**
5.1 Geometric Acceptance 59
5.1.1 Fiducial Cuts 59
5.2 Energy Threshold Cuts 61
5.3 Jet cuts 61
5.4 Photon cuts 62
5.5 Additional kinematic cuts 65
5.6 Scattering Angle in the Center of Momentum System (θ^*) 66
5.7 The Photon Purity 74

6 Prompt Photon Analyses at DØ **77**
6.1 Introduction 77
6.2 Inclusive Cross Section 77
6.3 Angular Distribution 82

7 Mass Fitting Analysis **86**
7.1 Introduction 86
7.2 The Invariant Mass Distribution 86

7.3 Efficiency vs. Invariant Mass 88
7.4 Fitting Procedure 91
7.5 Fitting Method 93
7.6 Monte Carlo Simulation of $Q^* \to \gamma q$ 97
7.7 A Function for the Q^* Signal Mass Distribution 99
7.8 A Function for the Background Mass Distribution 99
7.9 Fixing the Parameterization of the Signal Function 103
7.10 Uncertainty in the Parameterization of the Signal Function 109

8 Analysis Observations **111**
8.1 Fitting the Experimental Mass Distribution 111
8.2 Checks on the Reliability of χ^2 Fit Results 111
8.3 Significance of the Number of Observed Signal Events 117

9 Establishing Confidence Limits **120**
9.1 Establishing a Confidence Limit from Frequency Distributions 120
9.2 Bayes' Theorem and Bayes' Postulate 122
9.3 Establishing a Confidence Limit with Bayesian Methods 123
9.4 Confidence Limit Results 125

10 Conclusion **130**

A Introductory Theoretical Background **132**
A.1 Symmetries 132
A.2 Gauges 134
A.3 Spontaneous Symmetry Breaking 135
A.4 The Higgs Mechanism 136
A.5 The Standard Model 137
A.5.1 The Electroweak Sector 137

A.5.2 The Strong Interaction (QCD) 138

Bibliography **141**

Biographical Sketch **150**

LIST OF TABLES

2.1 The branching ratios for Q^* transition interactions, with spin-1/2, $f = f_s = f'$ $(= 1)$, $\alpha_s \approx 0.1$, and $M^* = 1$ TeV 9

3.1 The Central Calorimeter design parameters. 33

3.2 The End Calorimeter design parameters 34

3.3 The muon system design parameters. 41

5.1 Offline analysis cuts with the pass efficiencies for photon events. The last column gives the data source used to estimate the efficiency. The efficiencies for each cut are for a data sample where all previous cuts were also applied. The total efficiencies of all cuts are given in the last row. 66

7.1 The background function parameter values for a χ^2 minimization fit with an exponential function. 101

7.2 The background function parameter values for a χ^2 minimization fit with a double exponential function $B(M) = \exp(A_1 + A_2 M) + \exp(A_3 + A_4 M)$. 103

7.3 Values of the mass, bin contents, statistical error, function $B(M)$, and χ^2 per bin for the fit with a double exponential function $B(M) = \exp(A_1 + A_2 M) + \exp(A_3 + A_4 M)$. 104

7.4 The parameterization of $S(M|M^*)$ from fits to Monte Carlo Q^* decay events plus background. The values of variables $\mathrm{A}(M^*)$, $\mathrm{W}(M^*)$, and $\mathrm{R}(M^*)$ are given for several excited quark masses M^*. Also given are the polynomial functions which fit the parameters between data points, and polynomial functions which fit the error on the paramters as a function of M^*. 107

7.5 Several values of $N(M^*)$ as found in the χ^2 minimization fit with different parameterizations of the signal function $S(M|M^*)$. The change in the parameterization is noted as a subscript on N at the top of each column. The last column is ΔN_{par} as estimated from the standard deviation of the values of N for different parameterizations. The last row is a polynomial fit to all discrete values of ΔN_{par}. 110

A.1 The particles of the Standard Model. 139

LIST OF FIGURES

2.1 Feynman diagram of the process $gq \rightarrow Q^* \rightarrow \gamma q$. 9

3.1 The DØ Detector 14

3.2 The Central Tracking System 15

3.3 The Vertex Chamber 16

3.4 The Transition Radiation Detector 19

3.5 The Central Drift Chamber Modules 21

3.6 The Forward Drift Chambers 22

3.7 A Single Calorimeter Gap Interval (cutaway view) 26

3.8 The Calorimeters 29

3.9 A side view of the calorimeter, showing transverse and longitudinal segmentation. The numbered rays show pseudorapidity intervals. . . . 30

3.10 A foldout view of the calorimeter cell structure in ($\eta \times 10$) vs. R coordinates. The calorimeter layers are labeled on the vertical axis. . 31

3.11 An ECEM module shown in relation to the $p\bar{p}$ interaction point. The ray labeled e^- shows an example of the trajectory of an electron produced in an inelastic collision. The lines on the module show the layer and pad segmentation. 35

3.12 The Muon System 38

3.13 *top:* WAMUS drift cells. *bottom:* A single drift cell shown with equipotential lines. 39

3.14 A WAMUS vernier cathode pad. 40

4.1 The DØ Trigger System 50

4.2 The efficiency of the EM_1_HIGH trigger vs. photon E_T. 52
4.3 The efficiency of the GAM_HIGH_ISO filter vs. photon E_T. 53

5.1 The event distributions in the variables used in analysis cuts 1-9. . . . 67
5.2 The event distributions in the variables used in analysis cuts 10-13. . 68
5.3 The acceptance and offline analysis cut efficiencies, as determined from (mixture) Monte Carlo simulations. 69
5.4 The event distribution in $\cos\theta^*$ for experimental data *top left:* without offline analysis cuts, and *top right:* with offline analysis cuts. Monte Carlo Q^* events at $M^* = 200\ GeV/c^2$ *middle left:* without offline analysis cuts, and *middle right:* with offline analysis cuts. Monte Carlo Q^* events at $M^* = 400\ GeV/c^2$ *bottom left:* without offline analysis cuts, and *bottom right:* with offline analysis cuts. 71
5.5 *left:* Photon event efficiencies as a function of the upper limit cutoff on $\cos\theta^*$ for experimental data and for Q^* Monte Carlo samples. *right:* The ratio $R = \epsilon_{Q^*}/\epsilon_{Q^*+background}$ for Monte Carlo Q^* events at $M^* = 100$ and $400\ \mathrm{GeV}/c^2$. 72
5.6 Event distribution of experimental data sample in $\cos\theta^*$ *top left:* with no offline analysis cuts applied, *top right:* with analysis cuts 1 and 2 (see table 5.1), *bottom left:* with analysis cuts 2,3, and 4, and *bottom right:* with analysis cuts 1-13. 73
5.7 The photon purity γ vs. the photon E_T. 76

6.1 Inclusive prompt photon cross section. The vertical error bars are statistical and the horizontal error bars are systematic. Parton distribution functions are CTEQ2M and renormalization scale is $\mu = p_T$ of the photon. 78

6.2 (Data-Theory)/Theory for the cross section $\frac{d\sigma}{dp_T d\eta}$ shown in figure 6.1. Band at bottom shows systematic error in luminosity calculation. . . 79

6.3 The prompt photon inclusive cross section as a function of the photon-jet invariant mass. 80

6.4 (Data-Theory)/Theory for the prompt photon inclusive cross section $\frac{d\sigma}{dMd\eta}$ shown in figure 6.3. 81

6.5 Photon candidate events in η_γ vs η_{jet} for the three regions of uniform acceptance in η^* vs. η_{boost}. The lines at 45° are the η^* and η_{boost} axes. 83

6.6 The normalized $\cos\theta^*$ distribution. The curve is a spline fit to a NLL theory Monte Carlo calculation. 84

7.1 The photon-jet invariant mass distribution $M(GeV/c^2)$. 87

7.2 The error on the photon-jet mass ΔM associated with the energy and position resolution of the DØ detector. The curve is a polynomial fit to the data points, weighted by their errors. 89

7.3 The photon-jet mass resolution, $\sigma_M = \Delta M/M$, where ΔM is given by equation (7.3). 90

7.4 *top*: Monte Carlo direct photons with the requirement that the photon and jet $E_T > 5\ GeV$ compared with the same sample with the requirement that the photon $E_T > 35\ GeV$ and jet $E_T > 20\ GeV$. *bottom*: The photon-jet mass turn-on curve. This is the ratio of the two cross sections shown in the top part of the figure. 92

7.5 An example of χ^2 vs. $N(M^*)$ for a minimization fit of the function F(M) to the data. 96

7.6 Photon-jet invariant mass distributions for Monte Carlo simulated event samples of excited quark decays at several values of M^*. 98

7.7 The experimental mass distribution with a fit to the function $B(M) = \exp(A_1 + A_2 M)$. 100

7.8 The experimental mass distribution with a fit to the function $B(M) = \exp(A_1 + A_2 M) + \exp(A_3 + A_4 M)$. 102

7.9 *left:* The mass distribution of a sample of artificial background, produced by smearing the bin values of a histogram of the function B(M). *right:* The experimental photon-jet mass distribution. 104

7.10 An example of the results of a χ^2 fit performed to optimize the parameterization of $S(M|M^*)$. $M^* = 300$ GeV. 106

7.11 Values of A(M^*), W(M^*), and R(M^*) used in the parameterization of $S(M|M^*)$, displayed with their uncertainties at several values of M^*. The inner curves through the data points are polynomial fits to the discrete values of the parameters. The outer curves, above and below, are polynomial fits to the discrete values $\pm 1\sigma$ errors ΔA(M^*), ΔW(M^*), and ΔR(M^*). 108

8.1 *top:* The best value of the number of signal events $\hat{N}(M^*)$ from independent fits of $F(M|M^*)$ to the experimental mass distribution at 5 GeV intervals in M^*. The combined statistical and systematic error is displayed as a shaded band around the data points. *bottom:* The values of $\bar{\chi}^2$ vs. M^* for the same minimization fits. 112

8.2 The best values of the number of signal events $\hat{N}(M^*)$ and the error $\Delta N(M^*)$ from χ^2 minimization fits performed with a sum of two exponential functions $B(M) = e^{(A_1+A_2M)} + e^{(A_3+A_4M)}$ compared with the same from fits performed with a sum of two "product of powers" functions $B(M) = A_1 \frac{(1-M/s^{1/2})^{A_2}}{M^{A_3}} + A_4 \frac{(1-M/s^{1/2})^{A_5}}{M^{A_6}}$. 113

8.3 The distribution of the best values of the number of signal events $\hat{N}(M^*)$ for 20 samples of artificial background without any signal events adden, at each of several values of M^* ($M^* = 150, 200, 250, ..., 450$ GeV). 115

8.4 The sample mean and sample variance of the $\hat{N}(M^*)$ distributions of Fig. 8.3 vs. M^*. 116

8.5 The photon-jet experimental data sample *top:* significance $N/\Delta N$ vs. M^*, *middle:* $\tilde{\chi}^2$ vs. M^*, and *bottom:* χ^2 per bin $\times \frac{y_i - B(M_i)}{|y_i - B(M_i)|}$ vs. M^*. The symbols y_i and M_i denote the contents of bin i (either the number of events in the bin, or the weight of a merged bin) and the average mass integrated over the range of the bin ($M_i = \frac{\int dM\ M\ B(M)}{\int dM\ B(M)}$).119

9.1 The lower boundary of the shaded area is the upper limit on the $Q^* \to \gamma q$ cross section at the 95% confidence level . The curve intersecting it is the theoretical prediction of Baur *et al.*. The shaded region is all excluded at greater than 95% confidence. The parton distribution functions used in the theory calculation are CTEQ2L. 127

9.2 The upper limit at the 95% confidence level on the $Q^* \to \gamma q$ cross section shown with the theoretical prediction calculated with different parton distribution functions, as labeled. 128

9.3 The upper limit at the 95% confidence level on the $Q^* \to \gamma q$ cross section shown with the theoretical prediction at different values of the compositeness scale, $\Lambda = 250, 500, 750$ GeV. 129

A.1 $V(\phi) = \frac{1}{2}\mu^2\phi^2 + \frac{1}{4}\lambda\phi^4$ for (a) $\mu^2 > 0$ and (b) $\mu^2 < 0$ 135

ABSTRACT

This thesis presents a measurement of the inclusive cross-section for prompt photon production as a function of the invariant mass of the photon and highest energy jet in the final state. The experimental cross section is compared with a next-to-leading logarithm Quantum Chromodynamics (QCD) theoretical calculation. Also presented is a mass-fitting analysis in which the photon-jet invariant mass distribution is examined for evidence of excited quark production and decay, a signature of quark compositeness. No evidence of excited quark production was found. An upper limit on the excited quark cross section was established. This upper limit was compared with a theoretical prediction to set a lower limit on the mass of excited quarks of 531 GeV/c^2, according to the assumptions of the model.

CHAPTER 1
INTRODUCTION

"It seems probable to me that God in the Beginning form'd Matter in solid, massy, hard, impenetrable, moveable Particles."

Sir Isaac Newton, Opticks(1704)

This chapter states the motivation for this experiment on quark compositeness and gives a brief outline of the thesis.

1.1 A Brief History of Particle Physics

The references of this section are [4],[5].

A fundamental question that the science of particle physics attempts to answer is, "What is our universe made of?". An early theory of the nature of matter was proposed by Empedocles of Acragas. According to Empedocles, all things are mixtures in various proportions of four basic elements; earth, fire, air, and water. The elegance of this theory is that it reduces a complex system to a sum of simple parts. This quality is always desirable in a good scientific model. However, Empedocles' theory had very little predictive power.

A more practical theory was introduced by Leucippus and by Democritus with the concept of the atom. This theory (atomism) asserts that minute, discrete, finite, and indivisible elements are the ultimate constituents of all matter [6]. A major development in the understanding of atomic theory came with the formulation of the periodic table of elements, by Dmitri Mendeleev and others. The concept was introduced that matter is composed of chemical combinations of over 100 varieties of atoms. The atoms fall naturally into a systematic arrangement of families with similar chemical properties. The cycle of this family grouping repeats itself several times with elements of increasing atomic mass. The proliferation of atoms and their family grouping suggested that they were made up of more fundamental units. Subsequent critical thought and experimentation (by scientists including J.J. Rutherford, E. Thompson, and J. Chadwick) revealed that the atom is composed of a dense nucleus of protons and neutrons which are bound together by a strong nuclear force, surrounded by a cloud of electrons. The chemical properties of the atomic families are attributed primarily to the orbital arrangement of the electrons and the interactions between the electrons and the nucleus, which are described by the rules of quantum mechanics.

With the completion of the nuclear model of the atom, the proton, neutron, and electron were the only known particles. Cosmic ray experiments, and the advent of particle accelerators led to the discovery of many more particles, which interact strongly and decay into lighter particles. The proliferation of states once again challenged the simplicity of the model. Some of the particles are massive enough to decay, but have long lifetimes on the scale of the strong interaction. This was an indication of a conserved quantum number, which was called "strangeness". The SU(2) flavor symmetry group was expanded to accommodate the additional states in an SU(3) representation. Like Mendeleev's periodic table of the elements, the

grouping of states in an SU(3) multiplet hinted that there was a more fundamental level of structure which would explain the observed symmetry.

In 1964, the quark model of hadrons was proposed by Gell-Mann and by Zweig. According to this model, particles like the nucleons are composite, made of combinations of fundamental quarks. This static model, combined with the dynamics of "partons", introduced by Feynman in 1969[7],[8], led to the development of the Quark-parton Model (QPM), and eventually to the $SU(3)$ gauge theory of "Quantum Chromodynamics" (QCD) [9], which successfully describes a wide variety of high energy physics processes in many experimental settings [10]. QCD, together with the $SU(2) \times U(1)$ group of electroweak interactions and the Higgs mechanism makes up the Standard Model of particle physics. According to the Standard Model, quarks, leptons, and gauge bosons are all fundamental and point-like.

There is much reason to doubt that the Standard Model provides the most fundamental picture of particle interactions. There are three practically identical generations of quarks and leptons, differing primarily in mass. The total electromagnetic charge of each generation is given by:

$$3(q_u + q_d) + q_e + q_\nu = 3(\frac{2}{3} - \frac{1}{3}) - 1 + 0 = 0. \tag{1.1}$$

This cancellation of charge within each generation suggests a relation between the number of strong force colors to the proportions of electromagnetic charge in the quarks and leptons. The balance of positive to negative electromagnetic charge in an atom is exact to at least 1 part in 10^{21}. If charge were not so well balanced, macroscopic objects would have a net charge. Parameters which are included in, but not predicted by the Standard Model are the nine quark and lepton masses, four parameters of the Kobayashi-Maskawa quark-mixing matrix, three gauge couplings, the QCD θ parameter, and the Higgs potential parameters λ and v. At least nineteen parameters are not predicted by the model and are left to experimental measurement. The Standard Model includes six leptons and three colors of six

quarks, each of these mirrored by an antiparticle. There are eight gluons, $W^{\pm}$, Z°, and γ mediating the particle interactions, and at least one Higgs scalar to generate mass. This totals at least sixty-one dubiously fundamental particles.

It is desirable to find a model which explains these features in a simpler way. This model may include composite quarks and leptons which are combinations of a more fundamental particle. In past physics situations which led to the interpretation of the atom, the hadron, and the quark, a proliferation of states and a systematic organization of the states suggested a more fundamental level of structure.

1.2 Thesis Outline

The reader is assumed to have at least a passing familiarity with high energy collider experiments and particle physics. For introductory background, see [1],[2], and [3].

Chapter two discusses the quark model of hadrons, and the motivation for a search for quark compositeness. For the reader who is new to particle physics, begin by reading appendix A, which introduces Lagrangians, fields, gauges, symmetry groups, and the Standard Model.

Chapter three provides a description of the systems of the DØ detector, with discussion of their construction and the physics of their operation. Of particular importance to the analysis presented in this thesis is the DØ calorimeter, described in Section 3.2.

In a high energy physics experiment such as DØ, data collection must be reduced to a manageable rate. The experimentalist only wants to retain data which are of interest to a particular analysis. To accomplish both of these tasks, a "trigger" is devised which passes only data which meet a given set of criterion. This trigger is

essentially a set of conditions which determine if a collider event matches the profile of the signal event. Chapter four describes the process of collecting data with the use of a multi-level triggering system. The trigger which was used for collecting the data in this analysis is described. The methods of data processing and storage are discussed.

The data sample is unavoidably contaminated with "background" events which mimic the "signal" events of interest to the analysis. Chapter five discusses physical quantities which are used to characterize an event containing a photon, and the conditions (a.k.a. "cuts") which are applied to the experimental data sample to improve the signal to background ratio. The next section of chapter five describes the process of determining the purity of the sample. The last two sections discuss the photon-jet invariant mass, and the mass resolution of the detector.

Chapter six presents various measurements of the photon data sample and compares them with QCD theoretical predictions for prompt photon production.

Chapter seven describes the method of the photon-jet mass fitting analysis. I determine the expected mass distributions for excited quark decays and for background events. In a chi-squared minimization fit to the experimental mass distribution, I measure the number of excited quark candidate events and determine the significance of that number. Chapter eight presents the results of the fitting procedure and compares them with the theoretical model to establish confidence limits on the cross section and the mass of the excited quark. Chapter nine summarizes the results of the analysis.

CHAPTER 2

THEORETICAL BACKGROUND ON EXCITED QUARKS

This chapter describes the theoretical model of quark excited states which is investigated in this experimental analysis. The assumptions of the model are given, and predictions are here presented without proof. For a more inclusive discussion, see the sources, [11],[12],[13],[14].

2.1 Quark and Lepton Compositeness and Excited States

This section summarizes the model of fermion excited states presented in [11],[12],[13],[14].

Many compositeness models describe quarks and leptons as bound states of constituent particles called "preons", which interact via a new non-Abelian gauge field at a characteristic energy scale (Λ). A CDF result [15] constrains the compositeness scale for $qqqq$ contact interactions to be in the range $\Lambda > 1.4$ TeV for $g_c^2(\Lambda)/4\pi = 1$, where g_c is a new strong coupling between the preons. Direct preon interactions of this kind have not been observed at presently accessible collider energies.

A common prediction of many compositeness models is the existence of radial and/or orbital excited states of quarks and leptons. The dynamics of the preon system are unspecified, and excitations are not excluded at experimentally accessible energies, in the range of hundreds of GeV. The observation of massive excited state quarks decaying to the ground state would be conclusive evidence for compositeness. The signature of an excited quark decay will be indistinguishable from more common QCD processes, but the additional signal contribution will appear in the

invariant mass distribution of the final state products of events with this signature as a resonance peak centered at the excited quark mass.

The preon model which is tested in this analysis examines only quark excited states with spin and isospin 1/2, to limit the number of parameters. This does not exclude the possibility that the lowest lying excitation may be a spin-3/2 particle. In this model, quarks are a bound state of three spin-1/2 preons.

An excited state quark will be represented by the symbol Q^*, and the mass of this quark is M^*. The mass is dynamically generated, by the motion of the quark's constituents and not by the Higgs mechanism, so members of an excited weak isodoublet should be almost degenerate in mass.

As discussed in appendix A, the formulation of an experimentally verifiable theory requires an appropriate Lagrangian. The requirement of gauge invariance necessitates that the coupling between excited state spin-1/2 quarks and ordinary ground state quarks be of the magnetic moment type. The effective Lagrangian which describes the transition between excited and ground states is given by:

$$\mathcal{L}_{trans} = \frac{1}{\Lambda}\overline{Q^*}\sigma^{\mu\nu}[g_s f_s \frac{\lambda_a}{2} F^a_{\mu\nu} \ + \ g f \frac{\vec{\tau}}{2}\vec{W}_{\mu\nu} \ + \ g' f' \frac{Y}{2} B_{\mu\nu}]q_L \ + \ h.c. \qquad (2.1)$$

where Λ is the energy scale of the coupling; Q^* is the excited quark eigenstate; $\sigma^{\mu\nu} = (i/2)(\gamma^\mu\gamma^\nu - \gamma^\nu\gamma^\mu)$; q_L is the isospin doublet of a left handed ground state quark; $F^a_{\mu\nu}$,$W_{\mu\nu}$, and $B_{\mu\nu}$ are the field strength tensors for the gluon, $SU(2)$, and $U(1)$ gauge fields; g_s, $g = e/sin\theta_W$, and $g' = e/cos\theta_W$ are the gauge coupling constants; λ_a are the Gell-Mann matrices of color SU(3); $\vec{\tau}$ are the Pauli spin matrices; and Y is the weak hypercharge operator. The parameters f_s, f, and f' are determined by the preon system dynamics, and naively expected to be ≈ 1. In a higher order calculation, they become form factors, $f_s(Q^2)$, $f(Q^2)$, $f'(Q^2)$. The Lagrangian which describes transitions between excited and ground state leptons is of the same form.

From this Lagrangian are derived the decay rates and cross section. Assuming $M^* > m_{W,Z}$, one obtains

$$\Gamma(Q^* \to gQ) = \frac{4}{3}\alpha_s f_s^2 \frac{1}{4}(\frac{M^*}{\Lambda})^2 M^* \tag{2.2}$$

$$\Gamma(Q^* \to \gamma Q) = \alpha f_\gamma^2 \frac{1}{4}(\frac{M^*}{\Lambda})^2 M^* \tag{2.3}$$

$$\Gamma(Q^* \to {}^W_Z Q) = \frac{1}{8}\frac{g_{W,Z}^2}{4\pi} f_{W,Z}^2 (\frac{M^*}{\Lambda})^2 M^* (1 - \frac{m_{W,Z}^2}{M^{*2}})^2 (2 + \frac{m_{W,Z}^2}{M^{*2}}), \tag{2.4}$$

where

$$f_\gamma = fT_3 + f'\frac{1}{2}Y \tag{2.5}$$

$$f_W = \frac{f}{\sqrt{2}} \tag{2.6}$$

$$f_Z = fT_3 \cos^2\theta_W - f'\frac{Y}{2}\sin^2\theta_W. \tag{2.7}$$

$m_{W,Z}$ and $g_{W,Z}$ are the masses and coupling constants of the W and Z, $T_3 = +\frac{1}{2}, -\frac{1}{2}$ (u, d) is the third component of the weak isospin, and θ_W is the Weinberg angle. The branching ratios for u^* and d^* decay modes to ground state quarks plus gauge bosons are given in Table 2.1. As long as $M^* \gg m_{W,Z}$, the branching ratios should be insensitive to M^*. The total width for transition interactions is given by:

$$\Gamma(gq \to Q^*) \approx 0.04 f^2 M^* \tag{2.8}$$

Unless the f parameters (form factors) are much larger than one, the resonances will be very narrow, so the experimentally measured width of the mass distribution will be dominated by the detector resolution and, more significantly, by QCD radiation.

Single Q^* production decaying in the photon channel is shown in Fig. 2.1. The branching ratio to photons is small in comparison with other channels, but the signal is particularly clean, the mass resolution is the best in this channel, and

mode	branching ratio	mode	branching ratio
$u^* \to gu$	0.834	$d^* \to gd$	0.834
$u^* \to Wd$	0.109	$d^* \to Wd$	0.109
$u^* \to Zu$	0.035	$d^* \to Zd$	0.051
$u^* \to \gamma u$	0.022	$d^* \to \gamma d$	0.005

Table 2.1: The branching ratios for Q^* transition interactions, with spin-1/2, $f = f_s = f'$ $(= 1)$, $\alpha_s \approx 0.1$, and $M^* = 1$ TeV

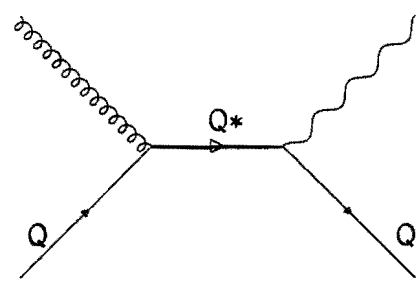

Figure 2.1: Feynman diagram of the process $gq \to Q^* \to \gamma q$.

the background is relatively manageable. Other DØ analyses on the other decay channels are in progress.

Excited quarks may couple to ordinary quarks by new strong interactions between the preons. These "contact" interactions are the largest contributors to the total Q^* production cross section. At energies below the compositeness scale, the effective four-fermion Lagrangian is given by:

$$\mathcal{L}_{contact} = \frac{g_c^2}{\Lambda^2}\frac{1}{2}j^\mu j_\mu, \tag{2.9}$$

with

$$j_\mu = \eta_L \bar{f}_L \gamma_\mu f_L \;+\; \eta'_L \bar{f}^*_L \gamma_\mu f^*_L \;+\; \eta''_L \bar{f}^*_L \gamma_\mu f_L \;+\; h.c. \;+\; (L \rightarrow R). \tag{2.10}$$

where j_μ are left handed fermionic currents between energy states and g_c is the new preon coupling. The width is given by:

$$\Gamma(f^* \rightarrow f + f'\bar{f}') = \frac{M^*}{96\pi}(\frac{M^*}{\Lambda})^4 N'_C S', \tag{2.11}$$

where N'_C is the number of colors of the light fermion and S' is a combinatorical factor, given by $S' = (1, \frac{4}{3}, 2)$ for ($f' \neq f$, $f' = f$ and both are quarks, $f' = f$ and both are leptons).

Excited quark production through contact interactions will have multiple jets in the final state. There will be several possible ways of combining these jets when reconstructing the mass in each event, only one of which gives the correct quark mass. In contact interactions, the width is strongly dependent on the ratio M^*/Λ (see (2.11)). The detection of Q^* production through contact interactions is further complicated because its relatively small cross section is contrasted with a large background from ordinary QCD multijet production. For simplicity, only leading order transition interactions were investigated in this analysis.

The cross section for excited quark production in $p\bar{p}$ collisions through quark-gluon fusion, and subsequent decay to a photon-jet final state, is given by:

$$\sigma_{p\bar{p}\to Q^*\to\gamma q} = \int dM \frac{2}{M} \int_{\ln\sqrt{\tau}}^{-\ln\sqrt{\tau}} dy\tau \; \mathcal{L}(x_1, x_2) \; \hat{\sigma}(M^2) \; P(\tau, y, y_c), \tag{2.12}$$

where M is the γq invariant mass, $\tau = x_1 x_2 = \frac{M^2}{s}$, s is the square of the $p\bar{p}$ center of mass energy, and $y = \frac{1}{2}\ln(\frac{x_1}{x_2})$. The parton-parton luminosity function is given by:

$$\mathcal{L}(x_1, x_2) = f_q(x_1, M^2) f_g(x_2, M^2) + f_q(x_2, M^2) f_g(x_1, M^2), \tag{2.13}$$

where $f_{q(g)}$ is a parton distribution function, which gives the momentum distribution of a quark(gluon) expressed as a fraction of the momentum of the beam particle (between 0 and 1). A discussion of luminosity and cross sections is presented in Section 4.1. The partonic cross section gives the probablility for the process as a function of M. It is in the form of a relativistic Breit-Wigner function:

$$\hat{\sigma} = \pi \frac{\hat{\Gamma}_{Q^*\to\gamma q} \; \hat{\Gamma}_{Q^*\to gq}}{(M^2 - M^{*2})^2 + (\hat{\Gamma}_{Q^*} M^*)^2}, \tag{2.14}$$

where

$$\hat{\Gamma}_{Q^*\to\gamma q} = \frac{f_\gamma^2(M^2)}{f_\gamma^2} \; (\frac{M}{M^*})^3 \; \Gamma_{Q^*\to\gamma q}, \tag{2.15}$$

$$\hat{\Gamma}_{Q^*} = \sum_{g,\gamma,W,Z} \Gamma_{Q^*\to Xq}. \tag{2.16}$$

The function $P(\tau, y, y_c)$ expresses the probability that both final state particles have rapidities within the limit $|y| < y_c$.

CHAPTER 3
THE DØ DETECTOR

The DØ Detector is a general purpose detector operating at the Fermilab Tevatron $p\bar{p}$ collider. It was designed for the purpose of measuring high energy particle phenomena, with an emphasis on lepton identification, good calorimeter energy resolution and granularity, and full detector coverage, including regions of high rapidity. Most of the information in this chapter is excerpted from the resources [16],[17],[18].

The physics topics which are being studied at DØ include the search for the top quark; precision measurements of QCD phenomena at high P_T; studies of the electroweak sector, including the mass ratio of W to Z; b quark studies; and searches for physics beyond the Standard Model, including Supersymmetry. Each of these physics processes has a characteristic signature which distinguishes it from other processes. For example, a direct photon event is characterized by an isolated electromagnetic energy deposit with no charged particle tracks pointing to it, and by one or more jets of particles in the opposite hemisphere of the detector.

There are three major systems in the DØ detector, which together are used to reconstruct the signatures of the wide variety of high energy physics processes under study. The central tracking system serves to localize the interaction vertex, to identify charged particles, and to track their direction as they pass through the detector. The calorimeter measures the energy and direction of electrons and jets produced in an event. The muon system tracks and measures the momentum of muons.

The DØ detector is calibrated with a combination of data from Monte Carlo simulations, from test beam analysis, and from collider events. In a Monte Carlo

study, high energy particle interactions are simulated on computer by random number generation controlled by complex algorithms which constrain probabilities. The interaction of the high energy particles with detector systems is also modeled by computer simulation.

Two series of test beam experiments were carried out, in which a few modules from the calorimeter were exposed to particle beams of electrons and pions. We measure the response of the modules to energy deposited by particles of known momentum, and use these data in the calibration of the calorimeter. We use collider events with particles whose mass has previously been measured, such as Z° decays, to calibrate the energy scale of the calorimeter.

To facilitate the description of DØ detector systems, a word must be said about the coordinate systems used to map the detector geometry. Two coordinate systems are used: right-handed cartesian coordinates (x,y,z) and cylindrical coordinates (θ,ϕ,z). The z coordinate is parallel to the beam axis with the origin at the center of the detector; the positive direction being that of the proton beam. The x and y coordinates are orthogonal to each other and to the z coordinate, with the y axis vertical with respect to the floor. The azimuthal angle ϕ ranges from 0 to 2π ($\phi = 0$ on x-axis and $\phi = \pi/2$ on y-axis). The polar angle θ is the angle with respect to the z axis. Another coordinate commonly used is pseudorapidity (η), which is a good approximation of rapidity (y) for highly relativistic particles. The transformation between θ and η is given by the relation

$$\eta = -\ln(\tan(\theta/2)). \tag{3.1}$$

An advantage to expressing the polar angle in rapidity is that a transformation between two Lorentz frames related by longitudinal boosts is simple, given by:

$$y' = y + \tanh^{-1}(\beta), \tag{3.2}$$

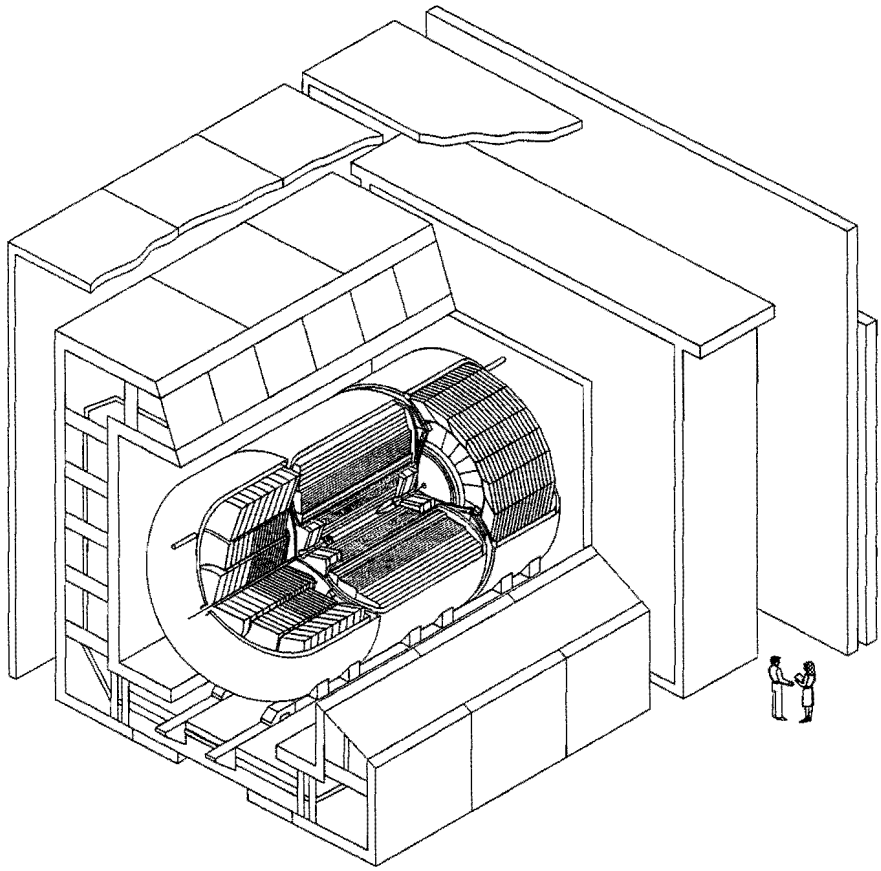

DØ Detector

Figure 3.1: The DØ Detector

where $\beta = v/c$ with v being the relative velocity between the two frames. The shape of the rapidity distribution dN/dy is Lorentz invariant, meaning that it is unchanged by a transformation to another Lorentz frame. Such a transformation is called a "Lorentz boost".

3.1 The Central Tracking System

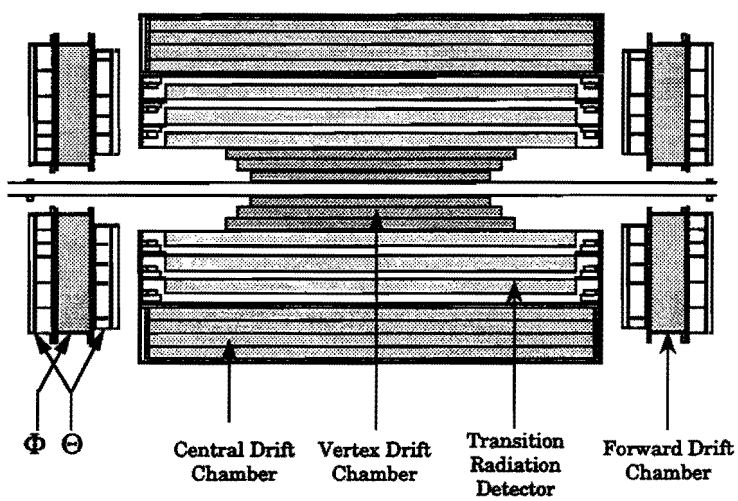

Figure 3.2: The Central Tracking System

Central tracking is composed of four independent detector systems; the Vertex Chamber, the Transition Radiation Detector, and the Central and Forward Drift Chambers. Together, they provide information for charged particle indentification and path reconstruction.

3.1.1 The Vertex Drift Chamber (VTX)

The innermost part of the central tracking system is the Vertex Drift Chamber. Its function is to measure charged particle tracks close to the interaction region in

order to reconstruct the point of origin, and also to detect the presence of secondary vertices from the decays of heavy quarks. This task must be done with great precision, as there may be closely spaced vertices from multiple interactions in the same beam crossing.

The Vertex Chamber is a cylindrical structure, consisting of three concentric layers. Each layer is segmented into cells; 16 segments in the innermost layer and 32 segments in both the second and third layers. The walls of the chamber are concentric cylinders made of a carbon fiber composite, low in density to minimize photon conversions. The walls are connected at either end to G-10 bulkheads, joined by titanium tie rods which support wire tensions. The Vertex Chamber has an inner radius of 3.7 cm and an outer active radius of 16.2 cm [19],[20].

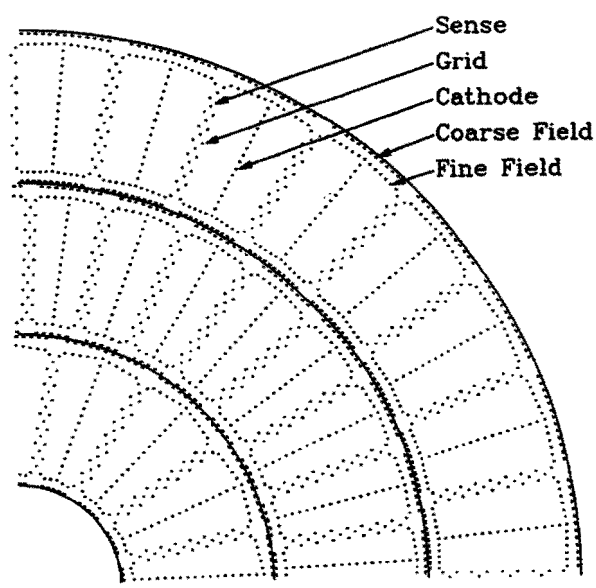

Figure 3.3: The Vertex Chamber

The cells of the vertex chamber are filled with a gas mixture of CO_2(95%)-ethane (5%) at one atmosphere of pressure. Each cell contains eight sense wires, which are used to measure the r and ϕ coordinates of charged particles passing through the cell. The passing of a charged particle ionizes gas in the chamber, and the resulting

free electrons drift in an electric field towards the anode sense wires. Field shaping is achieved by varying potentials at the sense wires, cathode wires, fine field wires, grid wires, and aluminum traces on the surface of the cylinder walls. As the electrons approach the anode wires, they are accelerated by the electric field, rising as $1/r$. At very short distances from the wires, the energy of the electrons exceeds the ionization energy of the gas, so more electrons are liberated, creating an avalanche of charged particles around the sense wires. The number of secondary electrons reaching the anodes is directly proportional to the number of initial ionizations, thus the chamber is an example of what is called a Proportional Wire Chamber (PWC). An electric pulse is induced on the wires, due to the drift of positive ions away from the anode wires. The pulse (a "hit", in jargon) is amplified and digitized. The timing, amplitude, and width of the pulses on the wires are used to reconstruct the path of the original charged particle [26].

3.1.2 The Transition Radiation Detector (TRD)

The next layer of central tracking, which surrounds the Vertex detector, is the Transition Radiation Detector. Its purpose is to help distinguish electrons from charged pions and other particles.

When a highly relativistic charged particle passes between two media which have different dielectric constants, the field surrounding the particle must adjust to satisfy the boundary conditions. Soft x-rays are produced at the boundary, called Transition Radiation. For a single boundary, the energy radiated is a function of $\beta\gamma$ ($\beta = v/c$, $\gamma = \frac{1}{\sqrt{1-\beta^2}}$). The angular distribution of the radiated energy is sharply peaked at an angle $\propto 1/\gamma$ with respect to the particle trajectory [27]. Since pions and other charged hadrons are much more massive than electrons, they will radiate less energy than an electron of the same energy. The contributing effects are somewhat more complex, in that there are interference effects between transition layers, and there are additional sources of energy loss due to ionization caused by the charged

particle itself, and atomic collisions involving large energy transfer which liberate delta rays[28]. As $\gamma \rightarrow \infty$, the total energy emitted due to an assembly of foils of finite width reaches a limiting value, which depends on the number of foils and other properties of the detector. In the DØ detector, the TRD X-ray energy distribution for electrons above a few GeV is mostly below 30 keV, peaking at about 8 keV.

The TRD is constructed in three concentric layers, each layer segmented into 16 cells. Each cell contains a radiator and a wire chamber to detect the X-rays. The radiator section is composed of a stack of 393 foils of 18μm thick polypropylene in a chamber filled with nitrogen gas. A pattern is embossed on the foils to maintain a thin gap between them which the gas will fill. There are thus many transition regions that a charged particle traverses as it passes through the radiator. Behind the radiator is the detector volume; a PWC filled with a mixture of $Xe(91\%)/CH_4(7\%)/C_2H_6(2\%)$ gas.

X-rays produced in the radiator convert by photoelectric absorption, and the electrons from the resulting ion pairs induce an ionization avalanche in the PWC amplification section. A noble gas can only be excited by photon absorption, so the xenon mixture is essentially stable. The cross section for recapture of free electrons from ionization is small, as they drift towards the anodes. The charge cloud of drifting electrons and ions induces a current pulse in the sense wires of the PWC, which is amplified and digitized. Both the amplitude and time distribution of the pulse are used to distinguish between electrons and pions. After suitable calorimeter conditions have already been applied to select electrons, the TRD is estimated to provide an additional pion rejection factor of about 10 in a low luminosity environment.

The outer walls of the TRD are a 1.1 cm thick Nomex honeycomb with fiberglass skins. The radiator sections are encased in carbon fiber tubes. Two thin mylar windows separate the radiator volume of a TRD cell from the detector volume. CO_2 gas flows in a gap between them to minimize diffusion of nitrogen gas from

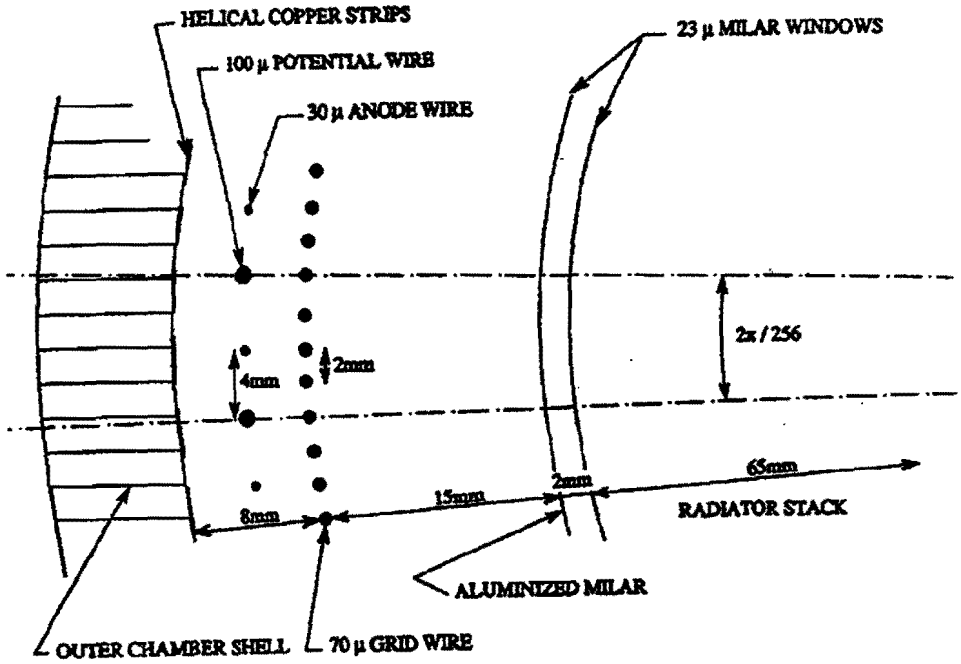

Figure 3.4: The Transition Radiation Detector

the radiator volume to the detector volume, where it would contaminate the xenon mixure. The outer window is aluminized and acts as a cathode for the drift field. Behind the window is the detector volume. There is a 15mm conversion stage and an 8mm amplification stage, separated by a cathode grid of wires. In the amplification stage are anode wires for charge collection, and field shaping wires. At the back of the amplification volume is another cathode layer of helical copper strips deposited on Kapton foil. The anode wires are grouped in pairs of two, for a total of 256 readout channels in each of the three layers of the TRD, with the same number of readout channels from the cathode strips. The sum of the combined layers of the TRD averages 0.81 radiation lengths (0.036 interaction lengths) in thickness.

For further information on the Transition Radiation Detector, see [21],[22],[23], and the PhD theses of F. Feinstein [24] and A. Pluquet [25].

3.1.3 The Central and Forward Drift Chambers (CDC and FDC)

The Central and Forward Drift Chambers are used to reconstruct the trajectories of charged particles. The Central Drift Chamber surrounds the TRD as a concentric cylinder, while the Forward Drift Chambers cap the CDC at either end, extending the tracking coverage to regions of high pseudorapidity. Like the Vertex Chamber, they use the drift time information of electrons from gas ionization to reconstruct tracks.

The Central Drift Chamber is constructed of 32 identical modules. The modules are each divided into four radial layers, which are separated by Rohacell "shelves", connected at either end to G-10 bulkheads. The entire apparatus is enclosed in an aluminum cylinder with two aluminum plates at either end, which support all wires under tension.

Each radial layer is divided into 32 azimuthal cells, which are staggered between layers by one half cell width to reduce dead space on any one radial trajectory. The cells are filled with a gas mixture of $Ar(92.5\%)CH_4(4\%)CO_2(3\%)H_2O(0.5\%)$. The

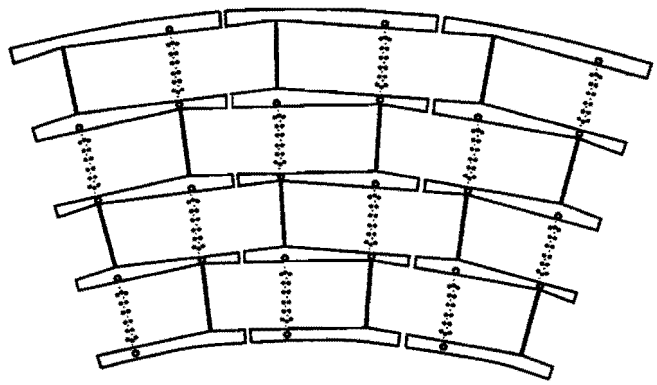

Figure 3.5: The Central Drift Chamber Modules

cells each contain seven sense wires (anodes) and two delay lines, running parallel to the beam axis and arranged in a plane from the inner to the outer wall. The sense wires are staggered by $\pm 200\mu$m in ϕ to resolve left-right ambiguity to either side of the wire plane. Resisitive epoxy strips are screen printed on the cell walls parallel to the anode planes. These strips are connected through a series of voltage dividers, and are used to shape the electric field around the anode wires. There are also two potential wires between each pair of anode wires for field shaping.

In each cell are two delay lines enclosed in Teflon tubes, embedded in the shelves and closely adjacent to the innermost and outermost sense wires. A signal in the sense wires will induce a pulse in the delay lines. Timing differences in the arrival of a signal at either end of the delay line provide the information which localizes the position of a track in the z-coordinate.

The position resolution of the CDC is 180μm in r and 3.5mm in z. With a drift field of 620 V/cm, the drift velocity is $\approx 34\mu m/ns$. The maximum drift distance is $\approx 7\ cm$. A scintillating fiber detector is included to aid in calibration of the CDC. This detector subtends the arc of only one CDC cell, and sits between the outer shell of the CDC and the inner skin of the first layer of the calorimeter. The geometric

coverage of the Central Drift Chamber is complete in the ϕ coordinate, and extends to about ± 1.0 in pseudorapidity.

The Forward Drift Chambers continue tracking coverage over the pseudorapidity range of about $1 < |\eta| < 3.2$. Each FDC unit consists of three chambers, configured in layers behind each other.

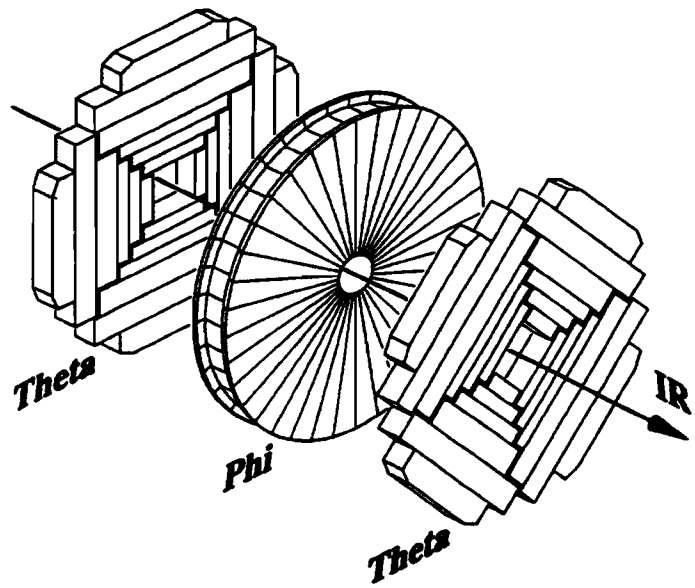

Figure 3.6: The Forward Drift Chambers

The inner and outermost chambers have sense wires perpendicular to the radial direction, which measure the θ coordinate of charged particles. These chambers are rotated by 45° with respect to each other. The θ chambers are divided into four mechanically separate quadrants. Each quadrant contains six rectangular cells at increasing radii. The cells each contain eight sense wires aligned perpendicular to the z coordinate. Between the sense wires are pairs of ground wires to shape the electric field. As in the CDC, each cell also contains a single delay line to measure the position of a charged particle track in the dimension parallel to the sense wires. The front and back walls are Kevlar coated Nomex honeycomb.

The middle chamber of each FDC unit has 16 layers of sense wires, 50 cm in length in the radial direction, and is used to measure charged particle tracks in the ϕ coordinate. This ϕ chamber is segmented into 36 mechanically separated pie-shaped wedges, each with 16 anode wires. Between each pair of sense wires in the ϕ chamber is a single ground wire. Aluminum strips on the inner surface of the wedge shaped cells are held at ground potential, to act as cathodes and to shape the field. The sense wires in both the θ and ϕ chambers are staggered by 0.2mm to resolve left-right ambiguity. Both θ and ϕ chambers have a maximum drift distance of 5.3 cm. The FDC chambers use the same gas mixture as the CDC chambers.

For more information on the Central and Forward Drift Chambers, see the PhD theses of T. Behnke[29], S. Rajagopalan [30], D. Pizzuto [31], and J. Bantly [32].

3.2 The Calorimetry

The DØ calorimetry is the centerpiece of the DØ detector design. It consists of uranium-liquid argon sampling calorimeters with emphasis on good energy resolution and fine segmentation for precise measurement of energy flow from electrons and jets. The calorimetry is divided into a central, barrel shaped calorimeter and two end cap calorimeters. Each of these sections is contained in an independent cryostat. The calorimeters are segmented, as a structure of adjacent interlinked modules.

The DØ calorimeters measure the energy deposited by particles produced in $p\bar{p}$ collisions, so before continuing, a brief overview of the mechanisms of energy loss for highly relativistic particles passing through matter is appropriate. In the case of high energy electrons and photons, the principal processes of energy loss are bremsstrahlung and electron pair production. The transverse electric field of

a charged particle is proportional to its Lorentz boost, γ. As the particle passes through a medium, it experiences an electromagnetic force acting on it from interactions with the electric fields of individual atoms. The particle's "impact parameter" is the perpendicular distance between its incident trajectory and the center of that force. When the impact parameter is comparable to interatomic distances, the nuclear electric field causes deceleration, and subsequent energy loss through the radiation of high energy photons. This process is called "bremsstrahlung", which translates as "braking radiation". A high energy photon in the nuclear electric field will convert into an electron-positron pair; a process called "pair-production". As a high energy electron passes through a medium, it will emit bremsstrahlung, producing energetic photons which will then pair-produce. The combination of the two processes creates a cascade of photons and electrons, called an electromagnetic shower. The average rate of radiative energy loss is approximately proportional to the incident energy of the particle. The number of shower particles will continue to multiply until the energy of secondary electrons falls to a critical energy, $E_C \approx 800MeV/(Z+1.2)$ for solids and liquids, below which the dominant process for energy loss is ionization. Additional shower particles are not produced, and the electromagnetic shower dies out.

The length scale used to parameterize the longitudinal development of a high energy EM shower is the radiation length (X_0). It is the mean distance traveled by an electron through a medium during which it will lose, by bremsstrahlung, a fraction $1-1/e$ of its original energy. The radiation length is approximately given by:

$$X_0 = \frac{716.4\ g\ cm^{-2}A}{Z(Z+1)\ln(287/\sqrt{Z})} \tag{3.3}$$

where A and Z are the mass number and atomic number of the medium. Electromagnetic shower development perpendicular to the direction of the incident particle scales with the Molière radius, $R_m = X_0 E_S/E_C$ ($E_S \approx 21MeV$).

In the case of hadrons, the incident particle undergoes inelastic nuclear collisions in a medium, producing secondary energetic hadrons. The secondary particles take part in inelastic collisions producing still more hadrons. This successive particle multiplication is a hadronic shower, which eventually dies when the energy of secondary particles is insufficient for further particle production, and the remaining energy is lost through ionization. The characteristic length scale for hadronic showers is the nuclear interaction length, $\Lambda \approx 35\ g\ cm^{-2} A^{1/3}$. Longitudinal energy deposit is sharply peaked at one interaction length, with a maximum at $x/\Lambda \approx 0.2 \ln(E/1\ GeV) + 0.7$ [33].

A sampling calorimeter is so named because it doesn't measure all of the energy deposited in it, but only samples the energy. All of the energy from a jet must be contained within the detector, but because of size limitations, the entire volume of the calorimeter cannot be made energy sensitive. Therefore, part of the detector volume is "dead", and functions to absorb most of the deposited energy. Mixed within this absorber material are active regions which measure a fraction of the total deposited energy. The active materials may be scintillating plastic tiles or fibers, lead glass, sodium iodide, or in the case of DØ, liquid argon. Thus, a sampling calorimeter consists of some mixture of absorbing and active material.

The absorber materials in the DØ calorimeter are plates of uranium, copper, and steel, chosen for their high density and relatively short interaction length, which minimizes the detector size needed to fully contain particle energy. Additionally, uranium provides more equal energy response to electromagnetic and hadronic showers than other materials. A large percentage of hadronic energy loss is through the breakup of nuclei and nuclear excitations, which is not measurable as ionization energy. By using uranium as an absorber material, the visible energy from electromagnetic processes is supressed. The calorimeter's active regions are gaps between the plates filled with liquid argon. Liquid argon has the advantage of good radi-

ation hardness, while its major disadvantages are its slow ion drift speed and the necessity for cryogenics. Thin signal boards are centered in the gaps, which measure ionization energy in the liquid argon. The boards are constructed of two sheets of G-10, a composite of plastic and glass fibers. The sheets are coated on one side with a carbon-based resistive material. One of the boards is clad with a thin layer of copper on the opposite side, which is etched into a grid of copper pads. The copper pads are shaped and positioned to occupy a small unit of solid angle equal to about 0.1×0.1 in $\eta \times \phi$ space in most layers. Copper traces from individual pads lead to the edges of the boards. The G-10 sheets are epoxied together, forming a sandwich with copper pads in the middle and resistive coating on either side. Pads in several successive active layers are ganged together with wires to form a cell. Each layer of cells is called a readout layer. With increasing calorimeter depth, the readout layers become thicker, and the ratio of active to absorber material, i.e. the energy sampling fraction, decreases.

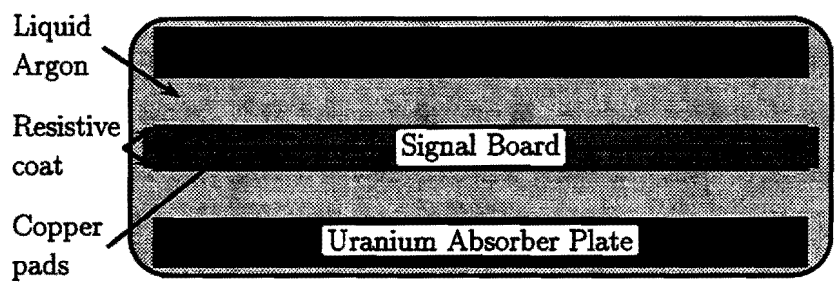

Figure 3.7: A Single Calorimeter Gap Interval (cutaway view)

The resistive coat on the signal boards is kept at an electric potential of +(2.0 to 2.5) kV, and the absorber plates are maintained at ground potential. As charged particles pass through the active gaps between absorber plates, they ionize the liquid argon, liberating electrons. The free electrons drift in the electric field, and are collected at the resistive coat on the boards. The changing field from charge

drift induces a current in the copper pads. Cables from the cells of ganged pads conduct the current to preamplifiers, which boost the current pulse and carry it outside the calorimeter through signal wires. The current pulse, induced by showers of charged particles, is amplified, shaped, and digitized. The information is used to derive the deposited energy. A collection of energy measurements from all cells in the calorimeter is used to reconstruct the energy flow of particles from an event.

As the electric field in the active layer gaps is increased, so does the drift velocity of free ionization electrons. The distance beween an absorber plate and its adjacent signal board is 2.3mm, and the typical electron drift time across a gap is $\approx$ 450ns. It is desirable to maximize the drift velocity so that all of the charge will be collected and dissipated before the next event introduces new particles into the gap. The effect of overlapping events in the calorimeter is called pileup, and it degrades the energy resolution. The time in which the calorimeter collects and dissipates charge is the relaxation time. At a critical gap field value, the electron drift velocity saturates, i.e. does not continue to rise. Further increase in the field will not significantly decrease the relaxation time. If the field is too high, dielectric breakdown occurs in the gap, causing sparking between the boards and plates. The operating gap field is thus balanced to minimize relaxation time and at the same time to maintain field stability.

Extensive testing was performed on the calorimeter modules, and strict standards of cleanliness were enforced to ensure that foreign material was not introduced into the gaps. The slightest contamination or defect can cause a short circuit between the signal boards and ground potential, rendering an entire layer inactive. Once the modules were installed within their cryostats, they became permanently inaccessible. The calorimeters must perform reliably under extreme temperature conditions for the working life of the detector.

Calorimeter modules were subjected to pulse vacuum cleaning, with a special high volume vacuum system which affixed to the module side skins. Each board in a module was probed with a voltmeter at various points along the surface to search for current leakage. The modules were rotated along their length, to disturb loose contaminants. After rigorous inspection, the modules were craned into the cryostat shell and joined to each other at their bulkheads with stainless steel pins and mounting brackets.

3.2.1 The Central Calorimeter and End Calorimeters (CC and EC)

The central calorimeter is composed of three layered rings of modules enclosed in a cryostat. A typical central calorimeter (CC) module is a long trapezoidal box shape, consisting of a stack of absorber plates and signal boards enclosed in a perforated stainless steel skin. The weight of the stack is carried by thick stainless steel bulkheads at either end of the module. Small Delrin (plastic) spacers between plates and boards maintain uniform spacing in the gaps. Each module is fitted with thermistors at either end to monitor temperature uniformity in the liquid argon bath.

The innermost ring of 32 CC modules surrounds the central tracking detectors. Electromagnetic particle showers originating from photons and electrons will be mostly contained in this first layer; the electromagnetic (EM) section. The absorber plates are thinnest (3mm) here, providing frequent energy sampling. The third layer of cells in the CCEM is where the peak energy deposit of most electromagnetic showers occurs, so cell segmentation is here further subdivided into 0.5×0.5 units in $\eta \times \phi$ for better position resolution. The CCEM covers full azimuth over the range $|\eta| < 1.1$.

The next concentric ring of 16 modules in the central calorimeter is the fine hadronic (FH) section, covering the region $|\eta| < 1.1$. Electromagnetic showers have almost completely died out at this depth, so it is mostly hadronic particles such as

pions which penetrate beyond the EM section. The fractional energy resolution for hadronic showers is approximately $50\%/\sqrt{E}$, determined from analysis of test beam data. Beyond the CCFH section is a third ring of 16 modules; the coarse hadronic (CH) section, covering the region $|\eta| < 0.6$. These modules catch any additional hadronic energy that was not absorbed in the FH section. Energy sampling is less frequent here, and energy resolution need not be as precise as in the CCFH.

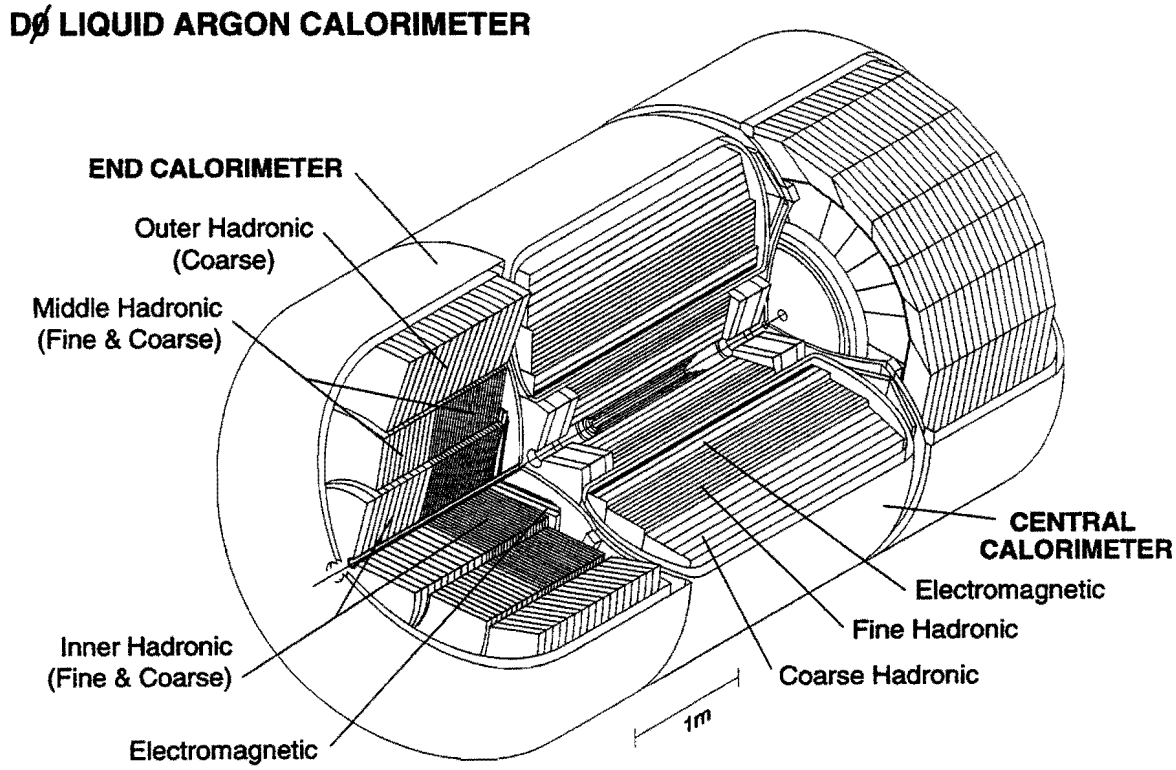

Figure 3.8: The Calorimeters

The energy resolution of the calorimeter can be expressed as:

$$\frac{\sigma}{E} = \sqrt{C^2 + \frac{S^2}{E} + \frac{N^2}{E^2}} \tag{3.4}$$

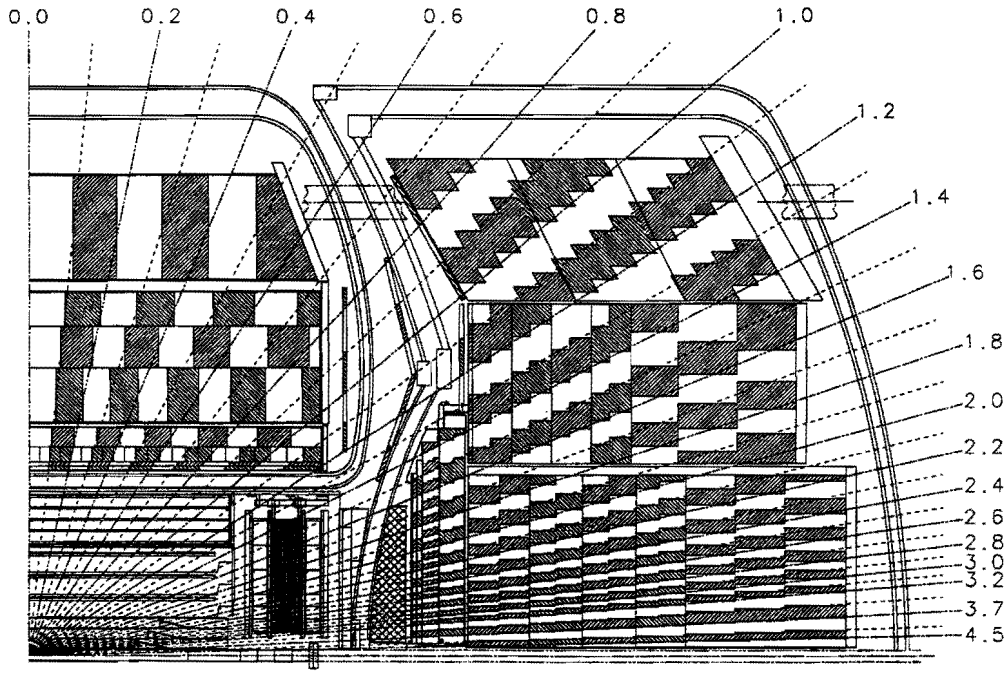

Figure 3.9: A side view of the calorimeter, showing transverse and longitudinal segmentation. The numbered rays show pseudorapidity intervals.

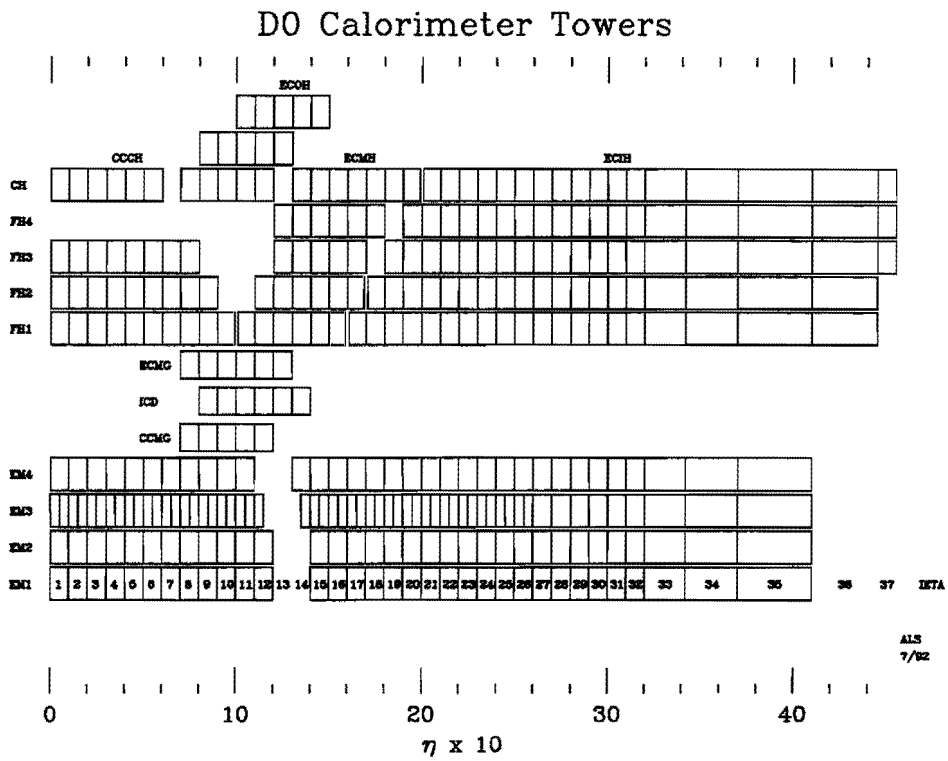

Figure 3.10: A foldout view of the calorimeter cell structure in $(\eta \times 10)$ vs. R coordinates. The calorimeter layers are labeled on the vertical axis.

where E is the incident particle energy, C parameterizes energy dependent factors like calibration errors, S comes from sampling fluctuations, and N comes from energy independent factors like electronic noise and uranium noise. These parameters are correlated. The contribution to the total resolution error from noise is measured as a function of time by taking periodic pedestal runs, with no beam in the detector. The width of the energy distribution for these runs is the value of N ($\approx$ 1 GeV). For accurate comparison to Monte Carlo data, the noise contribution is subtracted in quadrature from the fractional energy resolution. Fit values of the remaining parameters for electrons in the CCEM are $C = 0.005$, and $S = 0.13\sqrt{GeV}$. The sampling term was determined in test beam measurements [34],[35],[36],[37] and the constant term from Z$\rightarrow$ee decays [38]. Calorimeter position resolution for isolated EM showers is 0.8 to 1.2 mm in the central region, and scales as $\sqrt{E}$, [39].

The two end calorimeters, north and south (ECN and ECS), cover the rapidity range $1.1 < |\eta| < 4.5$ There are four types of modules in the EC. As in the CC, cell segmentation is 0.1×0.1 in $\eta \times \phi$ space, up to a pseudorapidity of 3.2. As pseudorapidity increases, the cell sizes become smaller; so the cell subdivisions in $\eta \times \phi$ become increasingly larger at the highest pseudorapidities, to a maximum size of 0.4×0.4. In each EC, a single disk shaped EM module covers pseudorapidity in the region $1.2 < |\eta| < 3.7$. ECEM modules have four readout layers, as in the CCEM. The 3mm uranium absorber plates and signal boards are stacked on either side of a stainless steel plate, with a stainless steel cylinder down the center. Tie rods and spacers maintain spacing and transfer the weight of the assembly to the central support plate. The EC inner hadronic (ECIH) modules sit behind the ECEM layers, covering the region $1.6 < |\eta| < 4.5$. The ECIH modules have a fine hadronic section (ECIFH) containing 64 uranium plates (6mm) in four readout layers, and a coarse hadronic section (ECICH) containing 13 stainless steel plates (46.5mm) in one readout layer. The EC middle hadronic (ECMH) section forms a

	CCEM	CCFH	CCCH
Modules	32	16	16
Inner Radius	84.1″	105.8″	170.9″
Outer Radius	104.5″	166.2″	219.3″
Front Plate Thickness	0.13″	0.48″	0.48″
Sideskin Thickness	0.17″	0.27″	0.27″
Endplate Thickness	1.9″	3.2″	4.4″
Readout Layers	4	3	1
$\Delta\eta \times \Delta\phi$	0.1×0.1	0.1×0.1	0.1×0.1
η coverage	± 1.2	± 1.0	± 0.6
Absorber	Uranium	Uranium	Copper
Plate thickness	0.118″	0.236″	1.625″
Gap thickness	0.09″	0.09″	0.09″
Sampling Fraction	0.119	0.068	0.015
Thickness in X_0	20.5	96.0	32.9
Thickness in Λ	0.76	3.2	3.2

Table 3.1: The Central Calorimeter design parameters.

	ECEM	ECIFH	ECICH	ECMFH	ECMCH	ECOH
Modules	1	1	1	16	16	16
Readout Layers	4	4	1	4	1	3
$\Delta\eta \times \Delta\phi$	0.1×0.1	0.1×0.1	0.1×0.1	0.1×0.1	0.1×0.1	0.1×0.1
η coverage	$1.4 - 4.0$	$1.6 - 4.45$	$2.0 - 4.45$	$1.0 - 1.7$	$1.3 - 1.9$	$0.7 - 1.4$
Absorber	Uranium	Uranium	Steel	Uranium	Steel	Steel
Plate thickness	$0.118''$	$0.236''$	$0.236''$	$0.236''$	$1.83''$	$1.83''$
Gap thickness	$0.09''$	$0.082''$	$0.082''$	$0.087''$	$0.087''$	$0.087''$
Sampling Fraction	0.119	0.057	0.015	0.067	0.016	0.016
Thickness in X_0	20.5	121.8	32.8	115.5	37.9	65.1
Thickness in Λ	0.949	4.91	3.57	4.05	4.08	7.01

Table 3.2: The End Calorimeter design parameters

ring surrounding the inner hadronic plug. It consists of 16 fine hadronic (ECMFH) modules and 16 coarse hadronic (ECMCH) modules in each end calorimer.

The central and end calorimeters are shown in different views in Figures 3.8, 3.9, 3.10, and 3.11. The first figure is a three-dimensional cutaway view, showing the CC and EC modular divisions. The second shows a cross-section of one half of the CC and EC sections, with the pseudoprojective towers of cells displayed in alternating dark and light shades. The numbers in the scale on this figure are units of pseudorapidity. The third figure is a two dimensional layout-type map of the calorimeter towers in $\eta \times 10$ vs. layer. The fourth figure shows the end calorimeter, in relation to the interaction region.

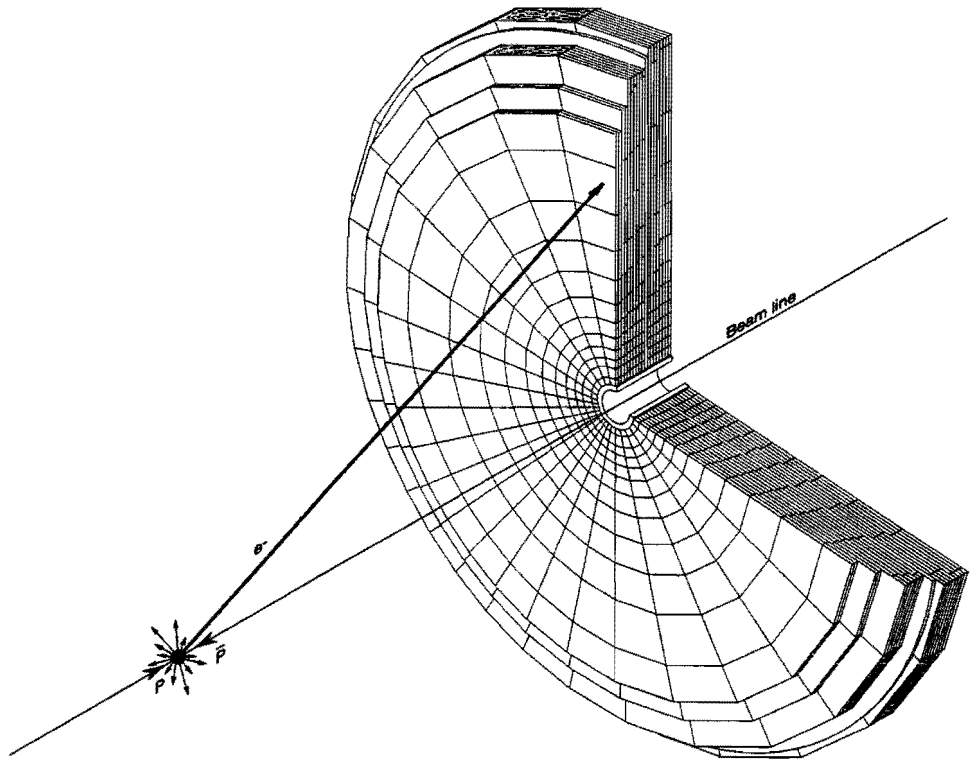

DØ END CALORIMETER ELECTROMAGNETIC MODULE

Figure 3.11: An ECEM module shown in relation to the $p\bar{p}$ interaction point. The ray labeled e^- shows an example of the trajectory of an electron produced in an inelastic collision. The lines on the module show the layer and pad segmentation.

3.2.2 The Intercryostat Detectors (ICD) and Massless Gap Detectors (MG)

Structural constraints necessitated a separation between the CC and EC in separate cryostats, such that there is a region between them with decreased calorimeter coverage. The ICD and MG Detectors are used to sample particle energy which flows in the transition space between the CC and EC, next to the cryostat walls.

Each ICD consists of a pair of scintillation counter modules mounted on the outer face of an End Calorimeter cryostat. An ICD contains 384 tiles made from Bicron BC-414 scintillator. Each tile covers a 0.1×0.1 region of $\eta \times \phi$ space and is aligned to match a pseudoprojective calorimeter tower. Light generated in the tiles by penetrating particles is carried out through bundles of wavelength shifting fibers to phototubes located directly behind the tiles. The scintillator array is calibrated with light from a UV laser, which is transmitted to each individual tile through an optical fiber [41].

The Massless Gap Detectors consist of single calorimeter readout boards mounted on the endplates of the CCFH modules (320 channels) and on the front plates of the ECMH and ECOH modules (192 channels). Liquid argon in the gaps serves as the active material, just as within the calorimeter modules, and the CC module bulkheads and cryostat walls are the absorber material [43].

3.3 The Muon System

The energy from high energy muons cannot be contained within the DØ calorimetery. Because muons are much heavier than electrons, radiative processes are not a dominant source of energy loss below particle energies of several hundred GeV. Muons do not interact strongly, so they do not initiate a hadronic shower except in

the case of a photonuclear interaction, which accounts for only a small percentage of total energy loss and has a relatively small cross section [33]. Although the energy of a muon is not completely absorbed in the calorimeter, it is possible to measure the muon's momentum, by bending its trajectory in a magnetic field $\vec{B}$. The relationship between the field $\vec{B}$, the particle momentum $\vec{p}$, the particle charge q, and radius of curvature $\vec{r}$ of its bent trajectory is given by $\vec{p} = \frac{q}{c}\vec{r} \times \vec{B}$.

The magnetic field in the DØ muon system is provided by five iron toroid magnets. The central toroid (CF) covers the pseodorapidity range $|\eta| < 1$, and two end toroids (EF) cover $1 < |\eta| < 2.5$. The Small Angle Muon Spectrometer (SAMUS) toroids extend coverage over $2.5 < |\eta| < 3.6$. The mean internal magnetic field in the toroids is 1.9T. A muon's trajectory as it traverses the magnets is measured by three layers of proportional drift tube chambers. The trajectory bend is in the r-z plane. The muon entrance point is measured by the first layer (A layer), which consists of four planes of drift tubes mounted outside the calorimeter cryostats and just inside the magnets. The second layer (B layer), with three planes of drift tubes, is positioned outside of the magnets. A third layer (C layer), with three planes of drift tubes, is separated from the B layer by 1-3 m of air space. Not all regions have complete C layer coverage, because of mounting difficulties. The initial trajectory of the muon is reconstructed from the interaction vertex, the central tracking hit information, and hit information from the A layer of the muon system. After the muon's path is bent in the magnets, the B and C layers give a second trajectory from which the bend angle is determined.

The Wide Angle Muon Spectrometer (WAMUS) consists of 164 drift tube chambers which cover all of the central toroid and most of the end toroids to $\theta \approx 10°$ [44]. The Small Angle Muon Spectrometer (SAMUS) extends coverage at the high rapidity edge of the end toroids, and covers the SAMUS toroids to a minimum angle of $\theta = 3.4°$.

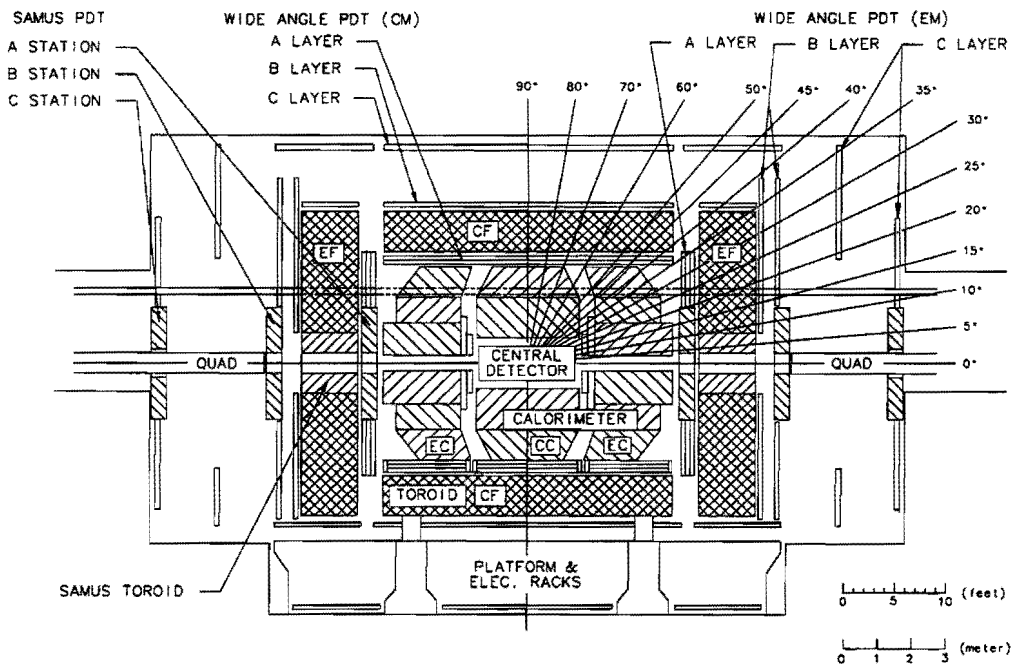

Figure 3.12: The Muon System

A Proportional Drift Chamber works on a similar principle to the PWC discussed in the earlier section on the Vertex Chamber. However, by allowing ionization electrons to drift over a greater distance in a low electric-field before reaching the amplification region close to the anode wire, far fewer wires and readout channels are required to instrument the large area covered by the muon system. Since the chamber occupancy (average track density) is low, longer drift times are not a problem as they would be in the central tracking system.

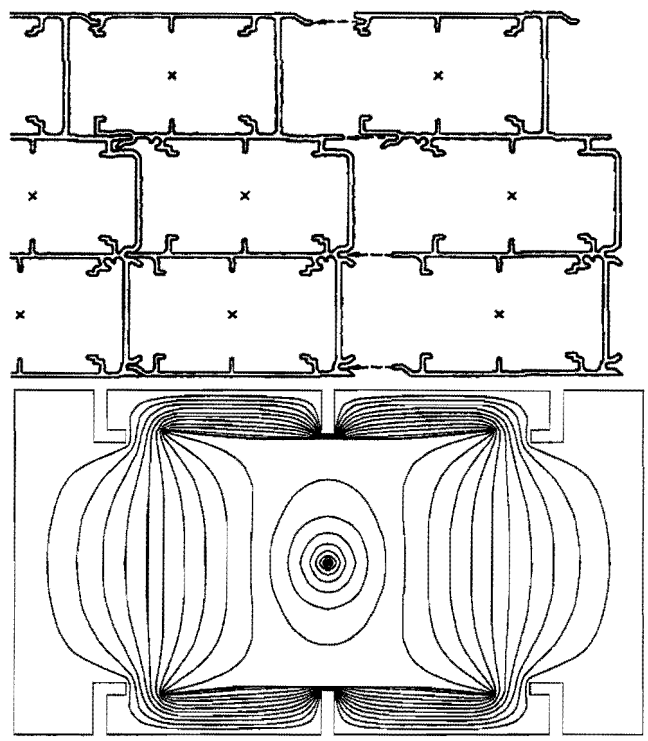

Fig. 4 ELECTROSTATIC EQUI-POTENTIAL LINES OF 4" PDT CELL SIGNAL WIRE AT +5 KV, AND VERNIER PADS AT +2 KV

Figure 3.13: *top:* WAMUS drift cells. *bottom:* A single drift cell shown with equipotential lines.

Each muon drift cell has a single anode wire, held at a potential of +4.54 kV. The maximum drift distance is 5 cm. A measurement of the ionization charge drift time is used to determine the distance of primary ionization from the anode wires

[40]. The location of the primary ionization parallel to the wires is reconstructed from the charge arrival time difference at either end of the anode wires (Δt), and from signals in two vernier cathode pads mounted at the bottom and top of the drift cell. The cathode pads are etched with a repeating elongated diamond pattern. The inside and outside of the pattern are separate electrodes. The electrodes are held at a potential of +2.6 kV.

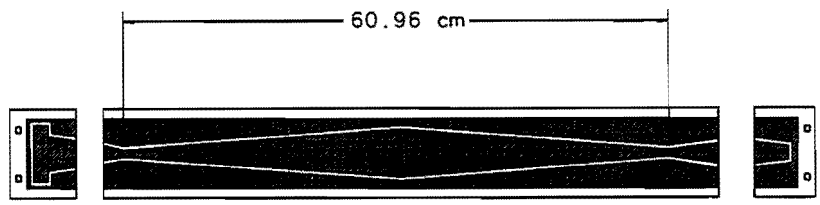

Figure 3.14: A WAMUS vernier cathode pad.

The inner pads are ganged together, and likewise for the outer pads. The ratio of the sum and difference of inner and outer pad charge collection is used to measure the hit position parallel to the anode wires, to within ± 3 mm. The Δt measurement from the anode wire resolves left-right ambiguity. The drift tube cells (Fig. 3.13) are constructed of aluminum. Anode wires are 50μm gold-plated tungsten, and cathode pads are copper clad Glasteel. The chamber gas mixture is $Ar(90\%)CF_4(5\%)CO_2(5\%)$, which gives an electron drift velocity of $\approx$ 6.5 cm/μs [45],[46],[16].

DØ Muon System	
η coverage	WAMUS ± 1.7, SAMUS 1.7-3.6
Magnetic Field Strength	1.9T
$\delta P/P$	20% ($P < 80$ GeV/c)
Thickness in Λ (90°)	13.4
Thickness in Λ (5°)	18.7
Resolution $\perp$ to sense wire	$\pm$0.2mm ($\pm$0.6mrad)
Resolution $\parallel$ to sense wire	$\pm$2.0mm

Table 3.3: The muon system design parameters.

CHAPTER 4

DATA SELECTION

4.1 Cross Sections and Luminosity

Much of the following discussion of DØ luminosity measurements may be found in [47].

In the context of particle physics, a cross section σ is a measure of the probability for an interaction to occur. Its units are units of area, expressed in terms of "barns" (1 barn $\equiv 10^{-28}\ m^2$, millibarn:mb $= 10^{-3}$ barns, picobarn:pb $= 10^{-12}$ barns, etc.). A cross section is related to the interaction rate $\dot{N}$ by

$$\dot{N} = \sigma \dot{\mathcal{L}} \tag{4.1}$$

where $\dot{\mathcal{L}}$ is the instantaneous luminosity, defined by this equation. The instantaneous luminosity $\dot{\mathcal{L}}$ of a colliding beam accelerator for two antiparallel beams of relativistic particles is given by:

$$\dot{\mathcal{L}} = fn\frac{N_1 N_2}{A} \tag{4.2}$$

where f is the revolution frequency of the beam particles, n is the number of particle bunches in either beam, A is the effective cross sectional area of the overlap between the beams, and N_1 and N_2 are the number of particles in the opposing bunches [48]. For the Tevatron accelerator at Fermilab, which provides the $p\bar{p}$ collisions in both the DØ and CDF experiments, a typical instantaneous luminosity value for the 1991-92 collider run (during which the data for this analysis were collected) was $\sim 10^{31}\ cm^{-2}s^{-1}$. The integrated luminosity is a quantity which determines the total number of events selected in a data taking period, given by:

$$\mathcal{L} = \int dt \dot{\mathcal{L}}, \tag{4.3}$$

where the integral is over the time during which the detector is fully enabled and taking data.

Equation 4.1 may be inverted, to determine the luminosity from the rate of a process whose cross section is known. Each process has its own characteristic cross section. The cross section which is used in the calculation of the luminosity in the DØ experiment is for the combination of all scattering processes which are detectable by the Level 0 trigger, to be described in the next section, multiplied by the efficiency with which they are detected. This cross section is called "minimum bias", because it is an attempt to trigger on typical $p\bar{p}$ events while introducing the least possible bias due to selection conditions. The minimum bias cross section σ_{MB} is determined by using measurements from other experiments of the cross sections of contributing processes and by performing Monte Carlo simulations of these processes in the DØ environment to measure the efficiency with which they pass the Level 0 (L0) trigger (described in Section 4.2.1) [54]. These processes are a subset of the total cross section for all $p\bar{p}$ interactions.

The total cross section σ_{tot} has an elastic (σ_{el}) and inelastic (σ_{in}) part:

$$\sigma_{tot} = \sigma_{el} + \sigma_{in}. \tag{4.4}$$

The elastic part refers to those interactions in which the colliding beam particles remain intact. These interactions occur mainly at low momentum transfer Q^2, and are not seen in DØ because there are no secondary particles on which to trigger. The scattered particles are not deflected with sufficient transverse momentum to leave the beam pipe. The inelastic part refers to those interactions in which new particles are produced and the beam particles break apart.

The inelastic cross section is divided into categories:

$$\sigma_{in} = \sigma_{SD} + \sigma_{DD} + \sigma_{HC}, \tag{4.5}$$

where SD denotes single diffractive interactions ($\sigma_{SD} \approx 9.5mb$), DD denotes double diffractive interactions ($\sigma_{DD} \approx 4.9mb$), and HC denotes hard core interactions ($\sigma_{HC} \approx 44.5mb$). In diffractive scattering, new particles are produced, but the interaction is not at the parton level. The partons in the beam particle scatter coherently. A single(double) diffractive interaction occurs when one(both) beam particle(s) is excited and decays into stable final state particles. The "particle" which is exchanged (technically not a particle but a "Regge trajectory" [49]) is commonly referred to as a "pomeron" α_P, after the physicist Pomeranchuk, who first postulated its existence. No quantum numbers other than angular momentum are transferred, so the pomeron has the quantum numbers of the vacuum. The pomeron is also the entity which is exchanged in elastic collisions. In a hard core interaction, the momentum transfer is between individual partons in the beam particles. The partons which are not directly involved in the momentum transfer are called "spectators". At $Q^2 \gtrsim 2\ GeV^2$, diffractive effects become very small and parton-level interactions are dominant. The world average for the inelastic cross section $\sigma_{inel} = 58.9mb$ comes from the E710 [50] and CDF [51][52][53] measurements.

The minimum bias cross section is given by:

$$\sigma_{MB} = \epsilon_{vert}(\epsilon_{SD}\ \sigma_{SD} + \epsilon_{DD}\ f_{DD}(\sigma_{IN} - \sigma_{SD}) + \epsilon_{HC}\ (1 - f_{DD})(\sigma_{in} - \sigma_{SD}). \quad (4.6)$$

The symbol ϵ_{vert} is the efficiency for finding a vertex within the accepted range in the Z coordinate. A vertex position cut is imposed at approximately 3σ from the center of the detector in the interaction Z distribution, estimated by fitting to a gaussian function ($|Z| < 97cm$). The symbol f_{DD} is the DD fraction of HC+DD ($\approx 10\%$). The symbols $\epsilon_{(SD:DD:HC)}$ are the efficiencies (5% : 84% : 99%, respectively) for detecting the inelastic reactions with the L0 trigger. Detection efficiencies for single diffractive, double diffractive, and hard core interactions are determined by Monte Carlo simulation. The minimum bias cross section for DØ is 48.2 mb.

The uncorrected measurement of the instantaneous luminosity $\dot{\mathcal{L}}_{meas}$ is related to the counting rate in the L0 counters R_{L0} by:

$$\dot{\mathcal{L}}_{meas} = \frac{R_{L0}}{\sigma_{MB}}. \tag{4.7}$$

At low luminosity, the counting rate R_{L0} is the same as the interaction rate $\dot{N}$, of (4.1). As the luminosity increases, the average number of interactions which occur in a single bunch crossing is more than one, so the luminosity must be corrected for multiple interactions. In a given data taking period, the number of bunch crossings in which no minimum bias interactions occur is N_0 and the total number of bunch crossings is N_{tot}. It is assumed a priori that the number of interactions per crossing follows a Poisson distribution, so the average number of interactions per crossing $\bar{n}$ is found from the expression for the probability of zero interactions in a beam crossing $P(n_0)$ (see Section 9.2), given by:

$$P(n_0) = \frac{N_0}{N_{tot}} = \frac{\frac{e^{\bar{n}}\bar{n}^0}{0!}}{\sum_{i=0}^{\infty} \frac{e^{\bar{n}}\bar{n}^i}{i!}}. \tag{4.8}$$

The correction factor relating the instantaneous luminosity $\dot{\mathcal{L}}$ to the uncorrected $\dot{\mathcal{L}}_{meas}$ of (4.7) is given by:

$$\frac{\dot{\mathcal{L}}}{\dot{\mathcal{L}}_{meas}} = \frac{\bar{n}}{1 - e^{-\bar{n}}} = \frac{-\ln(1 - \dot{\mathcal{L}}_{meas}\ \tau\ \sigma_{MB})}{\dot{\mathcal{L}}_{meas}\ \tau\ \sigma_{MB}}, \tag{4.9}$$

where τ is the crossing time ($\tau = 3.5\ \mu s$). The integrated luminosity as determined from minimum bias events is given by

$$\mathcal{L} = f\ \bar{n}\ t_{live}/\sigma_{MB} \tag{4.10}$$

where $\bar{n}$ is the average number of minimum bias interactions per crossing, $f = 1/\tau = 286275 sec^{-1}$ is the beam crossing frequency, t_{live} is the "live" time (detector is active) in seconds, and σ_{MB} is the minimum bias cross section.

The quantities f, and t_{live} are measured with information from the detector monitoring and beam monitoring. The quantity $\bar{n}$ is derived from L0 measurements of

N_0 and N_{tot} for each data taking period. The dominant errors in the measurement of the integrated luminosity arise from the uncertainty in the world average measurement of the inelastic cross section ($\approx 4\%$) and from the uncertainty in the efficiency of the DØ detector for triggering on the contributing inelastic processes ($\approx 1\%$). The total error ($\approx 5\%$) is propagated into the determination of the confidence limits on the excited quark cross section described in Section 9.3.

4.2 The DØ Trigger System

A typical luminosity for the DØ experiment during the 1992-93 collider run was $\dot{\mathcal{L}} \approx 2 \times 10^{30}\ cm^{-2}s^{-1}$. The minimum bias cross section σ_{MB} is ≈ 48 mb, yielding a minimum bias counting rate of $\sigma_{MB} \times \dot{\mathcal{L}} = 96$ kHz.

Over the course of the 1992-93 collider run, that collected an integrated luminosity of $\mathcal{L} \approx 13\ \mathrm{pb}^{-1}$, this is $\sim 10^{12}$ interactions. These are too many data to store, accumulating at a rate which is too high to handle. However, only a small part of this sample is directly relevant to the analyses which were investigated in this experiment. In order to reduce the total sample of inelastic collisions to a manageable and meaningful subset, DØ has a multilevel triggering system, designed to collect and record only interesting events.

4.2.1 Level Zero (L0)

The purposes of the Level Zero trigger are to identify inelastic $p\bar{p}$ interactions, to provide a rough measurement of the z coordinate of an interaction vertex, to detect multiple interactions in a single beam crossing, and to measure the luminosity.

The interaction time and vertex position are measured by two arrays of scintillation counters (hodoscopes) mounted on the faces of the end calorimeter cryostats.

The counter arrays are arranged in two overlapping layers, rotated by 90° with respect to each other, and perpendicular to the beam pipe. A layer consists of 10 short scintillators (7 cm × 7 cm), each coupled at one end to a photomultiplier tube, and four long scintillators (7 cm × 65 cm), coupled to photomultiplier tubes at both ends. The array completely surrounds the beampipe to maximize rapidity coverage, which is partial over $1.9 < |\eta| < 4.3$ and nearly complete over $2.2 < |\eta| < 3.9$. $p\bar{p}$ interactions are detected when particles from an inelastic collision cause synchronous hits in the north and south scintillator arrays. The time of flight resolution of this configuration is $\sigma_t < 150$ps, as determined by cosmic ray tests.

The output of L0 is a Fast Vertex position, available 400ns after beam crossing, which is derived from the time difference between signals in the north and south arrays. The Fast Vertex information is used by the Level One calorimeter trigger to correct $\sin\theta$ tables for vertex offsets from the Z=0 projective geometry. A Slow Vertex position is also calculated, available 2μs after beam crossing, which averages the interaction time time over signals from all photomultipliers in the array and corrects for systematic effects to yield a more accurate measurement of the vertex position. For a single interaction in a beam crossing, the position resolution in the Z coordinate is ± 3.5 cm.

L0 tags events with no interactions in a crossing, multiple interactions in a crossing, and bad vertex position outside of $|z| < 96$ cm. L0 also monitors the luminosity by counting the rate of synchronous hits in the north and south scintillator arrays [55],[56].

4.2.2 Level One (L1)

The Level One Trigger Framework is a hardware-based logic system. It accepts as input the L0 vertex position and timing, information from the calorimeter and muon system, and timing information from the accelerator. The Trigger Framework uses this information to determine whether to keep the event for further processing

or to reject it. For an event to pass L1, it must satisfy at least one of 32 trigger conditions, corresponding to 32 available "trigger bits", each of which is a logical combination of up to 256 programmable AND/OR input terms, configured together to accept only one type of interesting event. The L1 trigger information from which photons are selected in this analysis is primarily from the calorimeter.

The calorimeter is divided into 1280 trigger "towers", covering the range $|\eta| < 3.2$ in pseudorapidity and 2π in azimuth. A trigger tower consists of all the calorimeter cells contained in a 0.2×0.2 unit of solid angle in $\eta \times \phi$ space (4 calorimeter cells in area), projecting outward from the center of the detector. The calorimeter information at L1 is the transverse energy, $E_T = E \sin\theta$, deposited in each tower. The energy is measured separately as an electromagnetic part, deposited in the EM layers, and a hadronic part, deposited in the FH and CH layers. This information is used to reconstruct "global" quantities and "seed towers" for L2 to use in clustering. Global quantities include the total E_T, which is the scalar sum of all tower $E_T's$; the electromagnetic and hadronic $E_T's$; and the total missing E_T (MET), which is the magnitude of the vector sum of all tower $E_T's$. L1 uses not only global quantities from the calorimeter, but also the E_T deposited in individual trigger towers. If the electromagnetic E_T of a trigger tower is above a threshold, this tower is identified as a seed site to look for electromagnetic showers. If the total E_T of a trigger tower is above another threshold, the tower is identified as a seed site to look for jets [58],[59].

The L1 Trigger Framework has $\approx 3.5\mu s$ between beam crossings to decide whether to keep an event. There is not enough time for elaborate event reconstruction algorithms, and the output rate from L1 is still too high for storage.

4.2.3 Level Two (L2)

An event passing L1 is further tested by the Level Two trigger system. Both L0 and L1 are hardware based systems. L2 is software based, and can examine an

event in greater detail. Data from L0, L1, the calorimeter, the tracking systems, the ICD, and the muon detectors are processed by a farm of 48 VAXstation 4000-60's, which performs preliminary event reconstruction. Each trigger bit in L1 has one or more "event filters" associated with it at L2. Software algorithms, called "tools", are used to calculate event quantities (E_T, η, etc.). A filter uses a combination of these tools to characterize a special type of event, like a top quark candidate. There were 128 filters available. If an event passes any one of them, all raw data from the DØ Detector are stored to a hard disk and then written to an 8mm data tape.

The maximum input rate to L2 is 200 Hz and the maximum L2 output rate that can be stored is 1-2 Hz (the output "bandwidth"). Throughput is controlled by "prescaling" the individual triggers to a manageable total rate, appropriate to definitions of the trigger conditions, and within one set of conditions. For example, if a trigger is prescaled by a factor of 10, only every tenth event which passes is processed further at L2. The other 9 events are discarded. The total output bandwidth from L2 is divided among physics groups according to topical priority, and the sample size needed to complete an analysis. Prescales are used to balance the bandwidth allocations, and are adjusted as the instantanteous luminosity changes to optimize data-taking efficiency [60],[61].

4.3 Photon Triggers

The prompt photon cross section decreases exponentially with increasing E_T. To populate the E_T distribution with adequate statistics, we used three triggers with different thresholds and prescale factors. The three triggers selected events which had greater than 4.5, 7, or 14 GeV of EM energy in a single trigger tower. The photon events which passed the lowest energy trigger were all collected in a

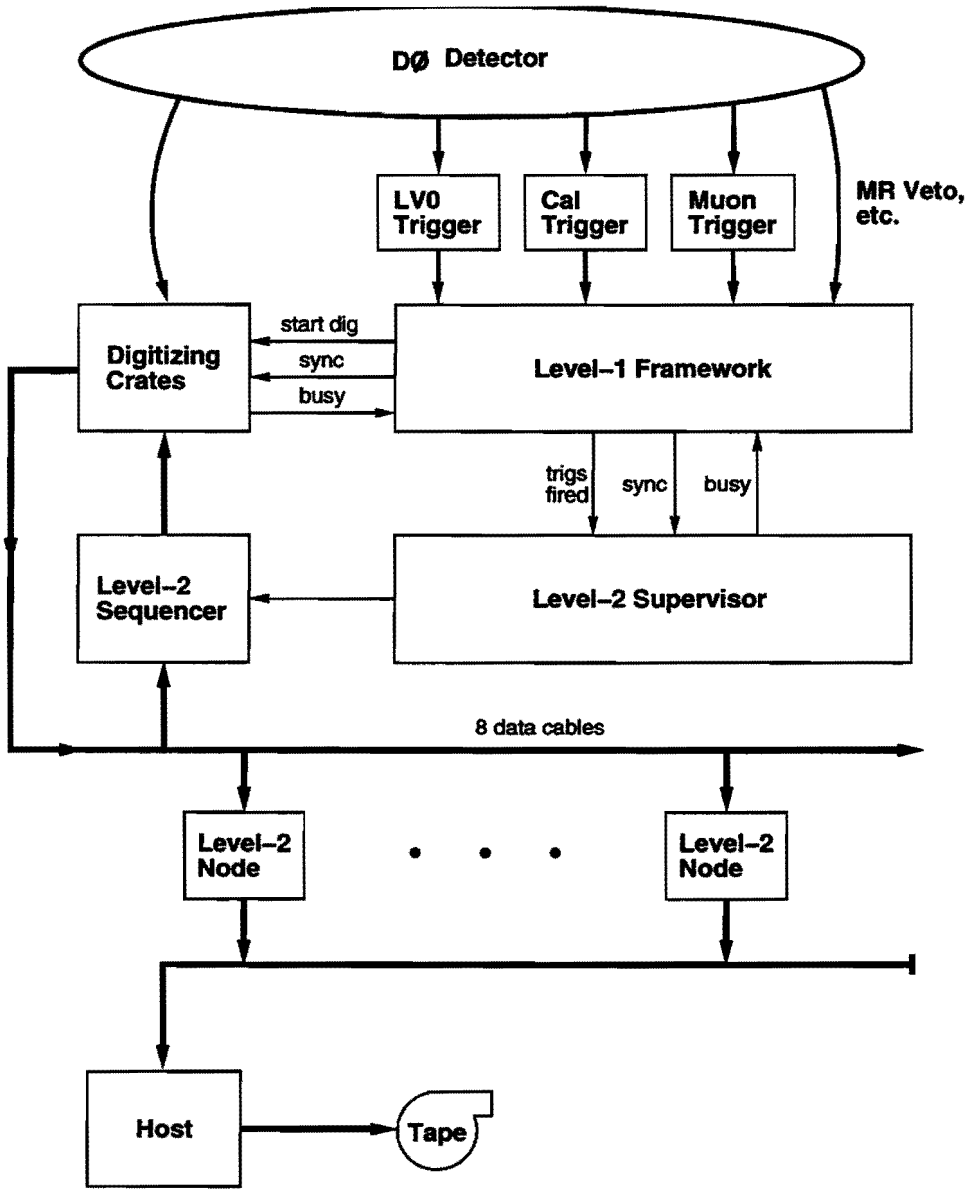

Figure 4.1: The DØ Trigger System

single special run, while the other two triggers collected photon events over all runs. The medium energy trigger was prescaled, and the highest energy trigger was unprescaled. We used an additional L1 trigger to collect diphoton events, which required 7 GeV of EM energy in each of two trigger towers.

We changed the trigger energy thresholds and prescales over the course of the run to make the best use of our allocated trigger bandwidth. All of the data used in this mass analysis comes from the highest energy photon trigger. This trigger first had an energy threshold of 14 GeV E_T, during which about $1.8pb^{-1}$ of data were collected. The threshold was lowered to 12 GeV for about $2.2pb^{-1}$ of data collection, and lowered again to 10 GeV for the remaining $11pb^{-1}$ of data collection.

When a photon showers in the calorimeter, the energy deposited in a trigger tower is only approximately proportional to the total energy of the photon. Some photon events with energies above the trigger threshold will not pass, while some which have energies below threshold will pass, because shower development is subject to fluctuations. A photon may deposit more or less of its energy inside a single trigger tower. The trigger efficiency as a function of photon E_T is less than 100% at the threshold value, rising to approach full efficiency several GeV above. This effect is called trigger turn-on. The energy thresholds at L2 are considerably higher than at L1, so that data will only be saved in the energy range where a trigger is fully efficient, and also because the L2 energy measurement is more accurate. The turn-on efficiency for a trigger is estimated by looking at data taken with a trigger that has a lower threshold. The highest energy photon trigger at L1 is named EM_1_HIGH, and the next lowest energy trigger is EM_1_MED. The efficiency of EM_1_HIGH as a function of EM trigger tower E_T is given by:

$$\epsilon_{EM_1_HIGH} = \frac{N_{EM_1_HIGH+EM_1_MED}}{N_{EM_1_MED}}. \tag{4.11}$$

where $N_{EM_1_MED\cdot EM_1_HIGH}$ is the number of events passing both the triggers EM_1_HIGH and EM_1_MED, and $N_{EM_1_MED}$ is the number of events passing the

trigger EM_1_MED. This distribution is shown in Fig. 4.2. The high trigger becomes fully efficient at about 20 GeV, where $\epsilon_{EM_1_HIGH}$ approaches 1.

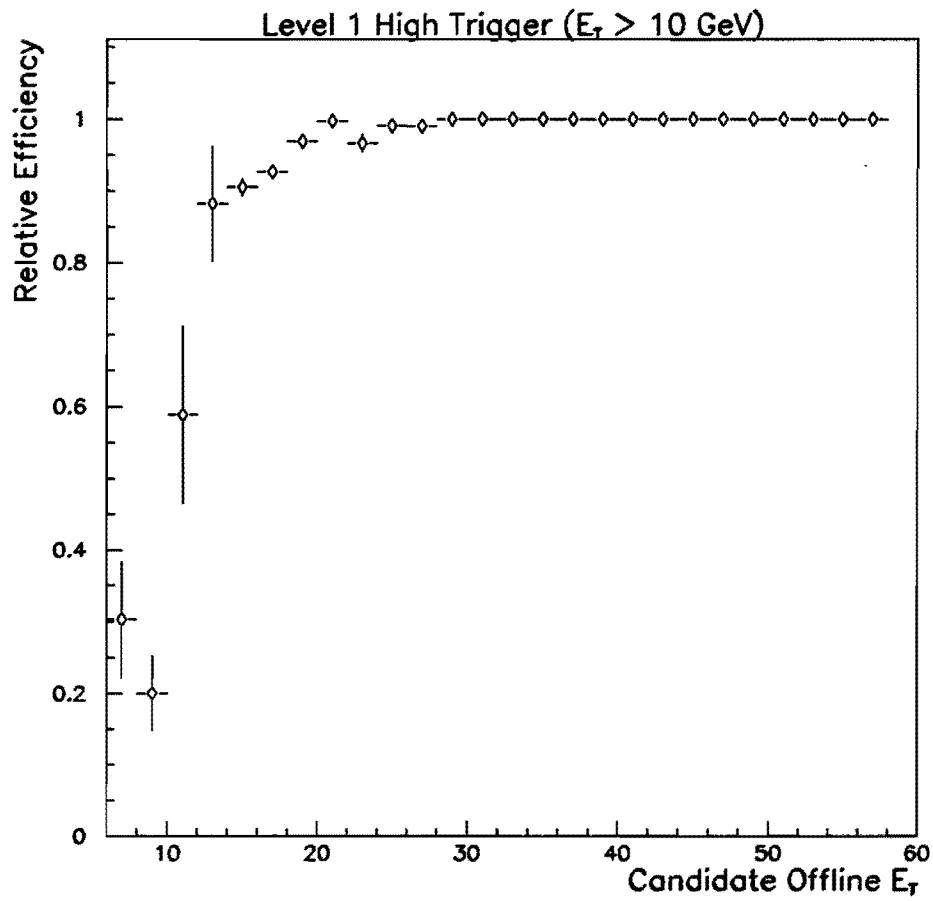

Figure 4.2: The efficiency of the EM_1_HIGH trigger vs. photon E_T.

We set L2 E_T thresholds of 6, 14, and 30 GeV for the single photon filters and 12 GeV for the diphoton filter. The turn-on efficiency for the highest energy L2 filter is shown in Fig. 4.3. A software-based filter tool performs rudimentary calorimeter "clustering", adding the energy of calorimeter cells in which the photon showered. A tool determines the fraction of shower energy which is electromagnetic, and compares

with distributions from test beam electrons. The EM shower from a prompt photon should be well isolated from surrounding hadronic showering. A projective cone is constructed around the seed tower, of radius $R = \sqrt{\Delta\phi + \Delta\eta} = 0.4$, where $\Delta\phi$ and $\Delta\eta$ are displacements from the center axis of the seed tower in the ϕ and η coordinates. This is the isolation cone. The total transverse energy deposited in the isolation cone which is not in the seed tower must be less than 15% of the energy in the seed tower.

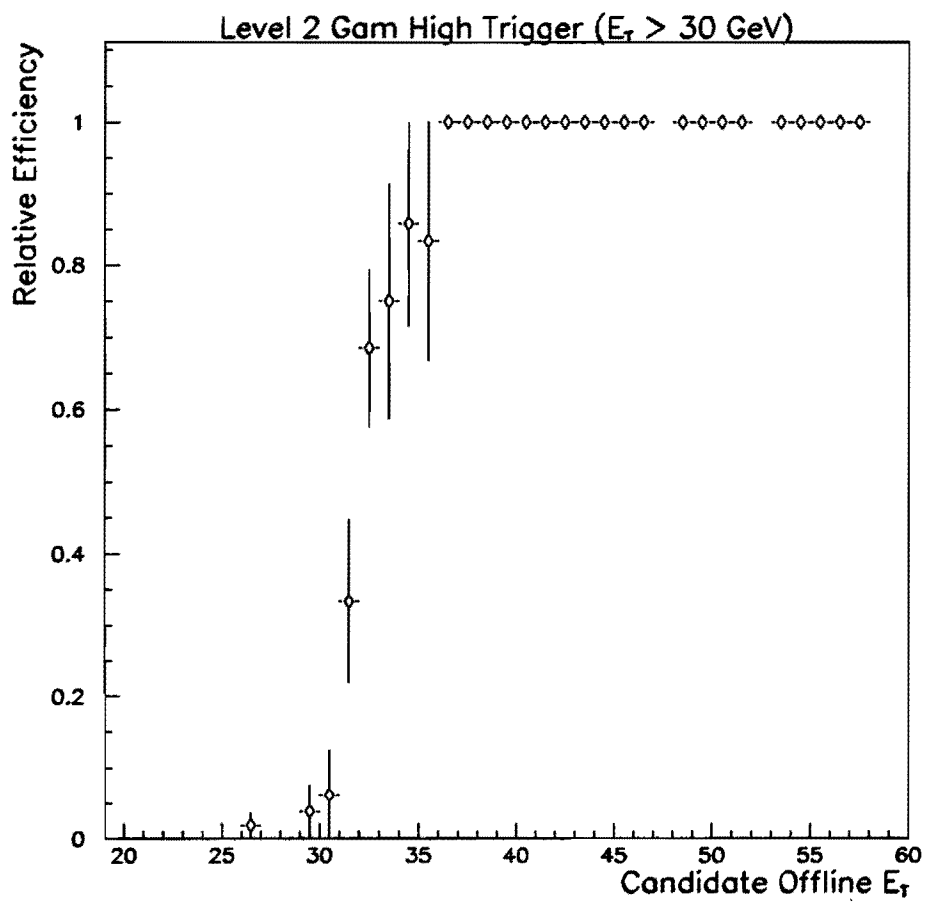

Figure 4.3: The efficiency of the GAM_HIGH_ISO filter vs. photon E_T.

"Offline" refers to analysis performed after data have been collected and saved during a run. We impose offline energy thresholds which are higher than L2 thresholds, to avoid regions of L2 trigger turn-on.

4.4 Offline Event Reconstruction and Storage

Raw data are collected in the form of digitized pulses from the various detectors. These data must be reinterpreted in terms of physics quantities, like jet energies and particle track positions. The software package that performs event reconstruction is called DØRECO. It contains hundreds of algorithms and subprograms, written by many physicists over a period of years. Reconstruction algorithms are tested and debugged with Monte Carlo data, data from the 1991 test beam run, and collider data.

DØRECO is constantly being revised and updated, so a reconstructed data set is identified with the DØRECO version number that it was processed with. Raw data which are written to tapes during experiment running was processed by a UNIX-based farm of 42 SGI Indigo machines, each rated at 35 MIPS (millions of instructions per second) [62]. A "farm" in this context is a group of computers which work on the same task together in parallel, with a single "master" machine allocating tasks and controlling input/output for several "slave" machines. The data set used in this analysis was almost all processed with DØRECO version 11.19, the final version used in run 1A.

The energy deposited by a photon in the calorimeter is reconstructed as a "cluster" of electromagnetic energy. Any EM calorimeter cell with energy above a threshold of 1.5 GeV is targeted as a seed-cell for clustering. A calorimeter cell adjacent to the seed-cell with the most deposited energy of all adjacent cells is added to the

cluster. A calorimeter cell adjacent to either of the two cluster cells with the most energy of all remaining adjacent cells is added, and so on, until no cells adjacent to the cluster have greater than 50 MeV of deposited energy. The sum of cluster cell energies, after subtraction of energy due to electronic noise, is interpreted as the energy of the photon. This strategy for energy reconstruction is the "nearest-neighbor" algorithm [63],[64],[65].

The direction of a photon is reconstructed from the event vertex and the position of the EM cluster associated with the photon. The energy from an electromagnetic shower is deposited in several calorimeter cells, forming a cell cluster. The energy distribution in the cell cluster falls off exponentially with distance from the center of the shower, in the plane orthogonal to the photon momentum vector. The shower centroid is determined by averaging over the positions of the cells in the cluster. It seems intuitive that cluster cells should be weighted as a simple ratio of the cell energy over the cluster energy. If this weighting system is used, the outer cells of the cluster will have very little weight, and the position resolution will be limited by the width of the smallest cell. The energy distribution on the periphery of the shower actually contains the most information about the shower shape and position. To take into account the exponential falloff in the energy distribution, a logarithmic cell weighting scheme is used which gives greater weight to the outer cells [39],[66]. The centroid position of an EM shower is defined by:

$$\eta_{centroid} = \frac{\sum W_i \cdot \eta_i}{\sum W_i} \quad \text{and} \quad \phi_{centroid} = \frac{\sum W_i \cdot \phi_i}{\sum W_i}, \tag{4.12}$$

where

$$W_i = max \ \{0, [\ln(\frac{E_i}{\sum E_i}) + W_o]\}. \tag{4.13}$$

The summation is over cluster cells in EM layer 3, where the peak energy deposit of electromagnetic showers occurs and the calorimeter segmentation is the finest. The parameter W_o sets the energy cut-off scale at which cells are dropped from the

summation. Through Monte Carlo studies, its optimal value was determined to be 5.5 for electron showers of E_T greater than 50 GeV.

Jets are reconstructed from calorimeter information using a cone algorithm. An E_T ordered list is made of $\Delta\eta \times \Delta\phi = 0.1 \times 0.1$ jet seed (calorimeter) towers. Starting with the highest E_T seed tower, preclusters are formed of calorimeter cells adjacent to the seed tower out to a radius of $R = \sqrt{\Delta\eta^2 + \Delta\phi^2} = 0.3$ The E_T weighted center of a precluster in $\eta \times \phi$ space is the center of a jet cone of size $R = 0.7$. A new E_T weighted center is formed from the cells in this jet cone, and a new jet cone is constructed around the new center. The center-finding process is repeated through several iterations until the center stabilizes. The jet center gives the direction of the momentum vector of the jet. The E_T of all calorimeter cells in a $R = 0.7$ cone around the center is defined as the energy of the jet. Energy and position dependent corrections are made to this definition. Corrections are also made to share energy between two closely adjacent jets, or merge them into a single jet [67].

4.4.1 STA and DST Data Formats

DØRECO produces two forms of output, STA files and DST files. A standard output file (STA) contains reconstructed quantities and raw data information. Its large amount of retained information per event makes it an impractical format for data analyses which require large statistical samples. An STA file contains all the necessary information to be used as input for reprocessing with future versions of DØRECO. A data summary tape file (DST) (not necessarily stored on a tape) contains reconstructed physics quantities only. It occupies less storage space than an STA file of the same events and contains enough information for most event analyses.

4.4.2 Streaming

The entire data set from the 1992-93 collider run is prohibitively large ($\sim 10^7$ events). Each analysis is concerned only with a small part of the total data set, so data are divided into multiple output "streams" according to physics category and rewritten to separate tapes. Streaming was done on two SGI Crimson machines. The QGA (QCD gamma) stream contains photon data.

4.4.3 Ntuples

The QGA stream DST's are a small enough data sample to fit on hard disk, but there is another format for storing data that is more convenient to access for analysis, the "Ntuple". An Ntuple is a two dimensional array. In one dimension are N number of physics quantities which describe an event, and in the other dimension are all of the events in the sample [68]. An Ntuple is easy to code, and may be customized, containing only the variables which will be used in a single analysis, thereby conserving storage space and access time. Ntuples can be accessed directly through the program PAW (Physics Analysis Workstation) [69] to view variable distributions in one or more dimensional histograms. The information in an Ntuple is stored in parallel, by which it is convenient to place selection criteria on the data, or to combine variables in a formula. The prompt photon data set for the 1992-93 collider run is stored in 15 Ntuples containing 157 variables and occupying less than 2 Mbytes of space.

CHAPTER 5
OFFLINE ANALYSIS

The event sample taken by the photon trigger contains many background events where fragmentation of final state partons creates hard π° and η mesons, which decay to an almost collinear photon pair. To minimize background contamination and to control event quality, appropriately defined analysis cuts are applied to the event sample. Events passing a cut are retained in the sample. The efficiencies of cuts are estimated in studies of experimental data and Monte Carlo simulated event samples.

Efficiencies of cuts on jet related quantities are determined with complete two-body simulated Monte Carlo events. Jets take more time to simulate than EM showers, so Monte Carlo event samples are simulated which contain a single isolated photon with no balancing jet to achieve better statistics for efficiencies which do not concern jets. Each cut described in this chapter is labeled with a number and is listed in Table 5.1. The efficiencies given are sequential; that is, each cut efficiency is defined as the number of events in the sample which pass the cut plus all preceding cuts, divided by the number of events in the sample which pass all preceding cuts. It is elusive to determine errors on the reconstructed quantities associated with the Monte Carlo modeling. The errors given in table 5.1 are statistical only, determined by the size of the event sample from which each efficiency is estimated.

5.1 Geometric Acceptance

"Acceptance" is a general term referring to the instrumented volume of the detector which is sensitive to the passage of particles, and to the energy and position conditions which are imposed by the experimentalist to insure that detection efficiency is uniform and errors are calculable. Geometric acceptance is the fraction of coordinate space which is fully efficient for detecting particles. For the pseudorapidity of the photon and leading jet, I require $|\eta| < 3.2$. This cut is to ensure good jet position resolution. As pseudorapidity increases, the size of a unit of pseudorapidity decreases (3.1). Calorimeter cells occupy a fractional unit of pseudorapidity, usually equal to 0.1. As the unit cell size decreases, the jet position resolution degrades. The efficiency for this cut is not given. It is also applied in the theoretical calculation of the cross section to which the data are compared.

5.1.1 Fiducial Cuts

(1) Photon rapidity

The fraction of photon-like showers in the event sample which come from real photons can be measured most accurately for photons in the central calorimeter. In the end calorimeters, structural support material and read-out cables cause a nonuniform density of material between the central vertex and the forward drift chamber. Knowledge of the number of radiation lengths of conversion material is critical for an accurate measurement of the photon purity, as discussed in section 5.7.

A cut is applied, accepting only events where the photon is within ± 0.9 in detector pseudorapidity. "Detector" pseudorapidity is distinguished from "physics" pseudorapidity in that the former has its origin at coordinate $Z = 0$, while the origin of the latter varies with the Z position of the interaction vertex. Electromagnetic showers within this limit are fully contained in the central calorimeter, which extends to $|\eta^{detector}| = 1.1$. Some of the photons within this range are lost in the cracks between the calorimeter modules, where they lose substantial amounts of energy in dead material and are not reconstructed. The efficiency given for this cut is the

fraction of the total number of photons with $|\eta| < 0.9$ which are reconstructed with $|\eta^{detector}| < 0.9$.

The dimensions of the double-differential cross section $\frac{d\sigma}{dp_T}$ are picobarns per unit p_T per unit η. To account for acceptance limitations in η, the single differential cross section $\frac{d\sigma}{dp_T}$ is usually divided by the available η range, which is (-0.9 to 0.9) 1.8 for an event whose vertex is at $Z = 0$. Events with a vertex at a large displacement from $Z = 0$ have a smaller effective η range. At a maximum displacement of 50 cm, the range is 1.7. To avoid this minor acceptance overestimate, the effective η range is calculated on an event by event basis. The Z coordinate of the interaction vertex is the origin, and two vectors are determined between this origin and the effective ends of the EM calorimeter, at ± 0.9 in detector η. The space between the vectors is the effective η range ($\Delta\eta$) for an event. In the double-differential cross section measurement $\frac{d\sigma}{d\eta dM}$, each event is weighted by $1/\Delta\eta$ to give the correct effective range of pseudorapidity available for the photon to shower into. The mass fitting analysis for the excited quark search is not concerned with the absolute normalization of the mass distribution, so all events have an equal weight of 1.

(2) Interaction Vertex Position

I require the Z coordinate of the interaction vertex to be within 50 cm of the center of the detector (Z=0). The calorimeter is designed with cells extending from the center in pseudoprojective towers in the polar angle, and events are triggered on the energy deposited in the towers. As the interaction vertex shifts away from the projective origin, trigger efficiency degrades, because a photon will deposit its energy in more than one trigger tower. Vertex offsets from the center will also cause the energy and position resolution to degrade on the side of the detector opposite the offset. The angle between the shower centroid and the plane of the calorimeter plates becomes smaller on this side. With decreasing angle, the sampling interval becomes larger, as $1/\cos\theta$, and plate edge effects cause shower nonuniformity.

5.2 Energy Threshold Cuts

(3) E_T of the photon

Events must contain at least one photon and one jet, as found by the offline reconstruction package, DØRECO. The photon E_T is required to be greater than 35 GeV, to avoid poor efficiency in the energy region of trigger turn-on. The high E_T photon trigger has a threshold of 30 GeV. Because of energy measurement fluctuations, electromagnetic showers from photons of less than 30 GeV at the particle level will pass this threshold and some photons of greater than 30 GeV will not pass. Figure 4.3 shows, as a function of photon E_T, the ratio of events which passed the medium and the high E_T photon triggers over those which passed the medium trigger. The high E_T trigger becomes fully efficient when this ratio approaches 1, which it is seen to do above 35 GeV.

(4) E_T of the leading jet

The E_T of the most energetic jet in the event, commonly called the "leading jet", must be greater than 20 GeV. The trigger used to collect this data sample doesn't require jets; they are found in the offline reconstruction. Jet reconstruction efficiency approaches 100% at energies above 20 GeV E_T [70][71].

5.3 Jet cuts

(5) EM fraction of jets

A cut is made on the fraction of energy in the leading jet which is deposited in the electromagnetic calorimeter. This EM fraction (EMF) is defined as the EM energy divided by the total jet energy, and it is required to be not less than 0.05 and not greater than 0.95. This cut reduces the number of fake jet entries which are constructed from noisy calorimeter cells. [72]

5.4 Photon cuts

(5) Isolation energy of the photon

The EM shower from a prompt photon is required to be well isolated from surrounding hadronic activity. A projective cone is constructed around the shower centroid, of radius $R = \sqrt{\Delta\phi + \Delta\eta} = 0.2$. This is the center cone, and should fully contain the photon energy. An isolation cone of radius $R = 0.4$ is constructed around the center cone (as in the L2 trigger, but centered on the shower centroid rather than the seed tower). The total transverse energy deposited in the annulus between the two cones is required to be less than 2 GeV. A photon from a leading order process should pass this cut easily, regardless of its energy. This cut is a transverse isolation cut, referring to the energy distribution in the plane perpendicular to the photon momentum vector.

(7) EM fraction of the photon cluster

A cut similar to the jet EMF cut is made on the photon cluster. The fraction of the total transverse energy in the center cone of the photon cluster which is contained in the electromagnetic calorimeter must be greater than 0.96. EM clusters with excessive energy in the hadronic calorimeter are more likely to be jets with a large electromagnetic energy component than to be photon showers. This cut is a longitudinal isolation cut, referring to the energy distribution along the direction of the photon momentum vector.

(8) Photon shower shape - "SPREAD"

A cut is applied in the photon shower shape variable named SPREAD, which expresses the energy distribution of the cluster in the plane perpendicular to the momentum vector. As with the weighting scheme used to define the cluster centroid, cells at the outer edge of a shower receive greater proportional weight. The definition

of SPREAD is given by:

$$SPREAD = \sum[\ln(\frac{E_i}{\sum E_i}) + W_o] \times R_i \times 10, \tag{5.1}$$

where the summation is over all cluster cells in the third layer of the EM calorimeter. $R_i = \sqrt{(\phi_i - \phi_{centroid})^2 + (\eta_i - \eta_{centroid})^2}$ is the distance between a cell and the cluster centroid. $W_o = 5.5$ is a free parameter, optimized in Monte Carlo studies. A cut of $SPREAD < 0.7$ is imposed on the photon cluster. Events with larger SPREAD values are likely to be background, or showers with poor energy resolution because of extra local electronic noise or underlying event energy. A further description of SPREAD may be found in [73].

A variable similar to SPREAD is CIRCULARITY, which is the ratio of the moments of an EM shower in the 2 dimensional space perpendicular to its momentum vector. The weighting scheme is the same as for SPREAD. Photon showers have a CIRCULARITY value close to 1.0, while EM showers from a low momentum π° will be more oblong, having intermediate CIRCULARITY values between 0.0 and 1.0. This variable is promising for discrimination between signal and background. Unfortunately, it is very sensitive to Monte Carlo modeling, and is difficult to calibrate.

(9) χ^2 value of photon shower

A collider event (or part of an event, such as an EM shower) is compared with the signature of a particular type of event using a covariance matrix approach [74] [75],[76],[77]. For a sample of N events, the covariance matrix for a set of observables is defined by:

$$M_{ij} = \frac{1}{N}\sum_{n=1}^{N}(x_{i,n} - \langle x_i \rangle)(x_{j,n} - \langle x_j \rangle), \tag{5.2}$$

where $x_{i,n}$ is the value of an observable x_i for event n, and $\langle x_i \rangle$ is the sample mean of the observable x_i. An "H-matrix" is defined as the inverse of the covariance matrix, $H = M^{-1}$. The H-matrix expresses a signature for the events in a given sample.

The sample may be from a Monte Carlo simulation, from test beam data, or from collider data. The signature of EM showers which is the basis for comparison is taken from measurements of the decay of Z°'s to electrons. To compare a single candidate event with the signature, we calculate the χ^2, defined by:

$$\chi^2 = \sum_{i,j}(x'_i - \langle x_i \rangle) H_{i,j}(x'_j - \langle x_j \rangle), \tag{5.3}$$

where the primed variable indicates the values of observables for the candidate event. The smaller the value of χ^2, the better the agreement between the candidate and the signature.

In the case of electrons, the observables include the fraction of shower energy in EM layers 1,2, and 4; the fraction of shower energy in a 6×6 array of cells in layer three, centered on the tower with the maximum energy; the logarithm of the shower energy; and the position of the event vertex. The H-matrix cut for run 1A prompt photon analyses is a maximum χ^2 value of 100. This cut retains greater than 90% of Monte-Carlo simulated photons over a broad range of photon E_T and η. For the excited quark search mass fitting analysis, a looser χ^2 cut of 200 is used.

(10) Number of cluster cells

The EM shower from a photon is required to have 8 or more calorimeter cells in the cluster. This cut eliminates the majority of background events caused by hot cells (cells with excessive energy deposits from sparking or electronic noise).

(11) Maximum cell energy fraction

The cell in a photon cluster which has the most energy is required to have less than 75% of the total cluster energy **(11)**. This cut is a hot cell discriminant, since photon showers distribute their energy over several cells.

5.5 Additional kinematic cuts

(12) Missing E_T

To get rid of background from cosmic ray bremsstrahlung, a cut is made on the missing E_T in the event. A collider event in which all of the energy was contained in regions of full acceptance, and where this energy was accurately measured, should have very little net transverse energy. The colliding beam particles had negligible transverse energy to start with, so the transverse energy of the final state particles should balance by conservation of momentum. The transverse energy which should be opposite an excess in any direction in ϕ is "missing". The ratio of missing E_T to photon E_T is required to be less than 50% **(12)**. This cut also eliminates events where substantial amounts of the total energy was lost in cracks in the detector, or in dead material which is insensitive to energy loss.

(13) Photon-jet difference in ϕ

In a leading-order calculation of a parton scattering process, there are only two particles in the initial state and two in the final state, as in Fig. 2.1. Higher order calculations include Feynman diagrams in which there are additional vertices, and may be more than two final state particles. The theoretical calculation of the process $Q^* \rightarrow q\gamma$ is leading order, so by momentum conservation, the photon and jet are back to back in the phi coordinate. To reduce background from events with higher jet multiplicity (number of final state jets), a cut is made on $\Delta\phi = \phi_\gamma - \phi_{jet}$, requiring it to be in the range $(\pi - 0.4) < \Delta\phi < (\pi + 0.4)$ **(13)**. This cut is not applied to the photon-jet data sample which is compared with the QCD prediction for the inclusive cross section, as this calculation is not leading order.

The analysis cut quantities with efficiencies for photon events are listed in Table 5.1. The errors listed are statistical. Some of the cut efficiencies were determined from collider data events, and these are so indicated. Other cut efficiencies are estimated from Monte Carlo. To estimate the dependence of these cut efficiencies on photon E_T, single particle photon events were simulated at 40 and 80 GeV/c. The

	Cuts	Efficiencies (%)			Data Sample
		40 GeV	80 GeV	other	
(1)	$\eta_\gamma^{detector}\| < 0.9$			91 ± 2	Collider data
(2)	$\|Z_{vertex}\| < 50$ cm			90 ± 1	Collider data
(4)	$0.05 < EMF_j < 0.95$	99.8 ± 0.1	99.6 ± 0.2		Collider data
(5)	$E_T iso < 2\ GeV$	99.8 ± 0.1	99.8 ± 0.1		MC single γ
(6)	$EMF_\gamma > 0.90$	99.9 ± 0.1	99.8 ± 0.1		MC single γ
(7)	$SPREAD < 0.70$	99.4 ± 0.1	99.4 ± 0.1		MC single γ
(8)	Hmatrix χ^2	98.6 ± 0.1	98.4 ± 0.1		MC single γ
(10)	$\frac{E_{maxcell}}{E_{cluster}} < 0.75$	99.9 ± 0.1	98.6 ± 0.1		MC single γ
(11)	$\frac{MET}{E_{T_\gamma}} < 0.5$			97 ± 1	MC $Q^* \rightarrow Q\gamma$
(12)	$2.74 < \Delta\phi < 3.54$			$(79 + .022M) \pm 2$	MC $Q^* \rightarrow Q\gamma$
total		$(61 + 0.017M) \pm 4$	$(60 + 0.017M) \pm 4$		

Table 5.1: Offline analysis cuts with the pass efficiencies for photon events. The last column gives the data source used to estimate the efficiency. The efficiencies for each cut are for a data sample where all previous cuts were also applied. The total efficiencies of all cuts are given in the last row.

event distributions in these cut quantites are shown in Figures 5.1 and 5.2. The acceptance and the efficiency for the standard photon cuts as a function of photon E_T for photons in the central calorimeter are shown in Fig. 5.3. These data points were determined in Monte Carlo simulations of photons and π° mesons. Acceptance is relatively flat with photon E_T, while the total cut efficiency falls off sharply below about 20 GeV.

5.6 Scattering Angle in the Center of Momentum System (θ^*)

In searches for particle decay, a lower-limit cut may be imposed on $\cos\theta^*$, where θ^* is the angle between the photon and the beam of colliding hadrons (on the side the photon is nearest to the beam) in the photon-jet center of momentum system

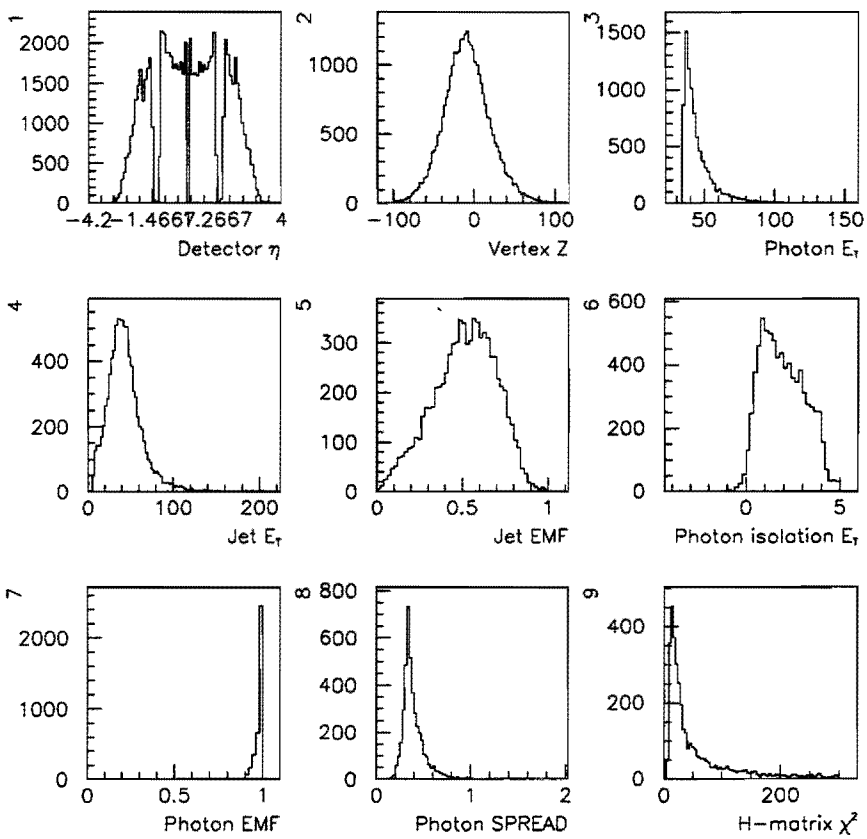

Figure 5.1: The event distributions in the variables used in analysis cuts 1-9.

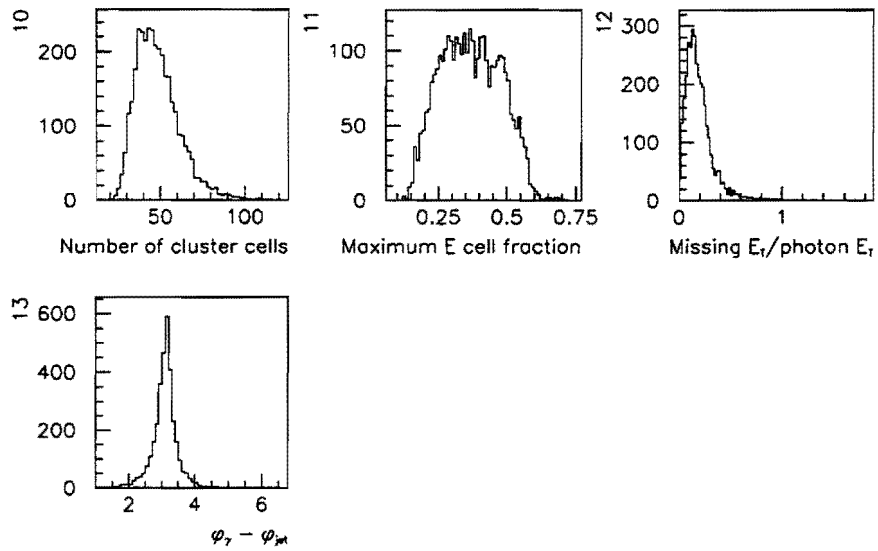

Figure 5.2: The event distributions in the variables used in analysis cuts 10-13.

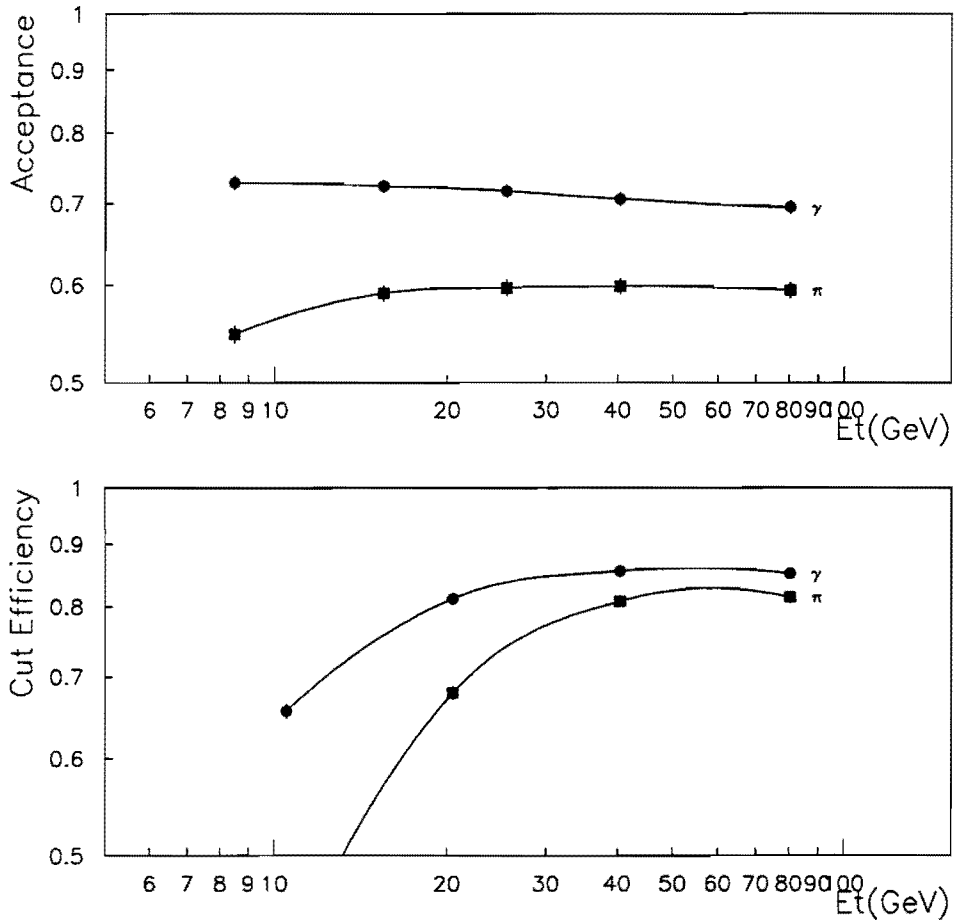

Figure 5.3: The acceptance and offline analysis cut efficiencies, as determined from (mixture) Monte Carlo simulations.

(CMS) reference frame. For a spin-1/2 excited quark decaying to a ground state quark plus a photon, the decay process is isotropic in the rest frame of the excited quark, so its angular distribution is flat in $\cos\theta^*$. The background has an angular distribution proportional to $1/(1-\cos\theta^*)^n$, where n is of order 1-2.

I attempt to select an optimized cut value in $\cos\theta^*$. Figure 5.4 shows the photon angular distribution of the experimental data sample collected with the highest energy photon trigger, and also of Monte Carlo generated Q^* events at masses of 100 and 400 GeV. The plots on the left are without offline analysis cuts, showing that the experimental data, which is primarily QCD background, rises with $\cos\theta^*$ while the distribution of Q^* events is flat. The plots on the right side of the figure show that after analysis cuts are applied, both background and signal event distributions fall off at high $\cos\theta^*$.

An optimum cut value gives the largest signal/background ratio. I expect that signal/background is small, so the optimum cut value will be found by maximizing the ratio $R = \epsilon_{Q^*}/\epsilon_{Q^*+background}$, where ϵ_{Q^*} and $\epsilon_{Q^*+background}$ are the efficiencies with which data pass a cut in $\cos\theta^*$ for Monte Carlo simulated Q^* events and for experimental data, respectively. These efficiencies are shown as a function of the upper limit cut value of $\cos\theta^*$ in Fig. 5.5(*left*).

The value of R is shown for $M^* = 100$ and 400 GeV/c^2 in Fig. 5.5(*right*). It is seen that for $M^* = 100\ GeV/c^2$, signal/background may be improved only marginally by imposing a $\cos\theta^*$ cut. At $M^* = 400$ GeV there is no advantage to a cut. Previously imposed analysis cuts have softened the $\cos\theta^*$ dependance, as was seen in Fig. 5.4. It is seen in Fig. 5.6 that after cuts 2,3, and 4 the $\cos\theta^*$ distribution has flattened considerably. For this analysis, there is no advantage to imposing an upper limit cut on the variable $\cos\theta^*$.

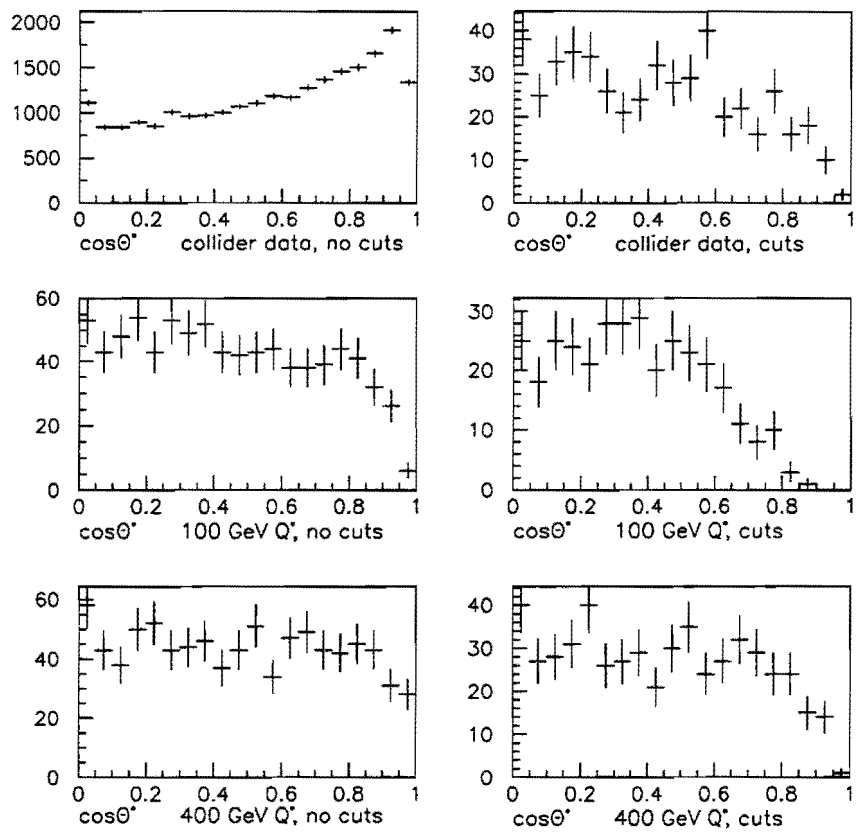

Figure 5.4: The event distribution in $\cos\theta^*$ for experimental data *top left:* without offline analysis cuts, and *top right:* with offline analysis cuts. Monte Carlo Q^* events at $M^* = 200\ GeV/c^2$ *middle left:* without offline analysis cuts, and *middle right:* with offline analysis cuts. Monte Carlo Q^* events at $M^* = 400\ GeV/c^2$ *bottom left:* without offline analysis cuts, and *bottom right:* with offline analysis cuts.

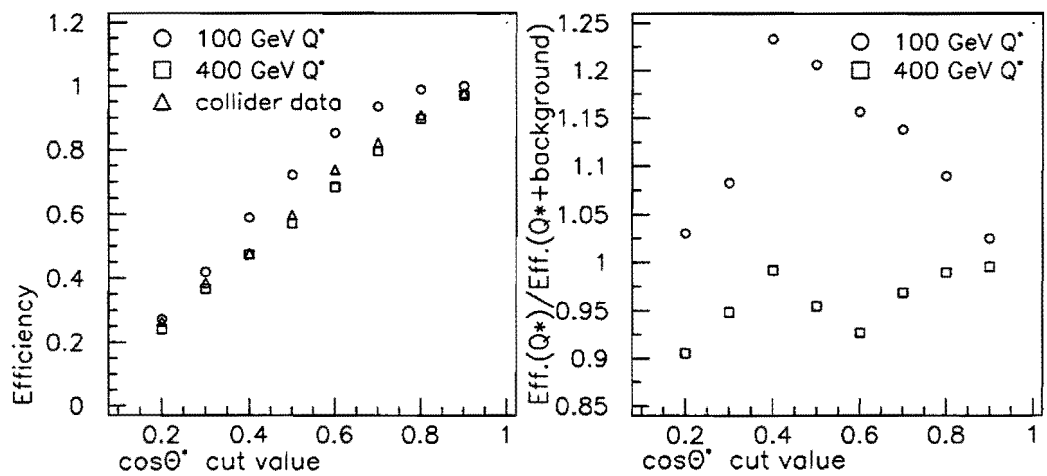

Figure 5.5: ***left:*** **Photon event efficiencies as a function of the upper limit cutoff on $\cos\theta^*$ for experimental data and for Q^* Monte Carlo samples.** ***right:*** **The ratio $R = \epsilon_{Q^*}/\epsilon_{Q^*+background}$ for Monte Carlo Q^* events at $M^* = 100$ and 400 GeV/c^2.**

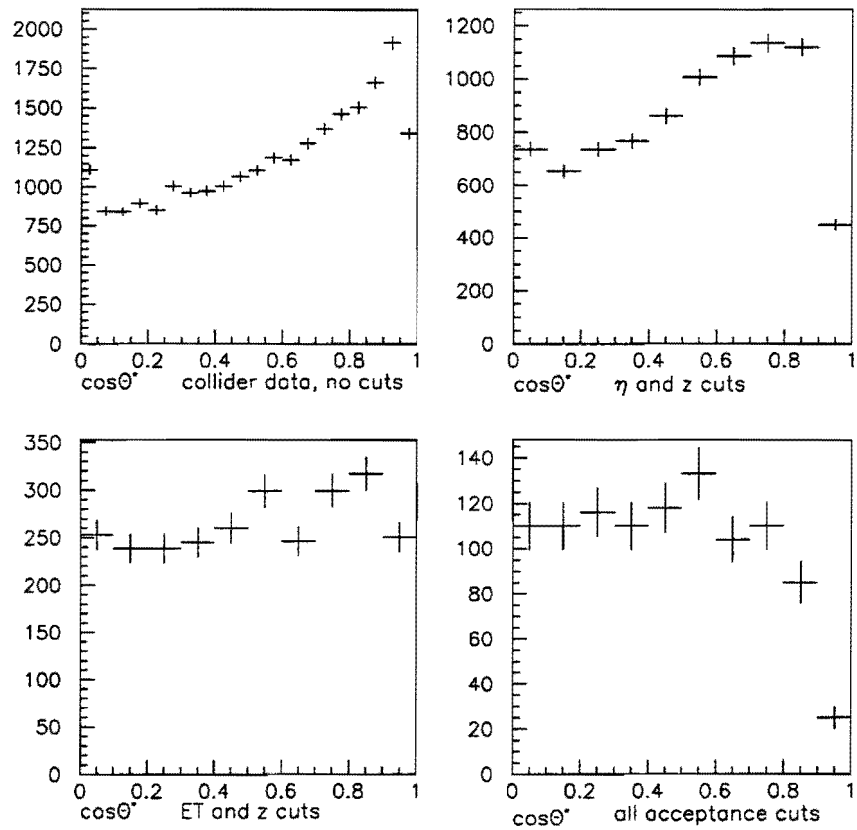

Figure 5.6: Event distribution of experimental data sample in $\cos\theta^*$ *top left:* with no offline analysis cuts applied, *top right:* with analysis cuts 1 and 2 (see table 5.1), *bottom left:* with analysis cuts 2,3, and 4, and *bottom right:* with analysis cuts 1-13.

5.7 The Photon Purity

After all attempts to reduce background have been exhausted, the signal to background ratio is still of order 1:1. The purity of the sample must be determined. For this process, a discriminant is chosen which favors photon events over background. The discriminant separates the experimental data sample into two subsets; those events which pass the condition and those which fail. The fraction of events which pass is denoted ϵ, and the fraction of failed events is $1-\epsilon$. The efficiencies with which signal ϵ_γ and background ϵ_π events pass the discriminant are determined via Monte Carlo simulation. The efficiency ϵ with which collider data passes the discriminant lies somewhere between ϵ_γ and ϵ_π. The photon purity is denoted γ, and is related to the pass efficiencies by:

$$\begin{pmatrix} 1-\epsilon \\ \epsilon \end{pmatrix} = \begin{pmatrix} 1-\epsilon_\gamma & 1-\epsilon_\pi \\ \epsilon_\gamma & \epsilon_\pi \end{pmatrix} \times \begin{pmatrix} \gamma \\ 1-\gamma \end{pmatrix}, \tag{5.4}$$

which is solved for γ as,

$$\gamma = \frac{\epsilon_\pi - \epsilon}{\epsilon_\pi - \epsilon_\gamma}. \tag{5.5}$$

False prompt photon events from π° decays consist of two almost collinear photons, and it is about twice as likely for a conversion to occur as they traverse a given amount of detector material as in a real photon event. In one method for measuring the photon purity, the ionization energy of converted events is measured in the CDC. The discriminant is whether an associated charged track is reconstructed in the tracking chamber that points to an electromagnetic shower. The track must have an energy distribution consistent with the passing of two minimum ionizing particles. A similar method measures the fraction of shower energy in the first layer of the calorimeter, identifying non-conversions. Background events are more likely than photons to convert in this layer, depositing some of their energy. A third method cuts on the transverse energy distribution of the photon shower, using

the variable SPREAD described in Section 5.4. At low energies, the finite angular separation of photon pairs in π° decay causes these electromagnetic showers to be broader than signal events of the same energy. The photon purity is measured at several energies using the first two methods described above, and a parameterized purity function is fit to the data points. The function which was found to fit the purity measurements with the lowest χ^2 is given by:

$$\gamma(E_T) = 1 - e^{-aE_T}, \tag{5.6}$$

with the parameter value $a = 0.009 \pm 0.002$. The function and purity data points are shown in Fig. 5.7

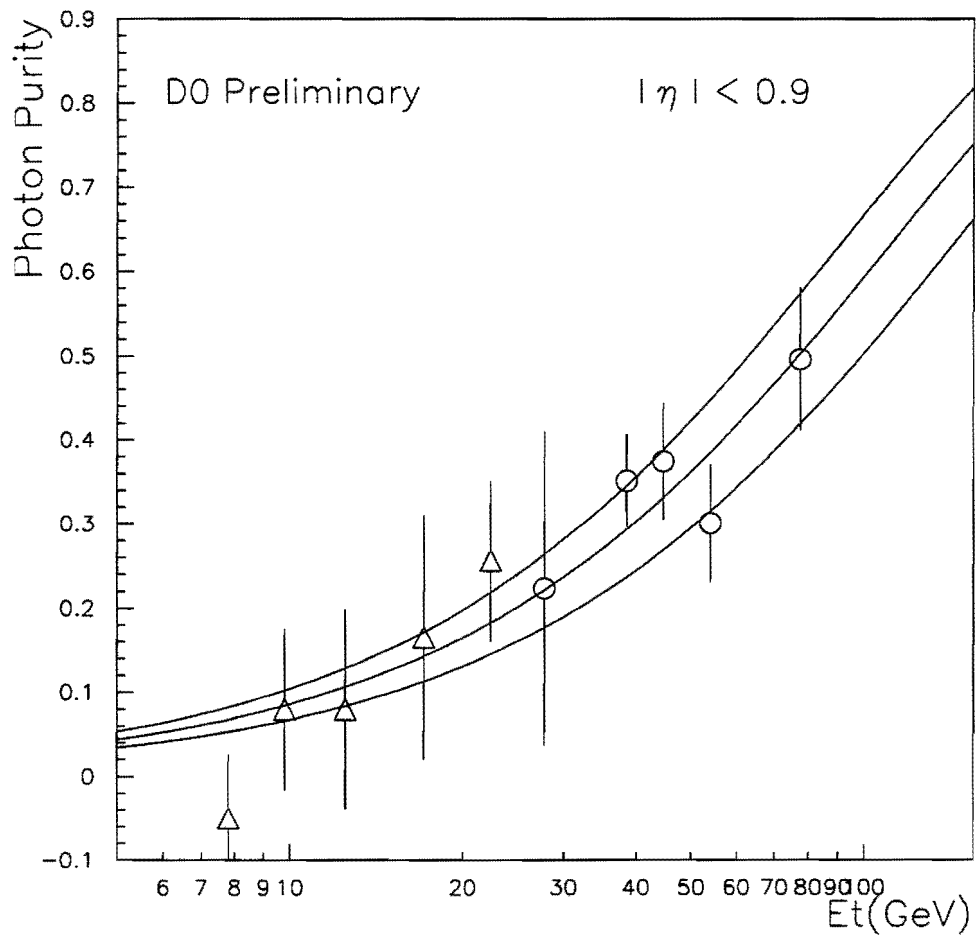

Figure 5.7: The photon purity γ vs. the photon E_T.

CHAPTER 6
PROMPT PHOTON ANALYSES AT DØ

6.1 Introduction

This chapter reviews the progress and results of ongoing prompt photon analyses in the DØ experiment. The cross section vs. photon P_T and the photon angular distribution represent the data sample described in Chapter 5 without analysis cuts 3,4,5,8, and 13, with a minimum electromagnetic energy fraction of 0.95 in cut 7, and with a maximum H-matrix χ^2 value of 100 in cut 9. The photon purity measurement described in Section 5.7 is applied in the first two measurements. The DØ Prompt Photon group currently includes W. Chen, S. Fahey, N. Graf, S. Jerger, S. Linn, Y. Lui, B. Pope, P. Rubinov, C. Shaffer, G. Snow, F. Wen, and J. Womersley.

6.2 Inclusive Cross Section

The prompt photon inclusive cross section is shown in Fig. 6.1, (analysis by S. Fahey [79]) with a next-to-leading logarithm (NLL) calculation by J. Owens *et al.* using CTEQ2M parton distribution functions at a scale $\mu = E_T$ [78]. The Monte Carlo program which provides the QCD prediction does not include jet fragmentation or hadronization. Instead, the momenta of final state partons are smeared with resolution functions appropriate for the DØ detector. The NLL prediction is consistent with our data over the full range of the measurement, as seen in Fig. 6.2.

Figure 6.3 displays the inclusive cross section as a function of the invariant mass of the photon and leading jet. The scale dependence of the NLL prediction and the leading-logarithm (LL) prediction are included in Fig. 6.4.

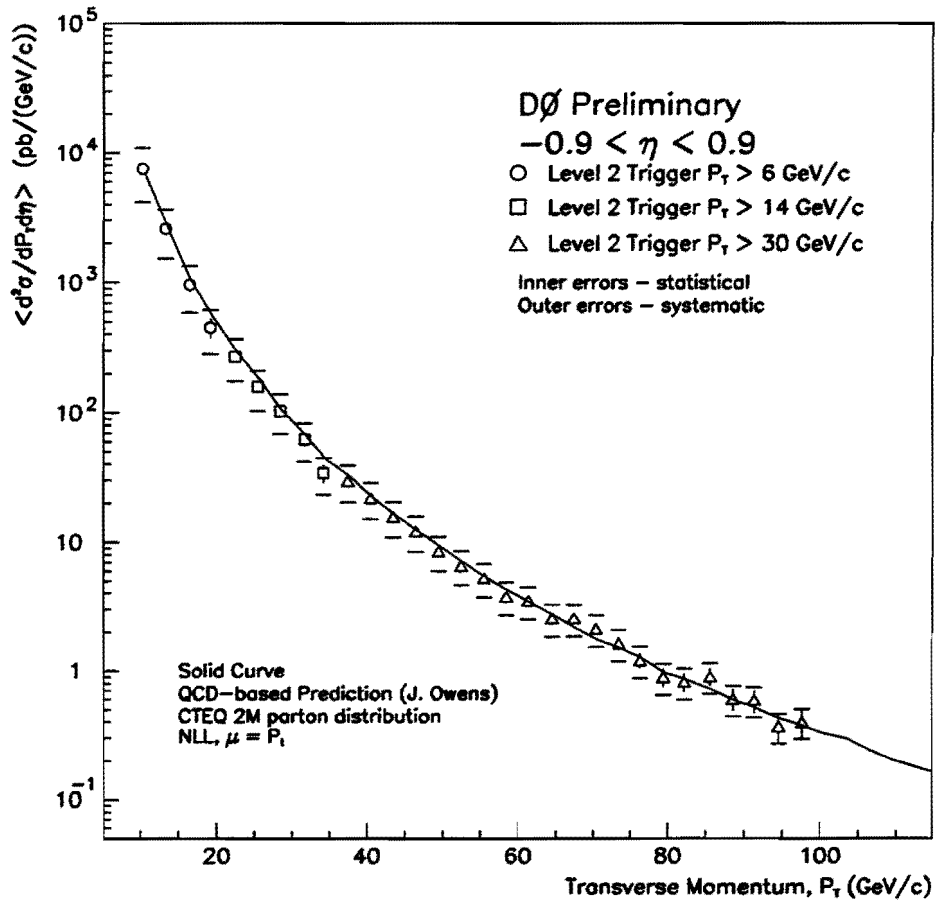

Figure 6.1: Inclusive prompt photon cross section. The vertical error bars are statistical and the horizontal error bars are systematic. Parton distribution functions are CTEQ2M and renormalization scale is $\mu = p_T$ of the photon.

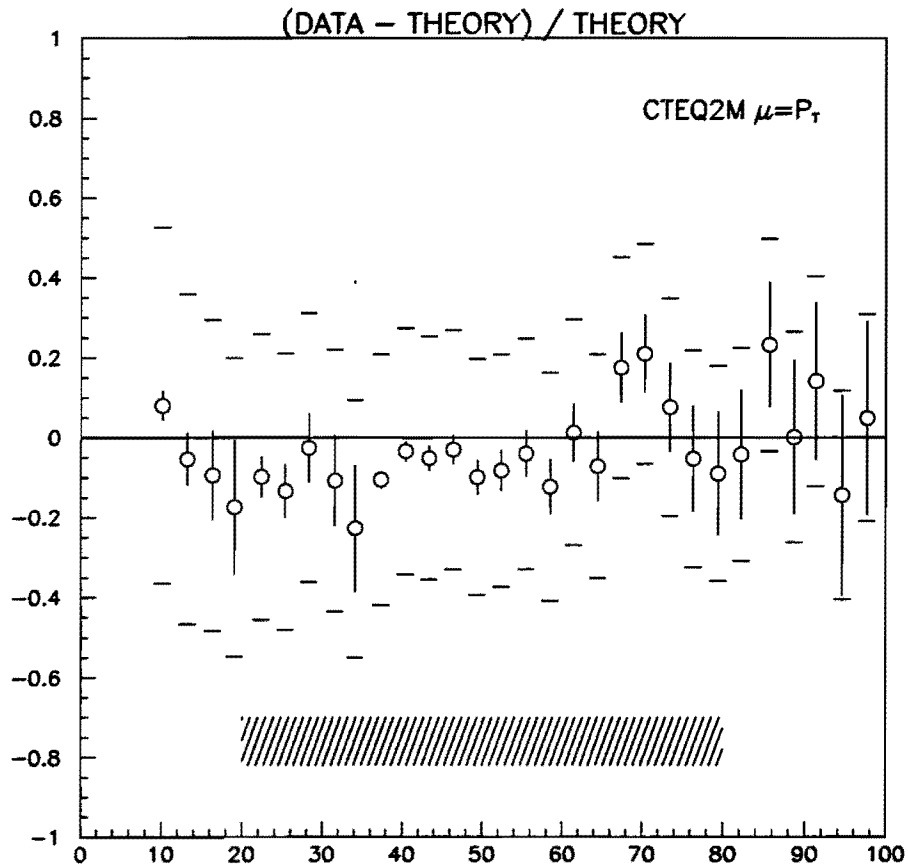

Figure 6.2: (Data-Theory)/Theory for the cross section $\frac{d\sigma}{dp_T d\eta}$ shown in figure 6.1. Band at bottom shows systematic error in luminosity calculation.

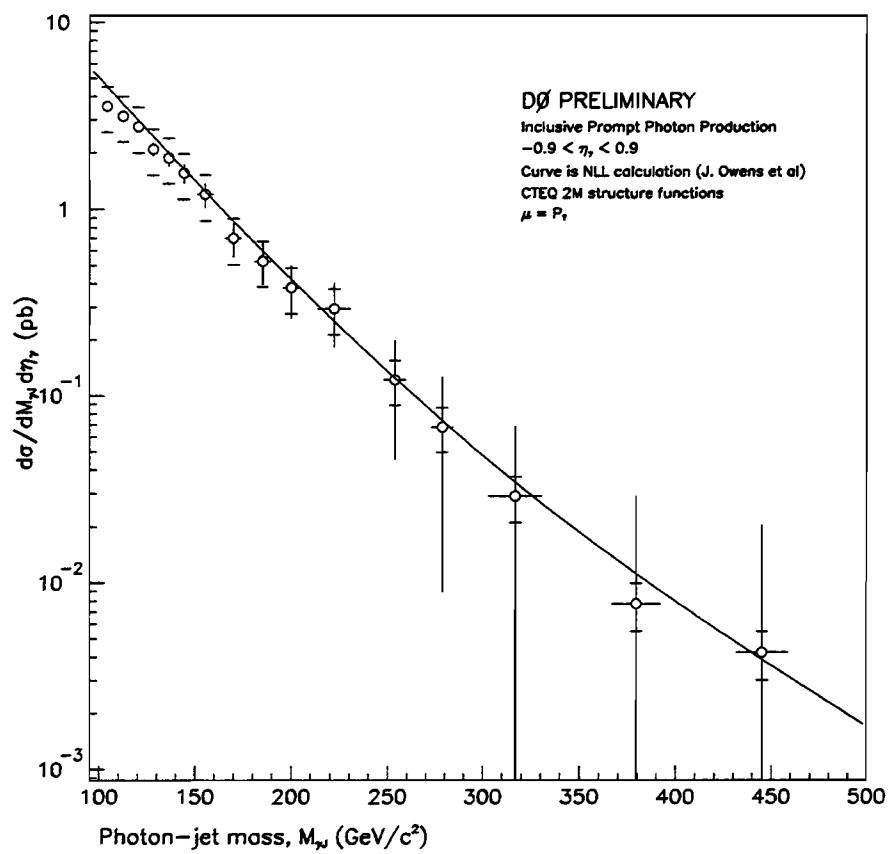

Figure 6.3: The prompt photon inclusive cross section as a function of the photon-jet invariant mass.

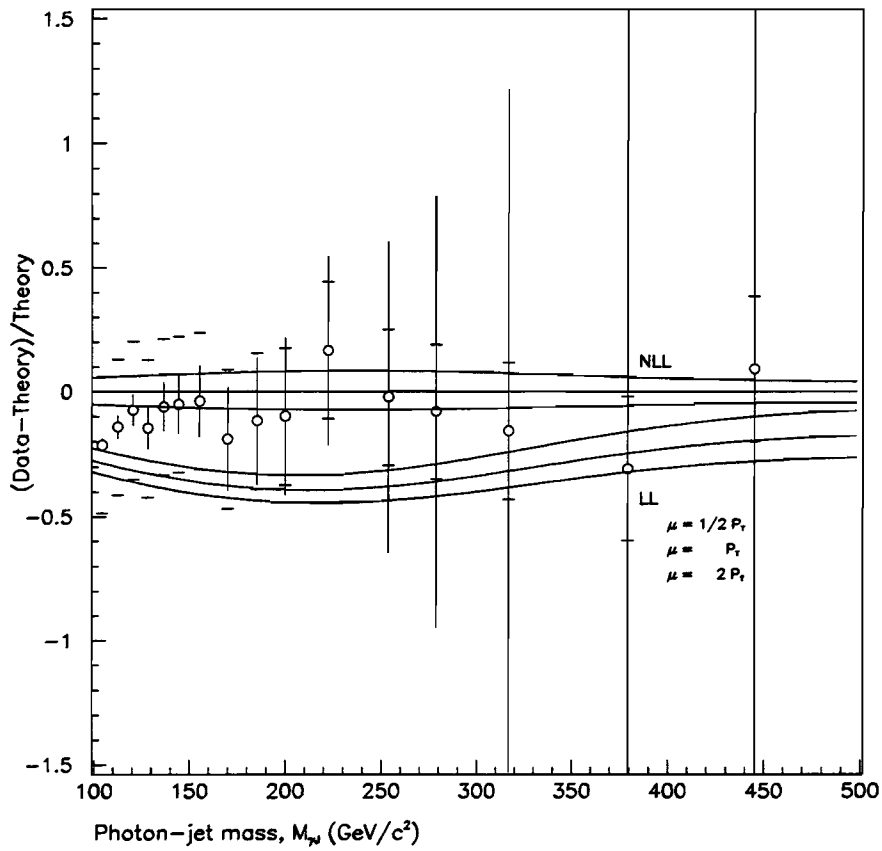

Figure 6.4: (Data-Theory)/Theory for the prompt photon inclusive cross section $\frac{d\sigma}{dM d\eta}$ shown in figure 6.3.

6.3 Angular Distribution

The dominant QCD jet processes are mediated by the exchange of a spin 1 gluon; prompt photons, however, are produced through the exchange of a spin 1/2 quark. The angular distributions for the two run approximately as $dN/d\cos\theta^* \propto 1/(1-\cos\theta^*)^n$, where θ^* is the scattering angle between the photon and the beams of colliding hadrons (on the side the photon is nearest to the beam) in the reference frame of the center of momentum (CMS) of the final state photon-jet system, with $n > 2$ for jets and n of order 1 for prompt photons [81].

The angular distribution of prompt photon events provides a sensitive measurement of matrix elements that is decoupled from the effects of parton distributions. Care must be taken to properly account for the angular dependence of the photon purity. Let η_γ and η_{jet} be the pseudorapidity of the photon and leading jet. I define,

$$\eta_{boost} = \frac{\eta_\gamma + \eta_{jet}}{2}, \tag{6.1}$$

the pseudorapidity of the center of momentum of the photon-jet system in the lab frame, and

$$\eta^* = \frac{\eta_\gamma - \eta_{jet}}{2}, \tag{6.2}$$

the pseudorapidity of the photon with respect to the colliding hadron beams in the photon-jet CMS frame (parton k_T is neglected). Photon candidates are selected from regions of uniform acceptance in η^* $vs.$ η_{boost}, in the range $30 < p^* < 120$ GeV/c, where p^* is the photon momentum in the CMS frame. In order to extend the measurement over as large a range of $\cos\theta^*$ as possible and to avoid the use of acceptance corrections, the region of full acceptance in the coordinates η_γ $vs.$ η_{jet} is divided into overlapping boxes in eta^* vs. η_{boost} of size 0.8×0.8, as shown in Fig. 6.5. The event distributions of the boxed regions are normalized to one another by the ratio of the total number of events in the ranges of overlap in η^*. In events where there is more than one jet present, the momentum vectors of jets in the hemisphere

opposite the photon in the ϕ coordinate are added together to preserve the simple two body to two body geometry

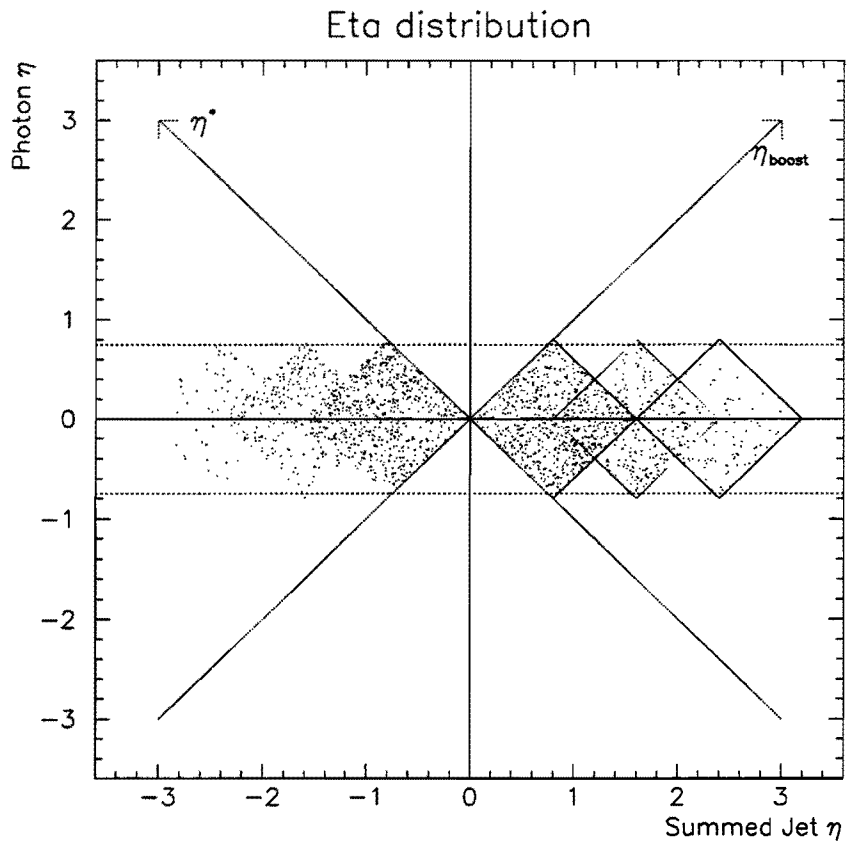

Figure 6.5: Photon candidate events in η_γ vs η_{jet} for the three regions of uniform acceptance in η^* vs. η_{boost}. The lines at 45° are the η^* and η_{boost} axes.

The photon purity $\gamma(\cos\theta^*)$ is determined in the lowest η^* box to be about 0.52. Statistical limitations prevent an accurate photon purity measurment in the next two η^* regions, so a form of extrapolation from the first region is used. It is assumed that the angular distribution of the background will be the same as that of the DØ inclusive jet data sample (the only factor distinguishing the two

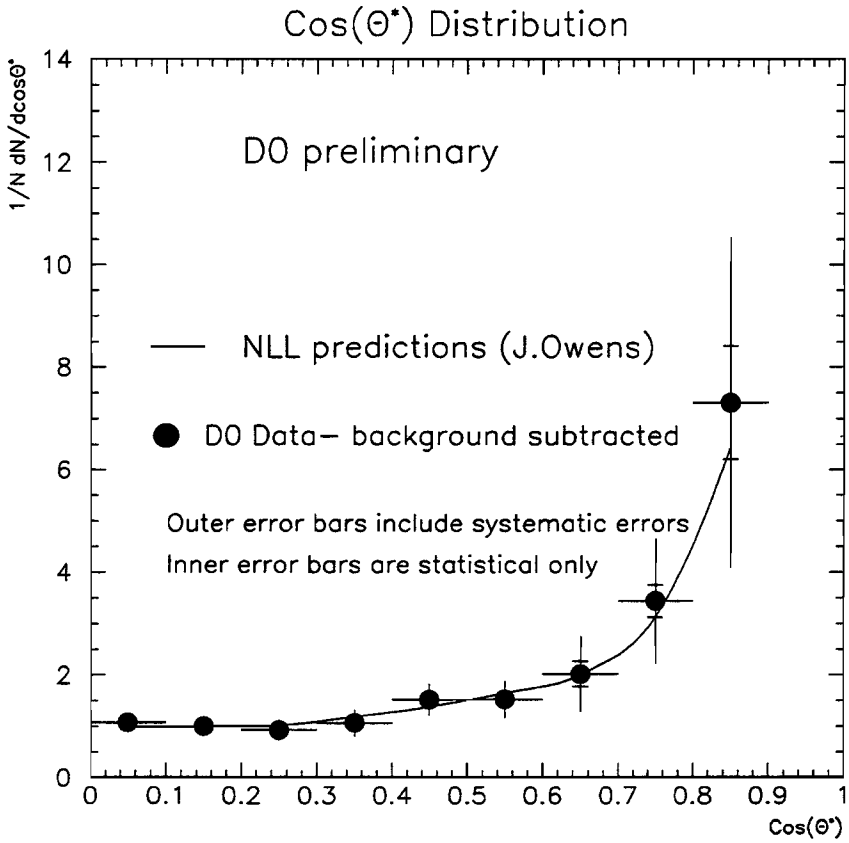

Figure 6.6: The normalized $\cos\theta^*$ distribution. The curve is a spline fit to a NLL theory Monte Carlo calculation.

is fragmentation). The angular distribution of multijet events is measured, with one jet in each event randomly assigned to be a photon. The distribution of the background as a function of $\cos\theta^*$ in the first η^* region is given by:

$$\frac{dN_{back}}{d\cos\theta^*} = (1 - \gamma(\cos\theta^*))\frac{dN_{total}}{d\cos\theta^*} \tag{6.3}$$

where N_{back} is the number of background events, N_{total} is the number of signal plus background events, and the photon purity γ as a function of $\cos\theta^*$ is given by:

$$\gamma(\cos\theta^*) = 1 - (\frac{dN_{back}}{d\cos\theta^*}/\frac{dN_{total}}{d\cos\theta^*}). \tag{6.4}$$

To compare the (background corrected) angular distribution directly with the theory prediction, both are normalized to one in the first three 0.1 bins in $\cos\theta^*$. Agreement of the theory prediction with data is good, as seen in Fig. 6.6 (analysis by P. Rubinov [80]).

CHAPTER 7
MASS FITTING ANALYSIS

7.1 Introduction

The appearance of an excited quark decay contribution to the photon-jet inclusive cross section will reveal itselve as a resonance peak in the photon-jet invariant mass distribution, centered at the excited quark mass. The goal of this part of the analysis is to look for evidence of such a resonance and to determine the statistical significance of the evidence.

7.2 The Invariant Mass Distribution

The $Q^* \rightarrow \gamma q$ process has only a photon and ground state quark in the final state, at leading order perturbation theory. In the Q^* rest frame,

$$M = E_\gamma + E_q = 2E_\gamma = 2E_{T_\gamma}/\sin\theta^* = 2E_{T_\gamma}\cosh\eta^*, \tag{7.1}$$

where E_γ and E_q are the photon and quark energies in this frame and where

$$\eta^* = \frac{(\eta_\gamma - \eta_{jet})}{2} \tag{7.2}$$

is the pseudorapidity of the photon with respect to the colliding hadron beams on the nearest side (parton k_T is neglected). The quantities η_γ and η_{jet} are measured in the laboratory reference frame, but η^* is frame independent. To avoid the error associated with jet energy resolution, $E_{jet} \approx E_q$ is not used in the expression for the mass. Higher order Feynman diagrams may include more final state jets, and for

these events (7.1) is not appropriate. In this analysis only leading order diagrams are considered, so the photon E_T and photon-jet opening angle is sufficient information to define the mass unambiguously. Soft gluon radiation smears the jet position, which degrades the mass resolution. This effect is accounted for in the Monte Carlo simulation of signal events. The Q^* rest frame is assumed to have very little E_T with respect to the lab frame. The photon-jet invariant mass distribution for the experimental data sample (with all analysis cuts applied) is shown in Fig. 7.1.

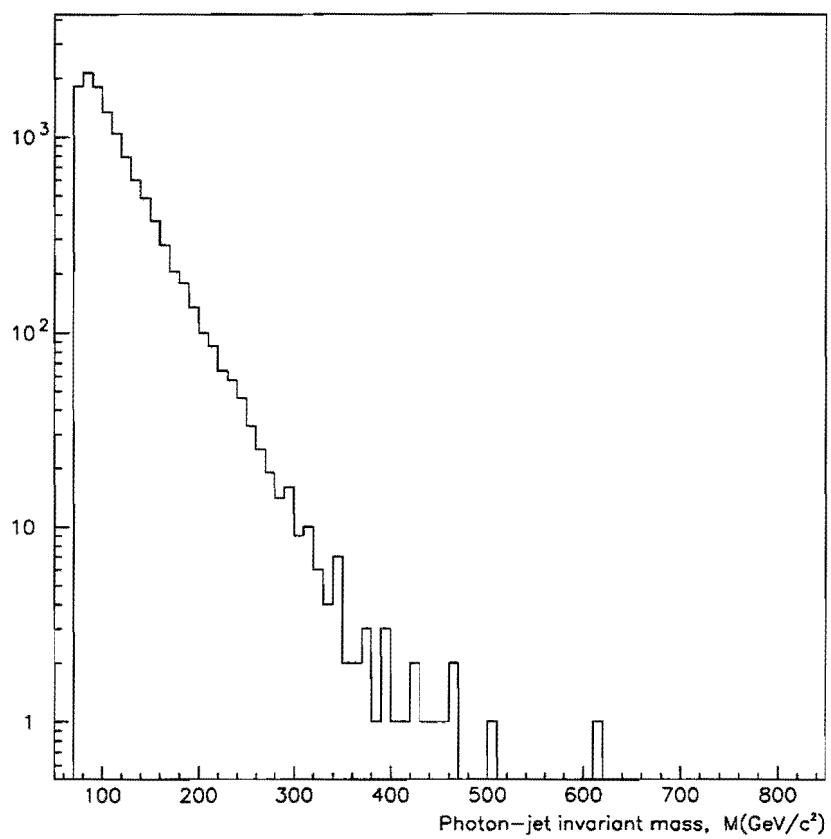

Figure 7.1: The photon-jet invariant mass distribution $M(GeV/c^2)$.

The error on the photon-jet invariant mass of (7.1) is given by:

$$\Delta M = \sqrt{(\frac{\partial M}{\partial E_{T_\gamma}}\delta E_{T_\gamma})^2 + (\frac{\partial M}{\partial \eta^*}\delta\eta^*)^2} = \sqrt{(2\cosh\eta^*\delta E_{T_\gamma})^2 + (2E_{T_\gamma}\sinh\eta^*\delta\eta^*)^2}, \tag{7.3}$$

where it is assumed that the photon energy resolution and the photon and jet position resolution are uncorrelated. The resolution of the detector is discussed in Section 4.4. The error on the photon-jet invariant mass ΔM is calculated from the reconstructed four-vectors of photon-jet pairs in samples of fully simulated Monte Carlo events. From GEANT, the four-vector of a photon or jet is the vector sum of all particles in its shower. This quantity is compared to the four-vector which is reconstructed from detector information. I assume that $\Delta M(M|M^*)$ follows a normal distribution, so I fit to a gaussian function to estimate the mean and standard deviation. The distributions are shown in Fig. 7.2. The photon-jet mass resolution ($\sigma_M = \Delta M/M$) is shown in Fig. 7.3 with a fit to a polynomial function. The uncertainty introduced by the resolution of the detector is incorporated in the full detector simulation of the Monte Carlo events.

7.3 Efficiency vs. Invariant Mass

The thresholds which I must impose on the energy of the photon and jet, to avoid trigger turn-on (Sec. 4.3), cause a region of turn-on in the invariant mass distribution. I estimate the region of turn-on with a simple Monte Carlo study. A Monte Carlo program by J. Owens *et al.*[78] is used to calculate the prompt photon cross section, as discussed in Section 6.2. I generate the leading order cross section with a minimum photon E_T of 35 GeV and leading jet E_T of 20 GeV, as is imposed on the experimental data sample. I generate the cross section again with E_T thresholds of 5 GeV for both the photon and leading jet. As can be seen in Fig. 7.4, the

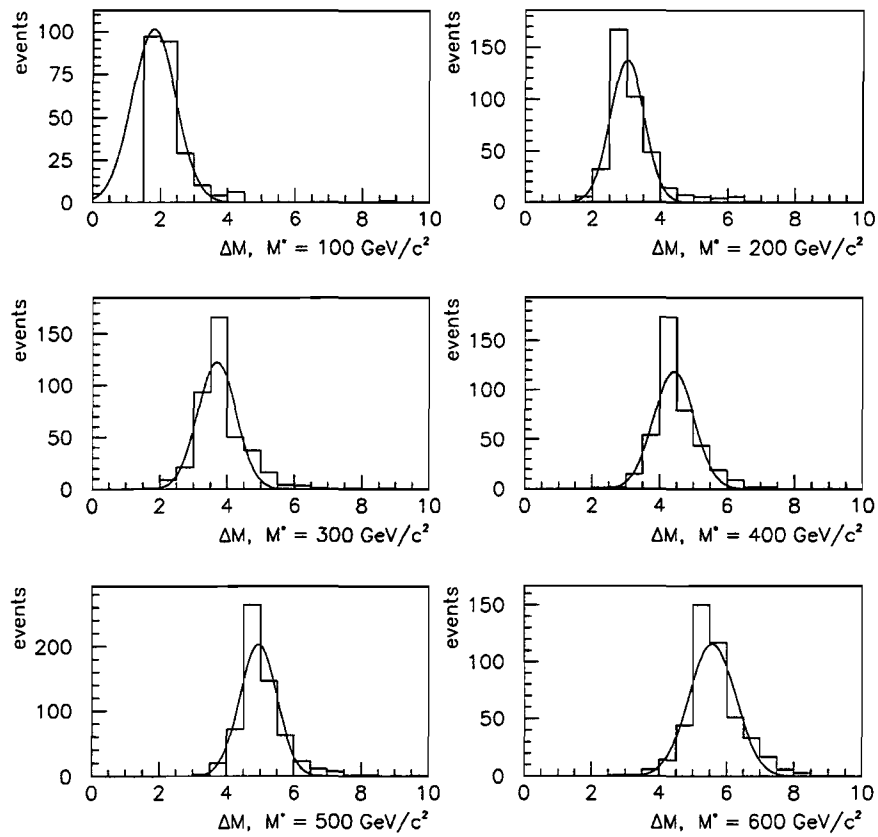

Figure 7.2: The error on the photon-jet mass ΔM associated with the energy and position resolution of the DØ detector. The curve is a polynomial fit to the data points, weighted by their errors.

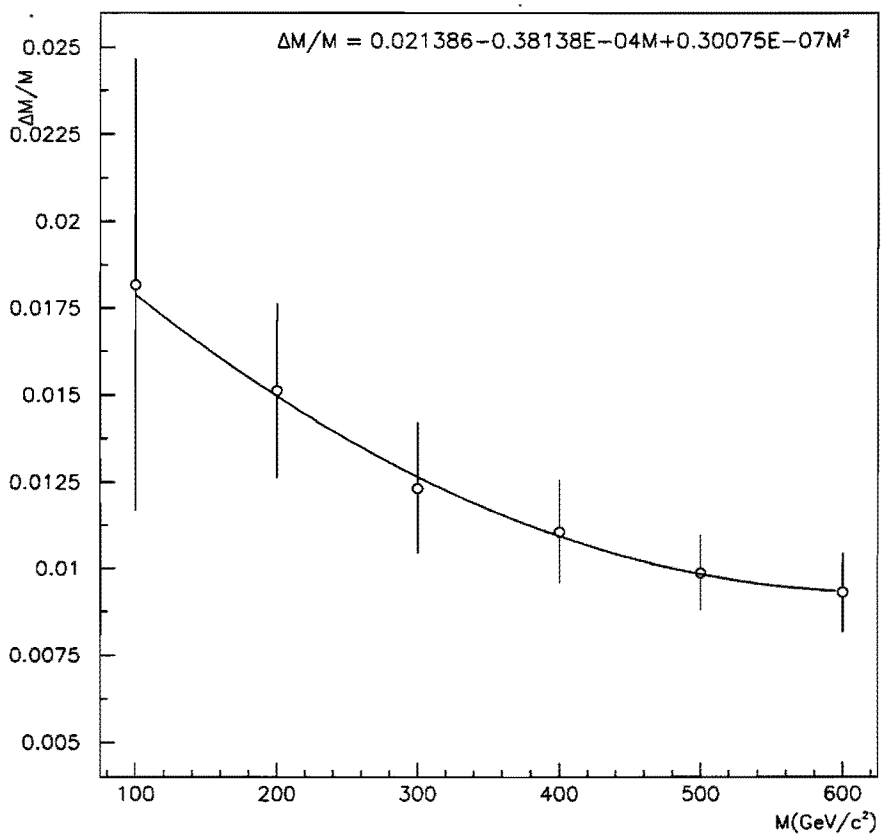

Figure 7.3: The photon-jet mass resolution, $\sigma_M = \Delta M/M$, where ΔM is given by equation (7.3).

two cross sections converge above an invariant mass of about 200 GeV/c^2. Photon events which do not satisfy the E_T threshold requirements contribute to the inclusive invariant mass cross section at masses below 200 GeV/c^2, but are dropped by the trigger and offline analysis cuts.

I interpret the ratio of the cross section with higher E_T thresholds over that with the low thresholds as the mass turn-on for my data sample, which I will call $\epsilon_M(M)$.

7.4 Fitting Procedure

I apply a fitting procedure to the mass distribution of the data sample described in section 7.2 to determine the number of Q^* candidate events. The cross section derived from the number of events is compared to theoretical predictions to determine if a significant signal has been observed.

The strategy of the search is here summarized:

1. Simulate Monte Carlo data samples of the process $Q^* \rightarrow \gamma q$ at different Q^* masses, M^*.

2. Choose function, $S(M|M^*)$, which fits signal mass distribution of Monte Carlo data samples.

3. Choose function, $B(M)$, which fits the experimental mass distribution, assumed to contain mostly background.

4. Simulate artificial background data sample consistent with form of $B(M)$.

5. Add Monte Carlo data sample with known number of events $N(M^*)$ to the artificial background. Fit combined data sample with

$$F(M|M^*, N) = B(M) + N(M^*)\ S(M|M^*).$$

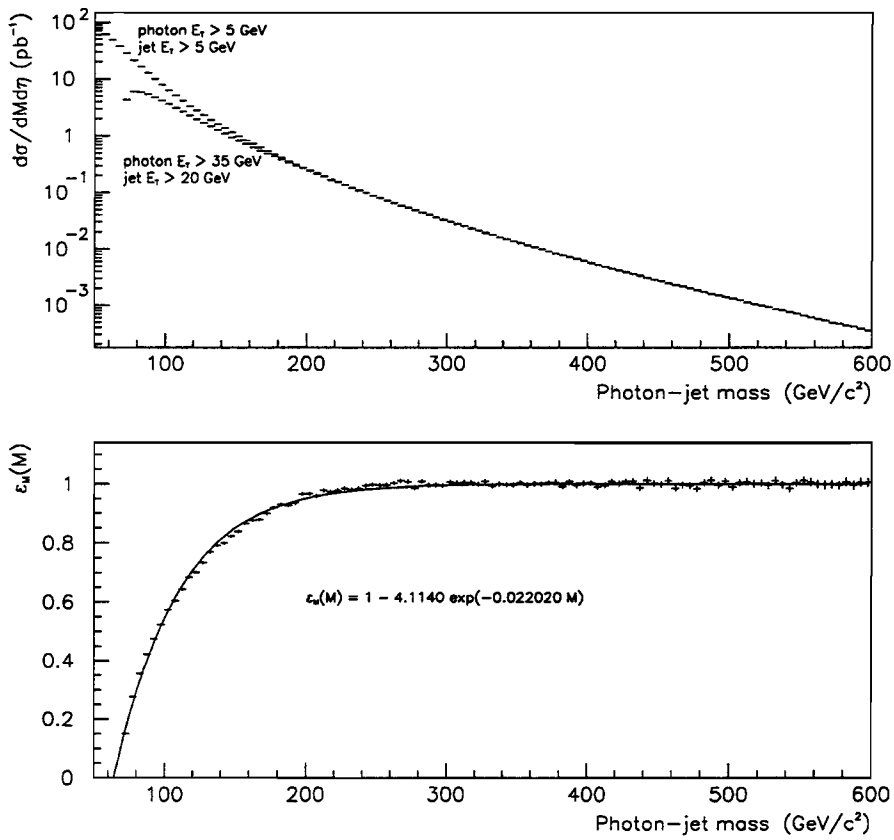

Figure 7.4: *top*: Monte Carlo direct photons with the requirement that the photon and jet $E_T > 5\ GeV$ compared with the same sample with the requirement that the photon $E_T > 35\ GeV$ and jet $E_T > 20\ GeV$. *bottom*: The photon-jet mass turn-on curve. This is the ratio of the two cross sections shown in the top part of the figure.

$N(M^*)$ is fixed, and the parameters in $B(M)$ and $S(M|M^*)$ are allowed to vary in the fit. Repeat for each Monte Carlo sample.

6. The fits yield a value of each parameter in $S(M|M^*)$ at several discrete M^* values. Fit the parameter values with polynomial functions of M^* to interpolate between them. $S(M|M^*)$ is a function defined at any value of M and M^*.

7. Fit the experimental mass distribution with $F(M|M^*)$. The number of signal events $N(M^*)$ and the parameters in $B(M)$ are allowed to vary in the fit. $\hat{N}(M^*)$ is best value of the number of signal events found at M^*.

7.5 Fitting Method

I devise a function $F(M|M^*)$, describing a mass distribution which is a sum of signal and background parts. The parameterization of the signal part of the function is determined by Monte Carlo studies of the Q^* theoretical model [11],[12] [13],[14]. Background to the excited quark signal originates primarily from direct photon production and dijet processes which mimic photon events, as discussed at the beginning of Chapter 5. I don't need to know the composition of the background if I may assume that the differential cross section of background ($\frac{d\sigma_{QCD}}{dM}$) is monotonically decreasing with increasing mass. The mass distribution of background events can then be fit well with an appropriate locally monotonic function (monotonic over the range of the data). An additional contribution to the mass distribution from the decay of excited quarks would appear as a resonance peak in the steeply falling mass spectrum.

The combined function which is fit to the data is expressed as:

$$F(M) = B(M|P_1, P_2, ...) + N(M^*)\ S(M|A_1(M^*), A_2(M^*), ...) \tag{7.4}$$

$B(M)$ is the background mass distribution, which is a function of the photon-jet mass M, and is parameterized by variables P_i. $S(M)$ is the signal mass distribution, which is a function of M, and is parameterized by variables A_i, which are functions of the excited quark mass M^*. The integral of $S(M)$ over all M is equal to one. $N(M^*)$ is a normalization factor, which is allowed to vary in the fit.

For any given M^*, the variable parameters in $F(M|M^*)$ are determined by minimizing a χ^2 [85],[86], given by:

$$\chi^2 = \sum_{i=1}^{n} (\frac{F(M_i) - y_i}{\sigma_i})^2 \tag{7.5}$$

I divide the mass distribution into n bins of width 10 GeV/c^2. The bin weights (y_i) are the event density, equal to $10 \times \frac{dN}{dM}$ events per GeV/c^2 at the average mass value integrated over the range of the bin, $M_i = \frac{\int dM\ M\ B(M)}{\int dM\ B(M)}$. For most bins, y_i is just n_i, the number of events in the bin. The mean value and standard deviation of the population distribution for each bin is unknown. The best estimates are $\mu_i \approx n_i$ and $\sigma_i \approx \sqrt{n_i}$, which are most accurate when the number of events per bin is large, and the probability distribution for y_i is normal. When the number of events per bin is small, the probability distribution is Poisson, and this approximation becomes unsatisfactory. Therefore, in χ^2 fits with discrete data, bins should be combined which contain ≈ 5 or fewer events. In this analysis, I merge bins such that each datum represents at least 8 events [87]. The weight and error of a merged bin are given by $y_i = n_{merged}/n_{bins}$ and $\sigma_i = (\sqrt{n_{merged}}/n_{bins})$, where n_{merged} is the total number of events in the merged bin, and n_{bins} is the number of 10 GeV bins which have been combined.

The parameters in the function $F(M|M^*)$ are varied until the minimum value of χ^2 is found. At the minimum value of χ^2, agreement between $F(M|M^*)$ and the

data should be the best possible. The reduced χ^2 is defined as $\tilde{\chi}^2 = \chi^2/d$ where d is the number of degrees of freedom (d.o.f.) in the fit, which is the number of data points minus the number of parameters. The statistic $\tilde{\chi}^2$ is convenient for comparing the result of a fit with the expected value of one. I consider a fit to be good if the value of $\tilde{\chi}^2$ is not much larger than one, which corresponds to an average absolute difference of 1 standard deviation between each datum and the value of the function $F(M)$ at that mass. I may determine the probability of getting a value of $\tilde{\chi}^2$ which is greater than or equal to the value which I measured, and use this as an indicator of the "goodness" of the fit. The probability of obtaining a $\tilde{\chi}^2$ value of greater than one is 50%. For a χ^2 minimization fit with 23 degrees of freedom, the probability of obtaining a $\tilde{\chi}^2$ value of greater than 1.5 is about 6%.

The computer package used for χ^2 minimization is MINUIT [88] and the minimizing technique is a variation of the Davidson-Fletcher-Powell algorithm [89] [90]. The errors on the free parameters are determined in the covariance matrix, also called the error matrix, which is the inverse of the second derivative matrix of χ^2 with respect to the free parameters. The diagonal elements of the covariance matrix (the variances) are the squares of the individual parameter errors, including the effects of correlations with the other parameters. The off-diagonal elements are called the covariances. A statistic which gives the relative magnitude of the correlation between two parameters is the "correlation coefficient", defined as:

$$\rho(x_i, x_j) = \frac{V_{ij}}{V_{ii}V_{jj}} \tag{7.6}$$

where $V_{ii,jj}$ are the variances of parameters x_i and x_j, and V_{ij} is the covariance of these two parameters. If $\rho(x_i, x_j) = 0$, the parameters are uncorrelated. The two parameters are more strongly correlated(anticorrelated) the closer $\rho(x_i, x_j)$ is to $+1(-1)$.

The experimental mass distribution is initially fit with $B(M)$ only, to set good initial values for the free parameters in this function. The distribution is then fit

```
SCAN OF PARAMETER NO.  5
  15.90000     ...   *                  .                  *  .
  15.70000     ...    *                 .                 *   .
  15.50000     ...     *                .                *    .
  15.30000     ...      *               .               *     .
  15.10000     ...       *              .              *      .
  14.90000     ...        *             .             *       .
  14.70000     ...         *            .            *        .
  14.50000     ...          *           .           *         .
  14.30000     ....................*.*&*.*...................
                /        /        /        /        /
          -21.00   -11.00   -1.000    9.000    19.00
```

Figure 7.5: An example of χ^2 vs. $N(M^*)$ for a minimization fit of the function F(M) to the data.

with $F(M|M^*)$ with a fixed value of M^*, allowing the free parameters in $B(M)$ and the variable $N(M^*)$ to vary. When the fit is optimized, $\hat{N}(M^*)$ is the best estimate of the number of $Q^* \rightarrow \gamma q$ events of mass M^*, according to the theoretical model. The fitting process is repeated for values of M^* at 5 GeV intervals between 150 and 550 GeV/c^2.

The signal cross section is given by:

$$\sigma(M^*) = \frac{N(M^*)}{\mathcal{L}\,\epsilon} \tag{7.7}$$

where ϵ is the total detection efficiency, including acceptance, trigger efficiency, and offline cut efficiency.

7.6 Monte Carlo Simulation of $Q^* \rightarrow \gamma q$

The theoretical model described in Sec. 2.1 is incorporated into a Monte Carlo simulation of excited quark production, decay by a "transition" interaction to a ground state quark and photon, and subsequent hadronization and showering in the DØ detector. I examine the simulation data to determine the Q^* event signature.

I generate the decay process $Q^* \rightarrow \gamma q$ using the PYTHIA Monte Carlo program version 5.6 [91] for excited quark masses of 100, 200, 300,...700 GeV; about 1000 events at each mass. Fragmentation and hadronization is performed using JETSET version 7.4 [92],[93]. These events were simulated in the DØ detector environment with the GEANT detector simulation program, DØGEANT version 3.15 [94]. The Monte Carlo model includes both u^* and d^* flavors of spin-1/2 excited state quarks. The distributions of the reconstructed photon-jet invariant mass for Monte Carlo Q^* events simulated at several excited state masses are shown in Figure 7.6.

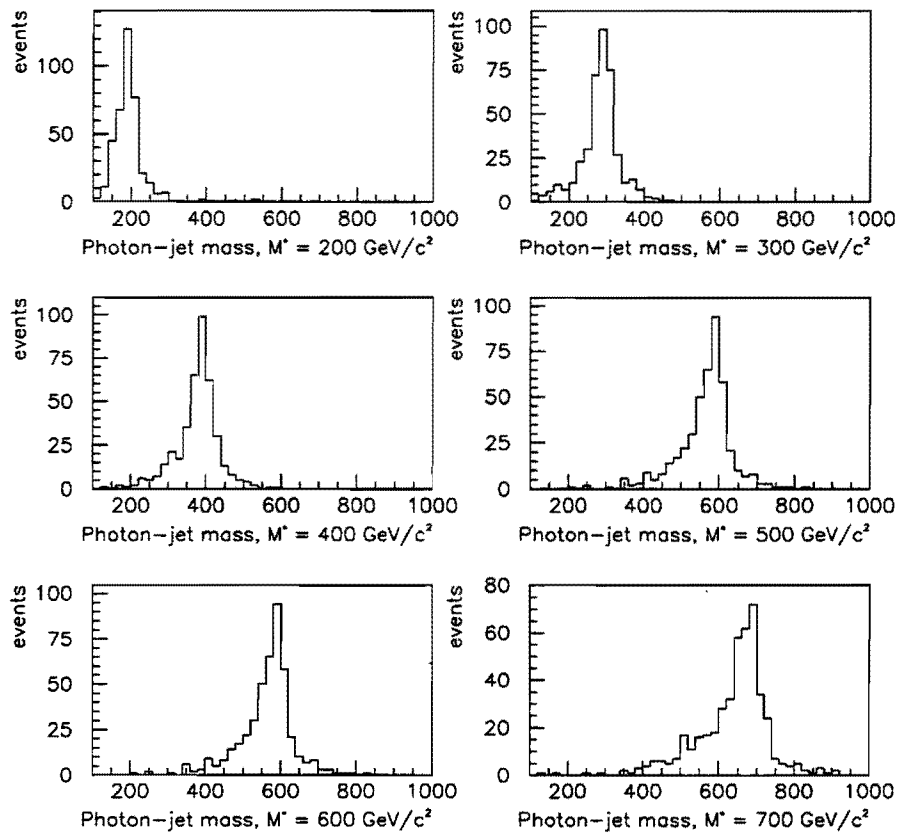

Figure 7.6: Photon-jet invariant mass distributions for Monte Carlo simulated event samples of excited quark decays at several values of M^*.

7.7 A Function for the Q^* Signal Mass Distribution

I fit the Monte Carlo mass distributions with a form of the Breit-Wigner function, given by:

$$S(M|M^*) = \frac{A}{(M - RM^*)^2 + (\frac{W}{2})^2}, \tag{7.8}$$

where M^* is the excited quark mass, W is the full width at half maximum of $S(M|M^*)$, R is defined as $M^{central}/M^*$ where $M^{central}$ is the central value of the Breit-Wigner, and A is a normalization factor, fixed by the requirement that $\int dM S(M|M^*) = 1$. A, W, and R are correlated with the parameterization of the background, so it is necessary to include both signal and background events to determine $A(M^*)$, $W(M^*)$, and $R(M^*)$. The moments of a Breit-Wigner distribution (Cauchy, with non-zero central value) are not defined unless the limits of integration are finite. In this case, the limits are the range of the data.

7.8 A Function for the Background Mass Distribution

I fit the background distribution with a function, $B(M)$. Since most of the experimental data sample is background, a form for the function B(M) is chosen which fits this sample well. Goodness of fit is again determined with a χ^2 test. An exponential function, $B(M) = \exp(A_1 + A_2 M)$, with two free parameters fits the data well over most of the range, but less well at the highest mass values above $300 GeV/c^2$. The function is shown superimposed on the data in Fig. 7.7 with the distribution of χ^2 per bin shown in the lower half of the figure. The values of the free parameters at the minimum χ^2 are given in Table 7.1.

An exponential function with a quadratic term fits the high mass values better with one additional free parameter, but the addition term causes instability in

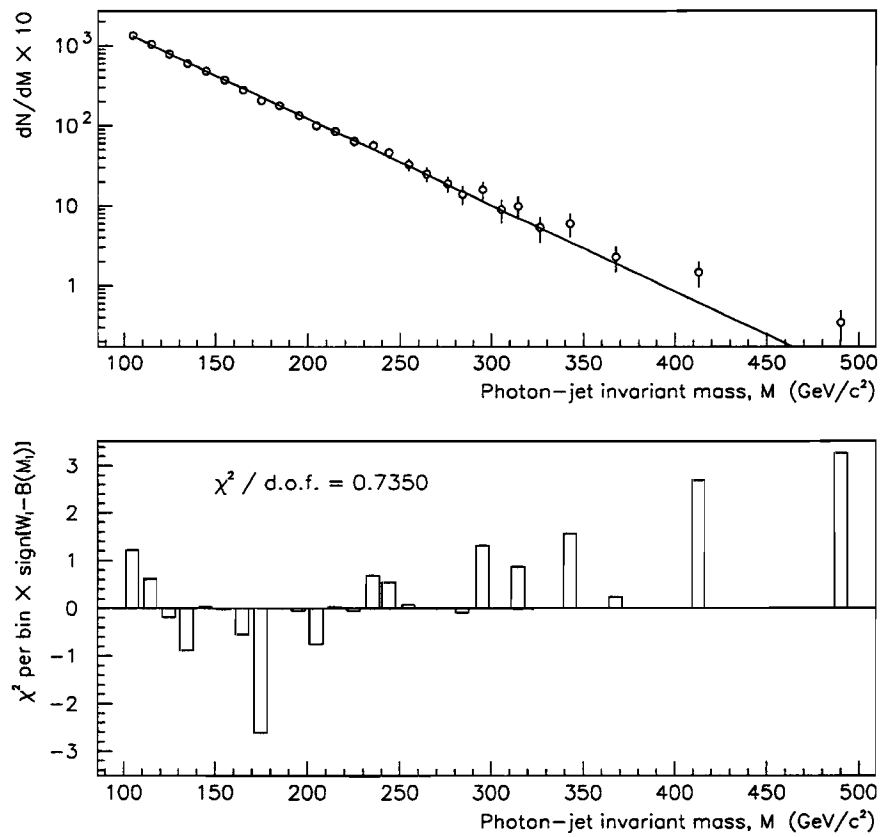

Figure 7.7: The experimental mass distribution with a fit to the function $B(M) = \exp(A_1 + A_2 M)$.

$B(M) = \exp(A_1 + A_2 M)$		
Parameter	Value	Approximate Error
A_1	9.78	5×10^{-2}
A_2	-2.49×10^{-2}	4×10^{-4}
$\chi^2 = 18.4$, d.o.f. $= 25$, $\tilde{\chi}^2 = 0.74$		

Table 7.1: The background function parameter values for a χ^2 minimization fit with an exponential function.

the fitting procedure. The program varies the parameters to extreme values while searching for a minimum χ^2, causing floating point overflow errors. If the parameters are bounded, the minimum χ^2 is found at the bounding value, indicating that the search has settled at a false minimum. When a reasonable minimum is achieved, the covariance matrix is not positive-definite, such that it is unsuitable for error estimation. I can make the fit linear by a change of variables, to $Z = \ln(B(M))$. The function to minimize is then $Z = A_1 + A_2 M + A_3 M^2$ and the data are transformed to $z_i = \ln y_i$ and $\sigma_{z_i} = |dz/dy|\sigma_{y_i} \approx y_i^{-\frac{1}{2}}$. I perform a χ^2 minimization on the function Z and get values for A_1, A_2, A_3. The fit is good, but these parameter values do not fit well when transposing back to the function $B(M)$. Also, $B(M)$ is meant to be summed with $S(M|M^*)$, so a change of coordinates is unusable.

Another drawback to this choice for B(M) is its potential for parabolic behavior. The function describing the background must be locally monotonic. When $S(M|M^*)$ is included at high values of M^*, the cross section for the background reaches a minimum value and then rises again.

A sum of two exponential functions for $B(M)$ fits the data well with four free parameters. The function is monotonic and the fit is better at high mass values, as

shown in Fig. 7.8. Table 7.2 shows the parameter values at the minimum χ^2. I chose the sum of two exponential functions to use for B(M) in the mass fitting analysis.

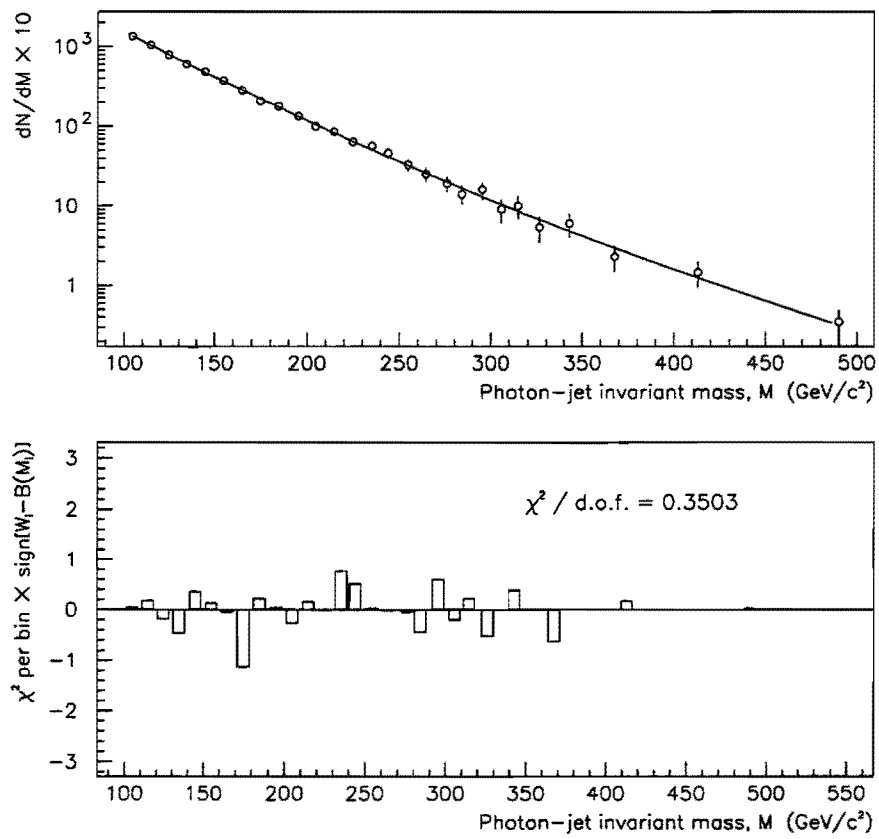

Figure 7.8: The experimental mass distribution with a fit to the function $B(M) = \exp(A_1 + A_2 M) + \exp(A_3 + A_4 M)$.

The value of $\bar{\chi}^2$ in this fit is 0.34. A value of $\bar{\chi}^2$ much lower than one is often an indication that the errors have been overestimated, or that the data are correlated. Neither of these two cases apply. The unweighted data in this distribution are the reconstructed photon-jet masses of independent collider events, and the errors are statistical. Table 7.3 shows the complete data for individual bins in the fit. The

$B(M) = \exp(A_1 + A_2 M) + \exp(A_3 + A_4 M)$		
Parameter	Value	Approximate Error
A_1	6.5	0.2
A_2	-1.58×10^{-2}	9×10^{-4}
A_3	9.96	0.06
A_4	-2.73×10^{-2}	4×10^{-4}
$\chi^2 = 7.73$, d.o.f. $= 23$, $\tilde{\chi}^2 = 0.34$		

Table 7.2: The background function parameter values for a χ^2 minimization fit with a double exponential function $B(M) = \exp(A_1 + A_2 M) + \exp(A_3 + A_4 M)$.

probability of obtaining a value of $\tilde{\chi}^2$ less than 0.34 in a fit with 23 degrees of freedom is 0.4%.

7.9 Fixing the Parameterization of the Signal Function

The next step is to fix the parameterization of the signal function, $S(M|M^*)$.

The function B(M) has been chosen, as described in the last section. A histogram of binned values is produced, where the bin width is 10 GeV and the bin content is $B(M_i)$ at the average mass value of the bin, M_i. The number of events in the artificial mass distribution is equal to that of the experimental data sample. The contents of each bin are smeared according to a Poisson probability density function. Fig. 7.9 shows the artificial background sample compared with the real experimental mass distribution.

To confirm that the artificial background distribution is consistent with the data, I perform a binned Kolmogorov two-sample test [95]. The null hypothesis is that

M_i	y_i	σ_i	$B(M_i)$	χ_i^2	M_i	y_i	σ_i	$B(M_i)$	χ_i^2
104.7	1348	36.72	1340.	0.048	243.9	46	6.782	41.17	0.506
114.7	1045	32.33	1031.	0.177	254.6	33	5.745	32.12	0.023
124.6	785	28.02	797.0	0.183	264.5	25	5.000	25.61	0.015
134.5	600	24.49	616.7	0.462	275.8	19	4.359	19.85	0.038
144.8	486	22.05	473.0	0.350	284.1	14	3.742	16.51	0.450
154.8	373	19.31	366.2	0.125	295.3	16	4.000	12.92	0.594
164.9	280	16.73	283.3	0.038	305.5	9	3.000	10.37	0.208
174.7	206	14.35	221.2	1.126	314.7	10	3.162	8.530	0.216
184.6	179	13.38	172.7	0.222	326.3	5.33	1.886	6.700	0.525
195.2	135	11.62	132.8	0.037	342.8	6.000	2.000	4.776	0.375
204.7	100	10.00	105.1	0.265	367.6	2.286	0.808	2.924	0.622
214.8	86	9.274	82.25	0.163	413.0	1.455	0.514	1.244	0.167
224.9	64	8.000	64.52	0.004	490.1	0.343	0.140	0.3215	0.023
235.3	57	7.550	50.39	0.766					
$\chi^2 = 7.73$, d.o.f. $= 23$, $\tilde{\chi}^2 = 0.34$									

Table 7.3: Values of the mass, bin contents, statistical error, function $B(M)$, and χ^2 per bin for the fit with a double exponential function $B(M) = \exp(A_1 + A_2 M) + \exp(A_3 + A_4 M)$.

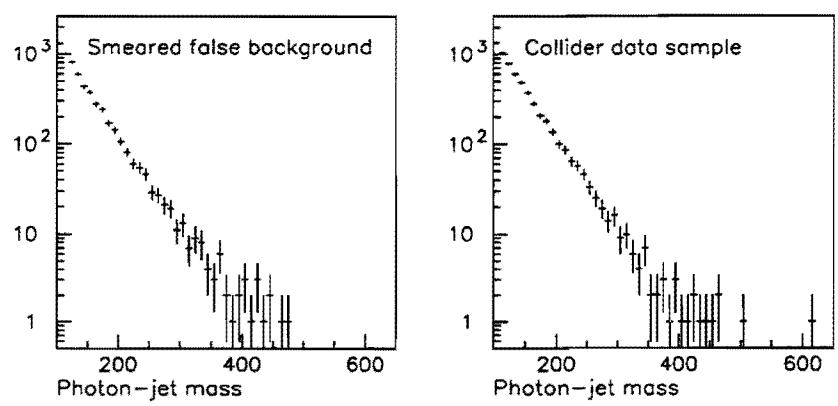

Figure 7.9: *left:* The mass distribution of a sample of artificial background, produced by smearing the bin values of a histogram of the function B(M). *right:* The experimental photon-jet mass distribution.

the two histograms come from the same parent distribution. The test returns a probability of 0.664. This is the probability of rejecting the null hypothesis when it is actually true. If two sets which are independently sampled from the same parent distribution are compared with the Kolmogorov test, then they will return a smaller probability of the null hypothesis 66.4% of the time. A comparison of two identical samples returns a probability of 100%. The alternative to the null hypothesis is an infinite set, so it is not meaningful to try to express the probability that two histograms come from different distributions. The probability is not a confidence level, because the background was not produced independently of the data. The parameters in $B(M)$ were determined in a χ^2 minimization fit to the data. Nevertheless, the test confirms that there is good agreement between the artificial background and data.

An acceptable background distribution has been modeled. Monte Carlo signal events are added to simulate a combined distribution. The histograms of mixed signal and background are rebinned with merging as necessary. The function $F(M|M^*)$ is fit to the artificial data sample at the value of M^* corresponding to the Monte Carlo sample which was added. The χ^2 minimization is performed with $N(M^*)$, the number of Monte Carlo signal events, fixed while the parameters in $B(M)$ and $S(M|M^*)$ are allowed to vary in the fit. An example of one of the fits is displayed in Fig. 7.10, showing a sample of false background with 402 Monte Carlo generated Q^* events added at $M^* = 300\ GeV/c^2$. The Kolmogorov two-sample test is performed on this example, comparing it to the experimental mass distribution. The probability of the null hypothesis is 1.15×10^{-9}. It is not likely that the two samples come from the same distribution.

The best values of parameters A, W, and R are found at each of five excited quark mass values by χ^2 minimization . The values of each parameter are fitted with a polynomial function of M^*. The parameter values and the polynomial functions

are displayed in Table 7.4 and Fig. 7.11. A χ^2 fit with N allowed to vary and the polynomial functions $A(M^*)$, $W(M^*)$, and $R(M^*)$ fixed yields the correct number of Monte Carlo signal events to within errors. This result is also true for smaller or larger numbers of signal events added to the background.

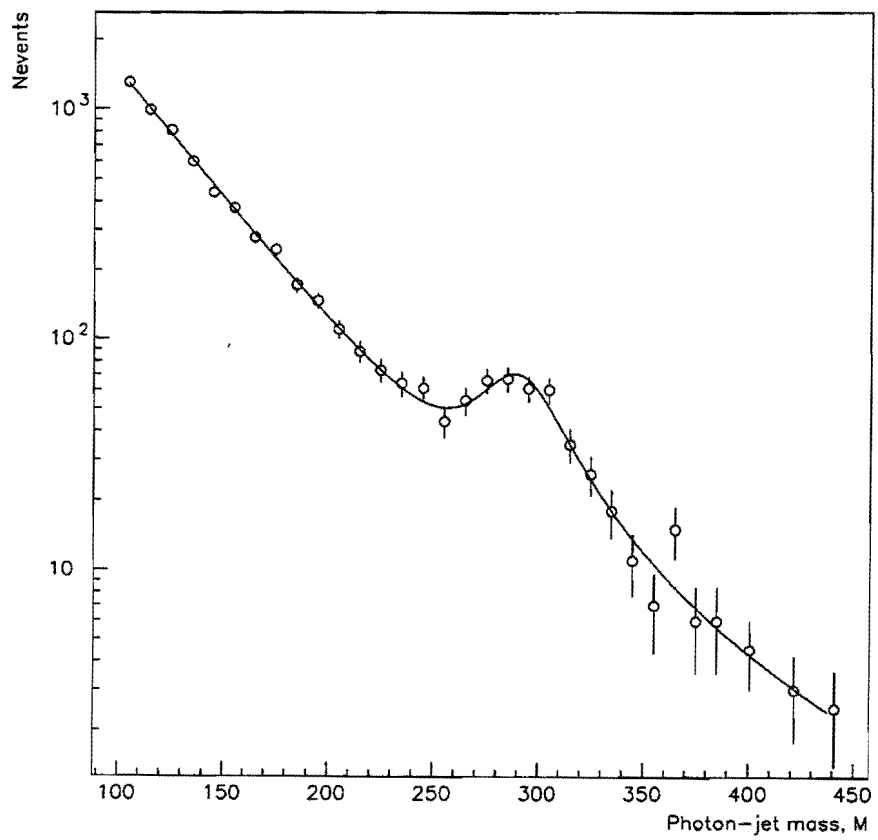

Figure 7.10: An example of the results of a χ^2 fit performed to optimize the parameterization of $S(M|M^*)$. $M^* = 300$ GeV.

7.10 Uncertainty in the Parameterization of the Signal Function

Q^* mass	A	W	R
200 GeV	190 ± 77	57.7 ± 12.3	0.9283 ± 0.0160
300 GeV	98 ± 15	52.7 ± 5.3	0.9653 ± 0.0085
400 GeV	72 ± 12	47.5 ± 5.1	0.9714 ± 0.00502
500 GeV	89 ± 11	56.2 ± 4.7	0.9601 ± 0.00334
600 GeV	78 ± 10	54.8 ± 4.8	0.9684 ± 0.00404

$$A = 925.03 - 5.8053M^* + 1.2933 \times 10^{-2}M^{*2} - 9.3465 \times 10^{-6}M^{*3}$$

$$\Delta A = 451.36 - 3.0306M^* + 6.7608 \times 10^{-3}M^{*2} - 4.8954 \times 10^{-6}M^{*3}$$

$$W = -182.55 + 3.042M^* - 1.3523 \times 10^{-2}M^{*2} + 2.4792 \times 10^{-5}M^{*3} - 1.6008 \times 10^{-8}M^{*4}$$

$$\Delta W = 52.732 - 0.32617M^* + 7.2097 \times 10^{-4}M^{*2} - 5.1822 \times 10^{-7}M^{*3}$$

$$R = .60814 + 2.6547 \times 10^{-3}M^* - .62776 \times 10^{-6}M^{*2} + 4.7555 \times 10^{-9}M^{*3}$$

$$\Delta R = 3.6270 \times 10^{-2} - 1.2878 \times 10^{-4}M^* + 1.2536 \times 10^{-7}M^{*2}$$

Table 7.4: The parameterization of $S(M|M^*)$ from fits to Monte Carlo Q^* decay events plus background. The values of variables A(M^*), W(M^*), and R(M^*) are given for several excited quark masses M^*. Also given are the polynomial functions which fit the parameters between data points, and polynomial functions which fit the error on the paramters as a function of M^*.

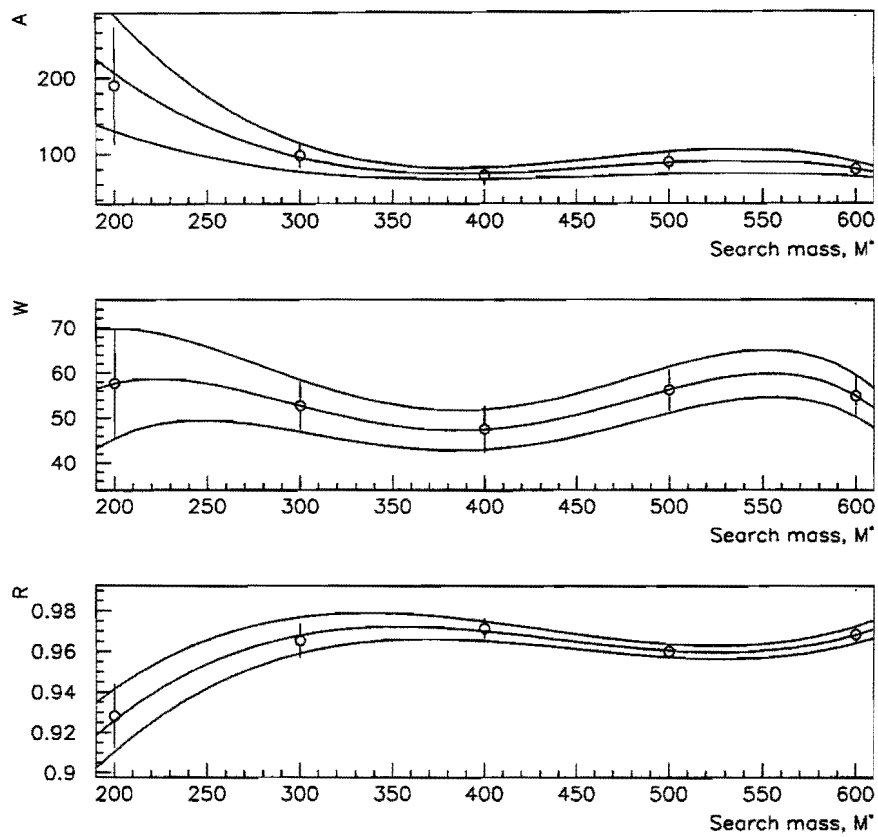

Figure 7.11: Values of A(M^*), W(M^*), and R(M^*) used in the parameterization of $S(M|M^*)$, displayed with their uncertainties at several values of M^*. The inner curves through the data points are polynomial fits to the discrete values of the parameters. The outer curves, above and below, are polynomial fits to the discrete values $\pm 1\sigma$ errors ΔA(M^*), ΔW(M^*), and ΔR(M^*).

Error is introduced in the determination of $N(M^*)$ due to the uncertainty in the parameterization of $S(M|M^*)$, as seen in Fig. 7.11. I refer to this error as ΔN_{par}. I change the parameters in $S(M|M^*)$ by $\pm 1\sigma$ and refit the experimental mass distribution to determine the variation in $N(M^*)$. I refit the distribution with

$$S(M|M^*) = \frac{A}{(M - [R \pm \Delta R] \cdot M^*)^2 + (\frac{[W \pm \Delta W]}{2})^2} \tag{7.9}$$

to get several results for $N(M^*)$ at each value of M^* in addition to the original fit with the best values of the parameters. The standard deviation of the values of N is an estimate of ΔN_{par}.

M^*	$N_{R,W}$	$N_{R+\Delta R,W+\Delta W}$	$N_{R+\Delta R,W-\Delta W}$	$N_{R-\Delta R,W+\Delta W}$	$N_{R-\Delta R,W-\Delta W}$	ΔN_{par}
150	-16.42	-11.71	-11.85	-17.84	-19.76	27.56
200	-11.80	-9.30	-2.10	-4.90	-8.88	3.45
250	31.76	43.77	29.11	30.38	34.81	5.26
300	-2.81	-13.81	-3.11	-5.09	-5.79	4.01
350	-0.07	-2.74	0.38	-0.79	0.69	1.22
400	-1.42	-1.11	-0.87	-2.31	-2.93	0.77
450	1.23	1.81	1.28	1.18	1 43	0.23
500	0.098	-0.068	-0.069	-0.067	-0.041	0.28
550	1.02	3.00	-0.12	1.20	-0.18	1.15
$\Delta N_{par}(M^*) \approx -13.359 + 0.18864\ M^* - 6.1807 \times 10^{-}4\ M^{*2} + 5.8848 \times 10^{-7}\ M^{*3}$						

Table 7.5: Several values of $N(M^*)$ as found in the χ^2 minimization fit with different parameterizations of the signal function $S(M|M^*)$. The change in the parameterization is noted as a subscript on N at the top of each column. The last column is ΔN_{par} as estimated from the standard deviation of the values of N for different parameterizations. The last row is a polynomial fit to all discrete values of ΔN_{par}.

CHAPTER 8
ANALYSIS OBSERVATIONS

8.1 Fitting the Experimental Mass Distribution

The experimental mass distribution of the data sample described in Chapter 5 is fit repeatedly with the function $F(M|M^*)l$ at 5 GeV intervals in M^* . The results of these fits are shown in Fig. 8.1. The uncertainty decreases with increasing mass up to the last data point, where it begins to increase again.

8.2 Checks on the Reliability of χ^2 Fit Results

I would like for $N(M^*)$ be as insensitive as possible to the form of the function that I choose for $B(M)$, but the number of signal events $N(M^*)$ and the parameters in $B(M)$ are correlated. I check the sensitivity of the fit to my choice of background function by comparing results with a second form for $B(M)$ which does not use exponential functions. The result is shown in Fig. 8.2 along with the double exponential result. This function is given by [96]:

$$B(M) = A_1(1 - M/\sqrt{s})^{A_2}/M^{A_3} \; + \; A_4(1 - M/\sqrt{s})^{A_5}/M^{A_6} \qquad (8.1)$$

Using these different choices of $B(M)$, $N(M^*)$ varies by 0-10 events. The variation is smaller than the scale of the error, ΔN.

As a cross-check on the results of the χ^2 minimization fits for $\hat{N}$ and ΔN, I perform the χ^2 fit on many samples of artificial background to see if the mean

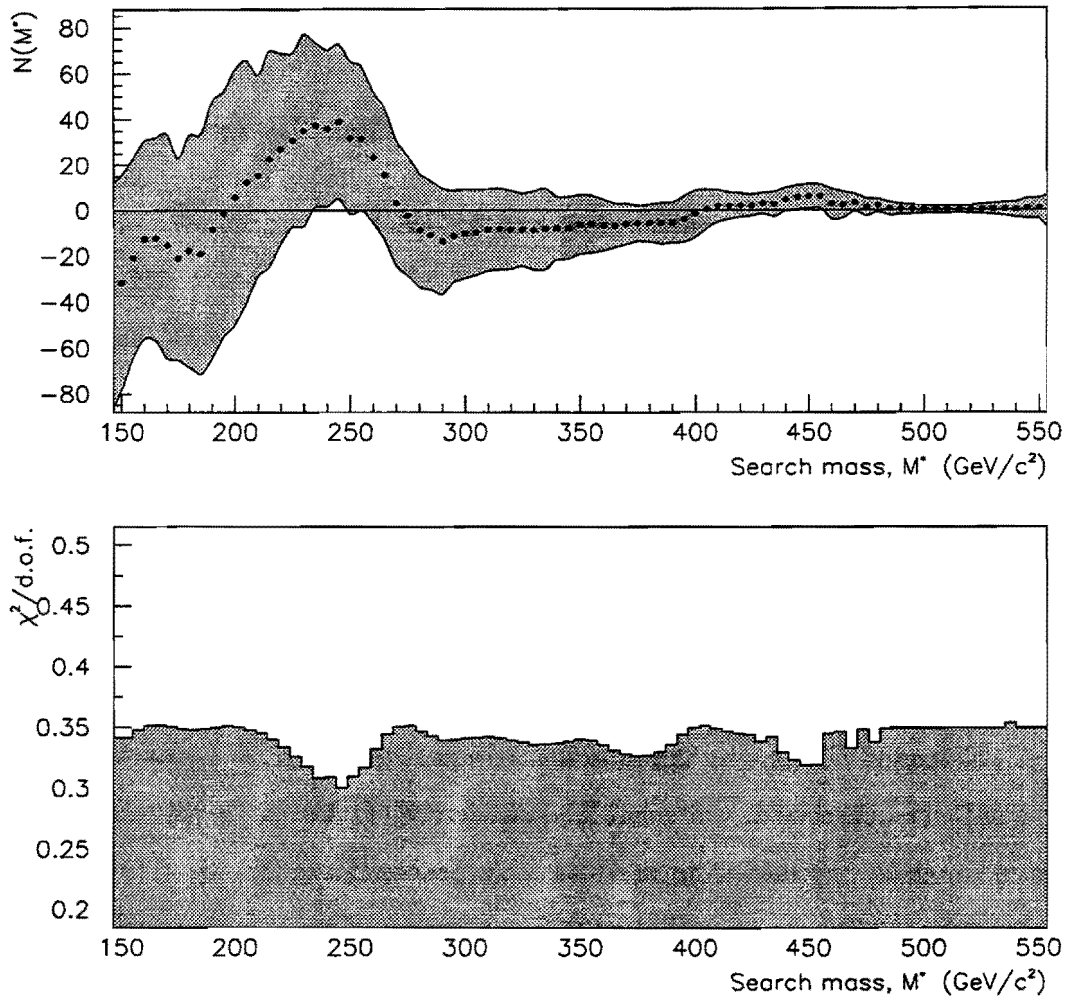

Figure 8.1: *top:* The best value of the number of signal events $\hat{N}(M^*)$ from independent fits of $F(M|M^*)$ to the experimental mass distribution at 5 GeV intervals in M^*. The combined statistical and systematic error is displayed as a shaded band around the data points. *bottom:* The values of $\tilde{\chi}^2$ vs. M^* for the same minimization fits.

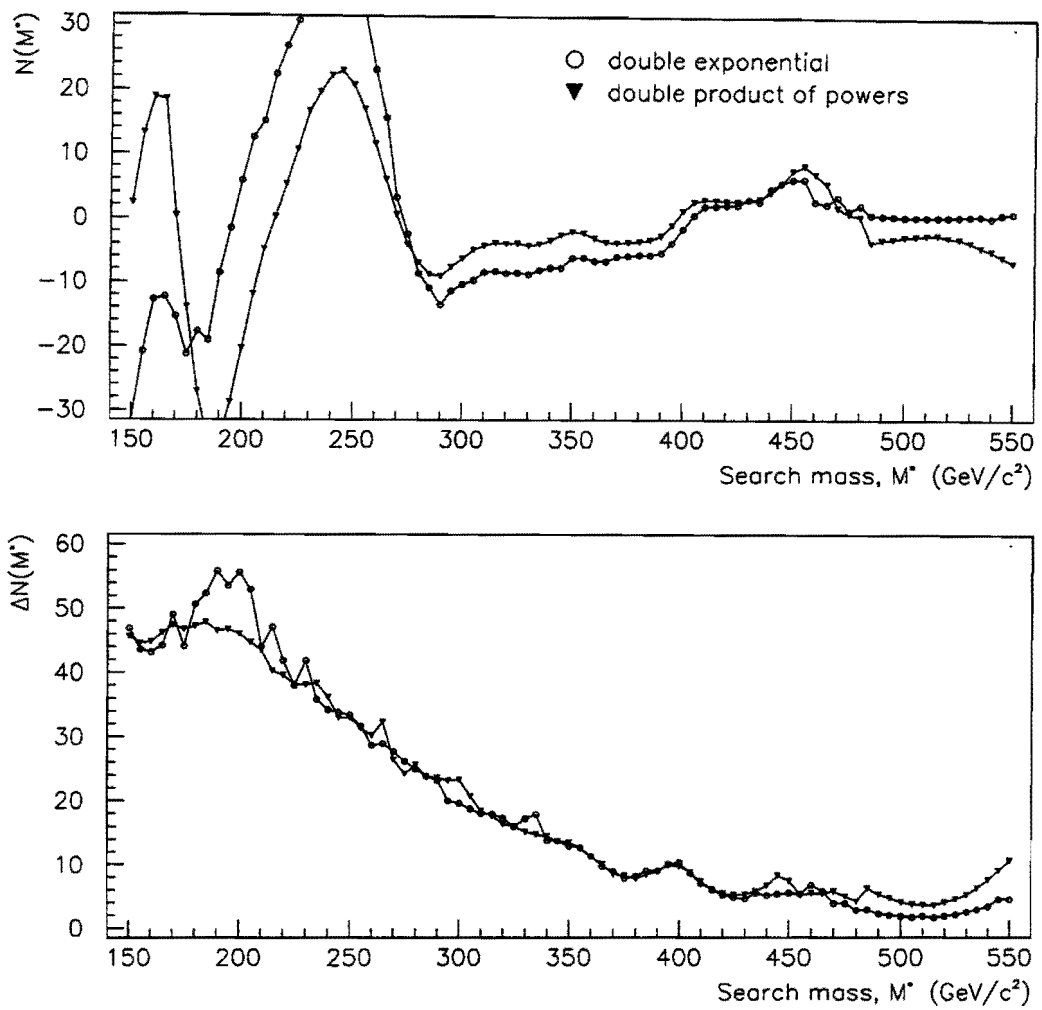

Figure 8.2: The best values of the number of signal events $\hat{N}(M^*)$ and the error $\Delta N(M^*)$ from χ^2 minimization fits performed with a sum of two exponential functions $B(M) = e^{(A_1+A_2M)} + e^{(A_3+A_4M)}$ compared with the same from fits performed with a sum of two "product of powers" functions $B(M) = A_1\frac{(1-M/s^{1/2})^{A_2}}{M^{A_3}} + A_4\frac{(1-M/s^{1/2})^{A_5}}{M^{A_6}}$.

number of signal events found is zero and the standard deviation of the number of signal events is consistent with the error in the covariance matrix.

Consider the number of events in a peak as a sum of signal events N_S and a random component from statistical fluctuations N_R.

$$N(M^*) = N_S(M^*) + N_R(M^*) \tag{8.2}$$

If the distribution contains background only, $N_S = 0$. The expectation value of N_R is zero, and the variance of N_R is the scale for determining the significance of a peak. The variance of $N(M^*)$ from the experimental mass distribution is compared with the variance of $N(M^*)$ from artificially generated background.

I produce 20 samples of artifical background, according to the method described in Sec. 7.9. Each sample contains the same number of events as the collider data sample. These samples are fit with $F(M|M^*, N)$ at $M^* = 150, 200, 250, ..., 450$ GeV/c^2. For each M^*, the number of events $N(M^*)$ and error $\Delta N(M^*)$ are determined in a fit. The distributions of $N(M^*)$, weighted by $1/(\Delta N)^2$ are shown in Fig. 8.3. The weighted sample mean and sample variance are given by:

$$\bar{x} = \frac{\sum_{i=1}^{20} \frac{N_i}{(\Delta N_i)^2}}{\sum_{i=1}^{20} \frac{1}{(\Delta N_i)^2}} \tag{8.3}$$

$$s^2 = \frac{\sum_{i=1}^{20} \frac{(N_i - \bar{x})^2}{(\Delta N_i)^2}}{\sum_{i=1}^{20} \frac{1}{(\Delta N_i)^2}} \tag{8.4}$$

As seen in Fig. 8.4, the sample average ($\bar{x}$) is consistent with zero events, which it should be if the fits are not biased. The sample variance s^2 of the artificial background is compared with the variance $(\Delta N)^2$ from fits to the experimental mass distribution. The two results are consistent. The sample variance s^2 does not take into account correlations between free parameters, so this comparison suggests that the error estimates are not strongly influenced by correlations. Agreement is best where the number of events per bin is large, and the free parameters in $B(M)$

are constrained by data points above and below the fit mass, M^*. In the upper mass region of the distribution, significant correlations between $N(M^*)$ and the free parameters in $B(M)$ produce a larger error $\Delta N(M^*)$.

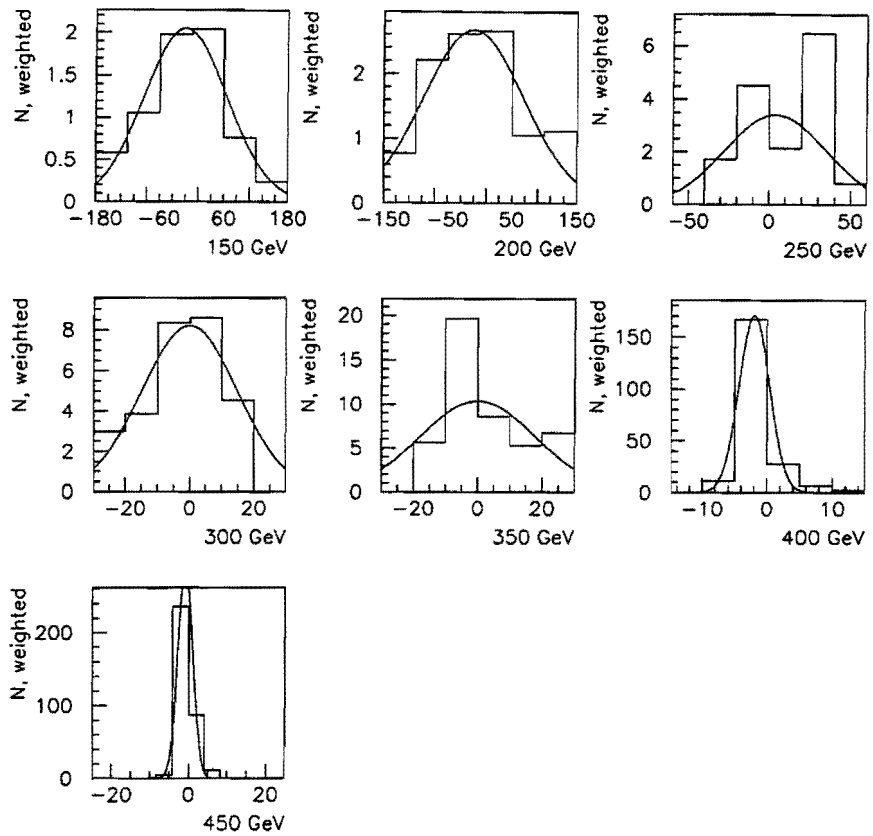

Figure 8.3: The distribution of the best values of the number of signal events $\hat{N}(M^*)$ for 20 samples of artificial background without any signal events adden, at each of several values of M^* ($M^* = 150, 200, 250, ..., 450$ GeV).

8.3 Significance of the Number of Observed Signal Events

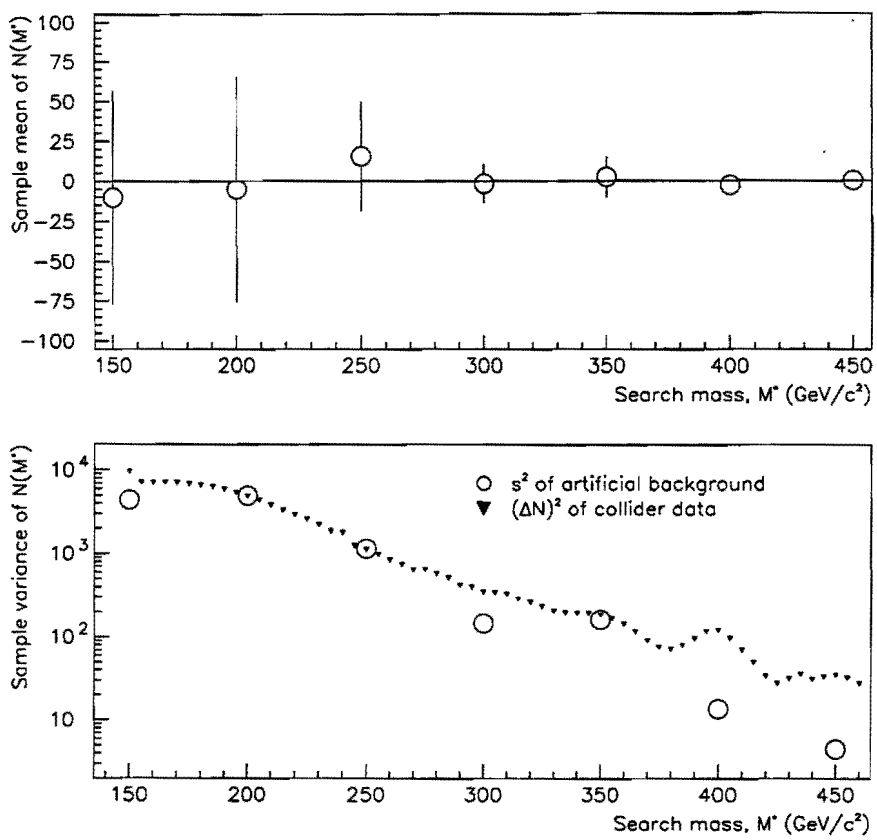

Figure 8.4: The sample mean and sample variance of the $\hat{N}(M^*)$ distributions of Fig. 8.3 vs. M^*.

To confirm a significant signal observation, there must be a contribution to the photon-jet cross section in excess of the background of at least four to five standard deviations [87]. In this section, I determine the significance of the number of events measured.

The following is a summary of a discussion on fitting mass distributions which is presented in [97]. I introduce a mass distribution in which a resonance appears, seen as a peak centered at a mass value M_0. A mass range is chosen from M_a to M_b which includes all the events in the resonance. The number of events in this range is N_{tot} and the number of background events is N_{back}. It is desired to know the probability that the observed effect at the mass value $M = M_0$ is a statistical fluctuation in $B(M)$. The null hypothesis is that all events in the data sample are attributable to background. In this case, $N_{tot} = N_{back}$ and the variance of N_{tot} is given by:

$$V(N_{tot}) = N_{tot} = N_{back} \tag{8.5}$$

The variance of the difference $V(N_{tot} - N_{back})$ is less than or equal to the sum of their individual variances $V(N_{tot})$ and $V(N_{back})$. If N_{tot} and N_{back} are completely uncorrelated, then:

$$V(N_{tot} - N_{back}) = V(N_{tot}) + V(N_{back}) = N_{back} + V(N_{back}). \tag{8.6}$$

If N_{tot} is not too small, it is justified to approximate it as a normal variable. To test the null hypothesis, I define a statistic s, which I will call the "significance" of the peak, by:

$$s = \frac{N_{tot} - N_{back}}{\sqrt{V(N_{tot} - N_{back})}} \approx \frac{N_{tot} - \hat{N}_{back}}{\sqrt{\hat{N}_{back} + V(\hat{N}_{back})}}, \tag{8.7}$$

where $\hat{N}_{back} = \int_{M_a}^{M_b} dM\ B(M)$ is the best estimate of N_{back} and $V(\hat{N}_{back})$ is the square of the error on $\hat{N}_{back}$. The variable s is approximately normal if the null hypothesis is true, so the units of s are standard deviations.

In this analysis, the mass range M_a to M_b is from $100 - 550 GeV/c^2$. A single fit yields $N(M^*)$, the number of events in a peak centered at $M_0 = M^*$, given by:

$$N(M^*) = N_{tot} - N_{back}. \tag{8.8}$$

From equations 8.7 and 8.8, the significance of $N(M^*)$ is given by:

$$s = \frac{N(M^*)}{\Delta N(M^*)}, \tag{8.9}$$

where $\Delta N(M^*) = \sqrt{V(N(M^*))}$.

The error $\Delta N(M^*)$ is the scale for determining the significance of $N(M^*)$. Figure 8.5 shows $N/\Delta N$ and $\tilde{\chi}^2$ as a function of M^*. If there is a signal contribution, the value of $\tilde{\chi}^2$ should be smallest at the correct value of M^* and larger at other values. In the distribution of $N/\Delta N$, the largest deviation from a null result is about 1.1σ. There is no substantial evidence in this measurement to suggest a contribution to the mass distribution from the process $Q^* \rightarrow \gamma q$, according to the theoretical model outlined in Sec. 2.1.

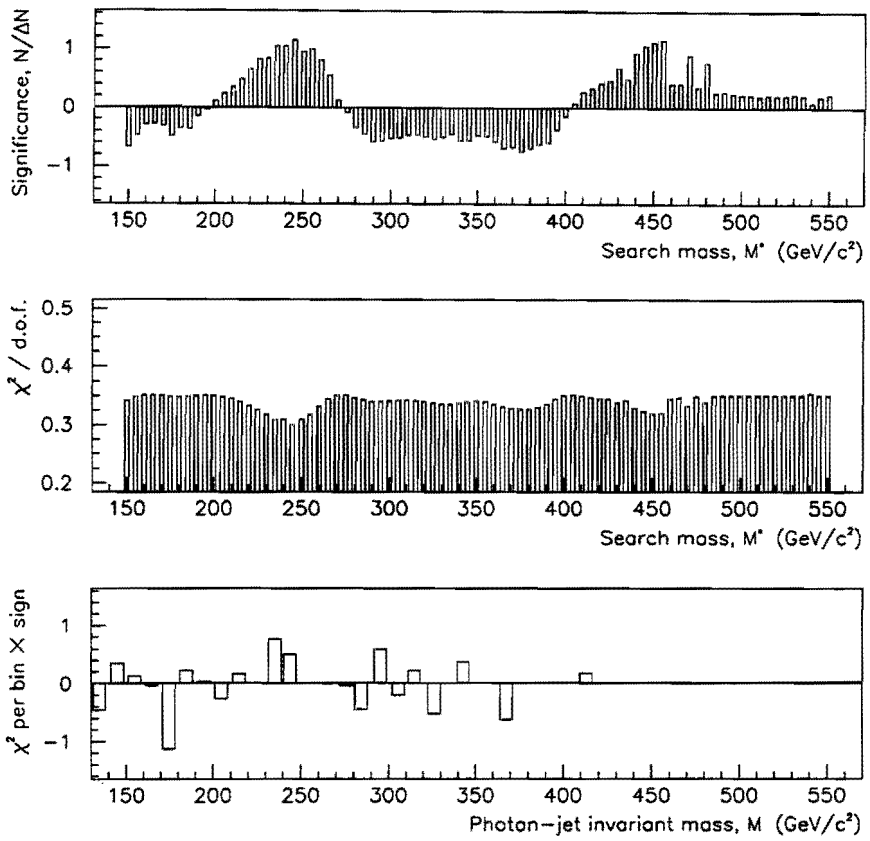

Figure 8.5: The photon-jet experimental data sample *top:* significance $N/\Delta N$ vs. M^*, *middle:* $\bar{\chi}^2$ vs. M^*, and *bottom:* χ^2 per bin $\times \frac{y_i - B(M_i)}{|y_i - B(M_i)|}$ vs. M^*. The symbols y_i and M_i denote the contents of bin i (either the number of events in the bin, or the weight of a merged bin) and the average mass integrated over the range of the bin ($M_i = \frac{\int dM\ M\ B(M)}{\int dM\ B(M)}$).

CHAPTER 9
ESTABLISHING CONFIDENCE LIMITS

This chapter describes a prescription for establishing an upper limit on the signal cross section at the 95% confidence level. Section 9.1 describes the orthodox method of establishing a confidence level from hypothetical frequency distributions and notes the difficulty with this approach. Section 9.2 presents a statement and proof of Bayes' theorem, generalizes Bayes' theorem to cases involving continuous probability distributions, and states Bayes' postulate. Section 9.2 describes how Bayes' theorem may be used to establish an upper limit on the cross section, by following a rigorous prescription for incorporating necessary assumptions and by using all available information from the experiment. Section 9.4 gives confidence limit results and discusses the dependency of the results on the theoretical model to which the measurement is compared.

9.1 Establishing a Confidence Limit from Frequency Distributions

References which discuss the "orthodox" approach to probability include [100] and [101].

According to the orthodox method of establishing probability, the question I should pose to define an upper limit at some confidence level is, "For what value σ_{UL} of the cross section is the probability of observing more events than I did in this experiment equal to CL?". Given my best estimate $\hat{N}$ of the the number of signal events observed N, my best estimate $\hat{\mathcal{L}}$ of the integrated luminosity $\mathcal{L}$, and

my best estimate $\hat{\epsilon}$ of the detection efficiency ϵ for my signal events, the value σ_{UL} is the solution to the equation:

$$CL = \int_{\hat{N}}^{\infty} dN\ p(N|\sigma_{UL}, \hat{\mathcal{L}}, \hat{\epsilon}), \tag{9.1}$$

where the number of signal events is N and the conditional probability $p(N|\sigma_{UL}, \mathcal{L}, \epsilon)$ is assumed to be a Poisson distribution:

$$p(N|\sigma_{UL}, \mathcal{L}, \epsilon) = \frac{e^{-\sigma_{UL}\mathcal{L}\epsilon}(\sigma_{UL}\mathcal{L}\epsilon)^{\hat{N}}}{\hat{N}!}, \tag{9.2}$$

which is the frequency distribution of a hypothetical ensemble of independent repetitions of the experiment. This distribution will change with the inclusion of any additional knowledge from independent measurements. There is no prescription in this method for handling uncertainties. The experimenter recognizes the need to include errors, so ad hoc "smearing" of the measured quantities (integrating over hypothetical frequency distributions) is put into (9.1), given by:

$$CL = \int_0^{\infty} d\mathcal{L} \int_0^1 d\epsilon \int_{\hat{N}}^{\infty} dN\ p(\mathcal{L})\ p(\epsilon)\ p(N)\ p(N|\sigma_{UL}, \mathcal{L}, \epsilon), \tag{9.3}$$

where the probability distributions for the experimental quantities are given by:

$$p(N) = \frac{1}{\sqrt{2\pi(\Delta N)}} \exp \frac{-(N - \hat{N})^2}{2(\Delta N)^2}, \tag{9.4}$$

$$p(\mathcal{L}) = \frac{1}{\sqrt{2\pi(\Delta \mathcal{L})}} \exp \frac{-(\mathcal{L} - \hat{\mathcal{L}})^2}{2(\Delta \mathcal{L})^2}, \tag{9.5}$$

and

$$p(\epsilon) = \frac{1}{\sqrt{2\pi(\Delta \epsilon)}} \exp \frac{-(\epsilon - \hat{\epsilon})^2}{2(\Delta \epsilon)^2}. \tag{9.6}$$

The quantities ΔN, $\Delta \mathcal{L}$, and $\Delta \epsilon$ are the uncertainties on the values $\hat{N}$, $\hat{\mathcal{L}}$, and $\hat{\epsilon}$, respectively.

9.2 Bayes' Theorem and Bayes' Postulate

References which discuss Bayesian methods include [102], [103], [104], [105], [106], [107], [108], and [109]. For further details, see these sources.

The upper limit on the cross section is calculated using Bayes' theorem, stated and proven here. A sample space is spanned by n mutually exclusive and exhaustive subsets B_i. The probability of an event belonging to a set B_i is expressed as $P(B_i)$, and satisfies $\sum_{j=1}^{n} P(B_j) = 1$. Set A also belongs to the sample space. It contains the events observed in an experiment. The prior probability $P(B_i)$ (also called the "prior") is the probability that an event belongs to set B_i. The conditional probability $P(B_i|A)$, called the posterior probability, is the probability that an event belongs to B_i, given that it is observed in set A. The conditional probability $P(A|B_i)$, called the likelihood, is the probability that an event will be observed in set A, given that it belongs to set B_i. The terms "prior" and "posterior" have nothing to do with chronological order. Prior knowledge is independent of the observation. A prior assumption is made with incomplete knowledge, and is accepted without proof (hence the term "a priori"). Posterior knowledge is obtained as a result of the observation.

The probability that an event belongs to both sets A and B_i is given by:

$$P(A \cap B_i) = P(B_i|A)P(A) = P(A|B_i)P(B_i). \tag{9.7}$$

From this equation, I find that the posterior probability may be expressed as:

$$P(B_i|A) = \frac{P(A|B_i)P(B_i)}{P(A)} \tag{9.8}$$

Since each event belongs to one and only one of the sets B_i, the probability of an event belonging to set A may be written as a sum of intersections between sets,

$$P(A) = \sum_{j=1}^{n} P(A \cap B_j) = \sum_{j=1}^{n} P(A|B_j)P(B_j). \tag{9.9}$$

Substituting this into (9.8), I get:

$$P(B_i|A) = \frac{P(A|B_i)P(B_i)}{\sum_{j=1}^{n} P(A|B_j)P(B_j)}. \tag{9.10}$$

This equation is Bayes' theorem. It expresses the posterior probability in terms of prior assumptions and likelihoods.

In some situations B_i are not discrete sets, but rather a continuous distribution of prior probabilities. Bayes' theorem is expressed in terms of probability density functions as:

$$\int_a^b dn\ p(n|N) = \frac{\int_a^b dn\ p(N|n)\ p(n)}{\int_{-\infty}^{\infty}\ dn\ p(N|n)\ p(n)}. \tag{9.11}$$

This equation expresses the probability that $a < n \leq b$, given that I have observed N. If I have no reason to favor one hypothesis n over another, then one possiblity is to assign a constant prior $p(n) = 1$ (unnormalized), such that all n are equally probable. Equation (9.11) becomes:

$$\int_a^b dn\ p(n|N) = \frac{\int_a^b dn\ p(N|n)}{\int_{-\infty}^{\infty} dn\ p(N|n)}. \tag{9.12}$$

This is Bayes' postulate.

9.3 Establishing a Confidence Limit with Bayesian Methods

Following the Bayesian approach to statistical inference, the question posed in this analysis is, "Given my incomplete knowledge of N, $\mathcal{L}$, and ϵ, for what value of the cross section σ_{UL} is the probability that the true value of the cross section is smaller equal to CL?". The value σ_{UL} is the solution to the equation:

$$CL = \int_0^{\sigma_{UL} d\sigma_{UL}\ p(\sigma|N,\mathcal{L},\epsilon}), \tag{9.13}$$

where $p(\sigma|N, \mathcal{L}, \epsilon)$ is the posterior probability of cross section σ given some level of knowledge about N, $\mathcal{L}$, and ϵ. This equation is solved using Bayes' theorem. The

sample space is the set which includes all possible values of the cross section between zero and the total minimum bias cross section σ_{MB}, as defined in section 4.1. The hypothesis is the set which includes values of the cross section between zero and σ_{UL}. The observation is the best estimate of the number of signal events $\hat{N}$ and the uncertainty ΔN from a χ^2 minimization fit . The prior knowledge is the cross section σ, the luminosity $\mathcal{L}$, and the detection efficiency ϵ. The answer is given by:

$$CL = \frac{\int_0^{\sigma_{UL}} d\sigma \int_0^{\infty} d\mathcal{L} \int_0^1 d\epsilon \; p(N|\sigma,\mathcal{L},\epsilon)\; p(\sigma)\; p(\mathcal{L})\; p(\epsilon)}{\int_0^{\sigma_{MB}} d\sigma \int_0^{\infty} d\mathcal{L} \int_0^1 d\epsilon \; p(N|\sigma,\mathcal{L},\epsilon)\; p(\sigma)\; p(\mathcal{L})\; p(\epsilon)}. \tag{9.14}$$

The best estimate of the number of signal events $\hat{N}(M^*)$ and the uncertainty $\Delta N(M^*)$ is my observation, determined in a χ^2 minimization fit to the mass distribution. I make the a priori assumption that the function which best expresses the likelihood of this observation is a gaussian, given by:

$$p(\hat{N},\Delta N|\sigma,\mathcal{L},\epsilon) = \frac{1}{\sqrt{2\pi(\Delta N)}} \exp \frac{-(\hat{N}-\sigma\mathcal{L}\epsilon)^2}{2(\Delta N)^2}. \tag{9.15}$$

If I were doing a "counting" experiment, in which there is no uncertainty on the number of events $\hat{N}$, then a good choice for the function to express the likelihood of this observation would be a Poisson distribution, given by:

$$p(\hat{N}|\sigma,\mathcal{L},\epsilon) = \frac{e^{-\sigma\mathcal{L}\epsilon}(\sigma\mathcal{L}\epsilon)^{\hat{N}!}}{\hat{N}!} \tag{9.16}$$

The integrated luminosity $\mathcal{L}$ is measured to be $\hat{\mathcal{L}} = 14.7pb^{-1}$ with a 1σ error of $\Delta\mathcal{L}/\hat{\mathcal{L}} = 5\%$. The total detection efficiency ϵ is estimated from Monte Carlo data, and varies with M from $\hat{\epsilon}(M) = 30 - 40\%$ with a 1σ error of $\Delta\epsilon = 5\%$. I assume that the function which best represents the probability distributions for $\mathcal{L}$ and ϵ is again a gaussian for each of these quantities, given by:

$$p(\mathcal{L}) = \frac{1}{\sqrt{2\pi(\Delta\mathcal{L})}} \exp \frac{-(\mathcal{L}-\hat{\mathcal{L}})^2}{2(\Delta\mathcal{L})^2} \tag{9.17}$$

and

$$p(\epsilon) = \frac{1}{\sqrt{2\pi(\Delta\epsilon)}} \exp \frac{-(\epsilon - \hat{\epsilon})^2}{2(\Delta\epsilon)^2}. \tag{9.18}$$

I have no reason to favor one value of the cross section over another. I assume a uniform probability distribution, given by:

$$p(\sigma) = 1 \tag{9.19}$$

These functions are prior probability distributions, as given in (9.11).

I performed the integrations in (9.14) numerically by six-point Gaussian Quadrature, with the multidimensional integration routine DGMLT in the CERN program library [110]. I begin with $\sigma_{UL} = N/(\mathcal{L}\epsilon)$ and increase σ_{UL} by increments until $CL = 95.01 \pm 0.01\%$. This value σ_{UL} is the upper limit on the cross section at the 95% confidence level. As a cross-check, I also performed the integrations with a Monte Carlo program which I wrote, which fills the sample space by coordinate assignment through random number generation. The results are within 2% of the integral values by Gaussian Quadrature for all data points.

9.4 Confidence Limit Results

The upper limit on the excited quark cross section times the branching ratio to the photon-jet final state is shown in Fig. 9.1 with the theoretical prediction overlayed. The shaded area above the limit is excluded at a confidence level of greater than 95%. The lower limit on the excited quark mass is the mass value where the theory prediction crosses into the non-excuded region. Within the theoretical model (at $\Lambda = M^*$, for mass degenerate u^* and d^*, and using the leading order parton distribution function set CTEQ2L), I find the lower limit on M^* to be 531 GeV/c^2 at the 95% confidence level.

Figure 9.2 shows the theoretical prediction for the cross section with different choices of parton distribution functions. CTEQ2L gives the best global fit to data with leading order theory predictions. CTEQ2M gives the best global fit with next to leading order calculations. CTEQ2MF uses a flatter gluon distribution at small x, while CTEQ2MS uses a singular gluon distribution at small x. This figure shows that the lower limit on the mass varies by $\approx 30\ GeV/c^2$ with different choices of the parton distribution functions. Figure 9.3 shows the theoretical prediction with different choices of the compositeness scale Λ.

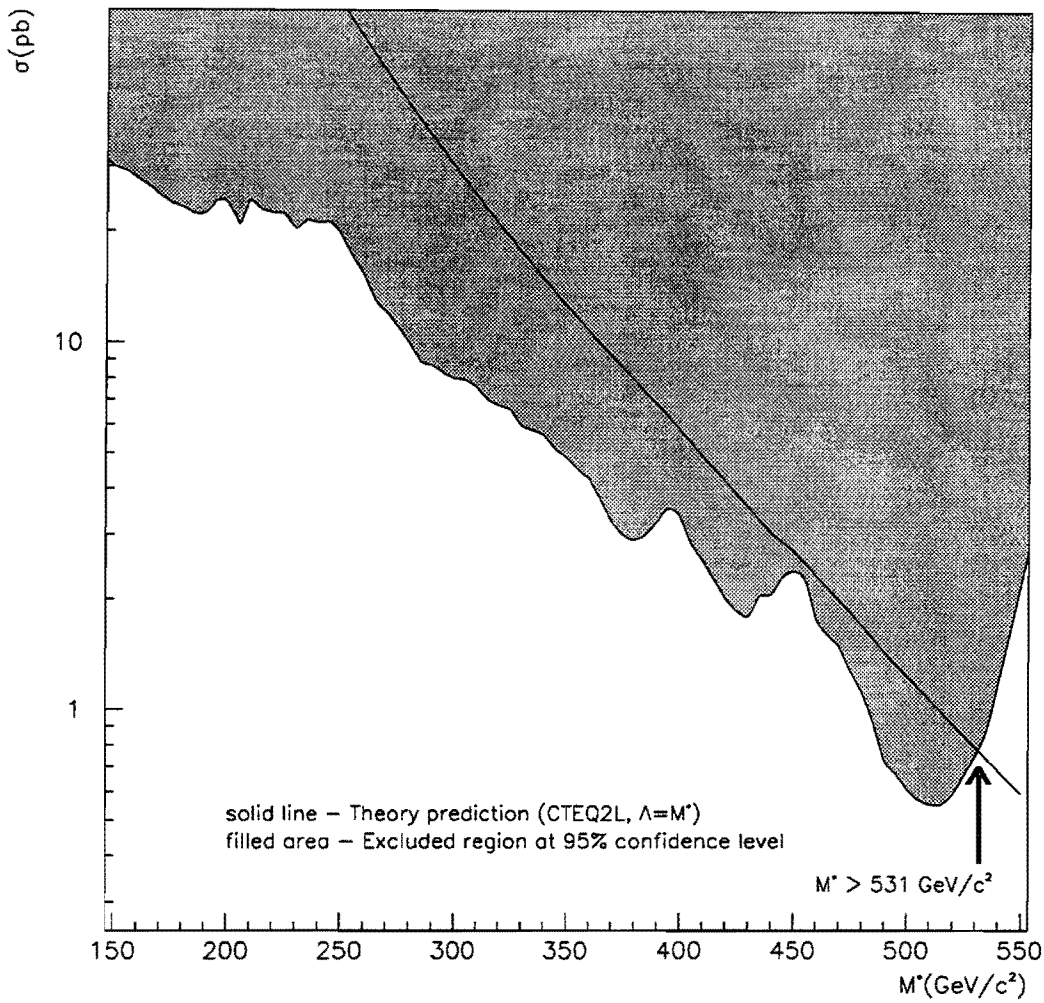

Figure 9.1: The lower boundary of the shaded area is the upper limit on the $Q^* \rightarrow \gamma q$ cross section at the 95% confidence level . The curve intersecting it is the theoretical prediction of Baur *et al.*. The shaded region is all excluded at greater than 95% confidence. The parton distribution functions used in the theory calculation are CTEQ2L.

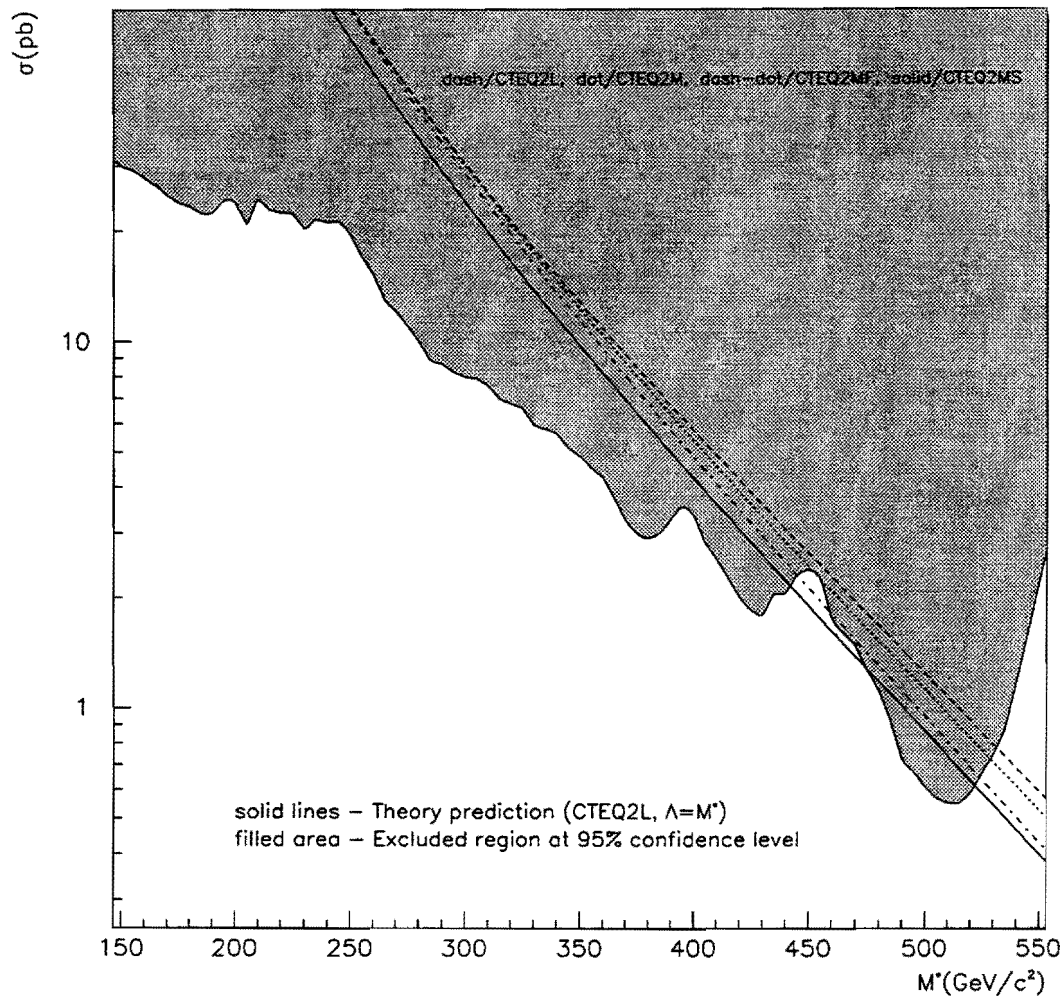

Figure 9.2: The upper limit at the 95% confidence level on the $Q^* \rightarrow \gamma q$ cross section shown with the theoretical prediction calculated with different parton distribution functions, as labeled.

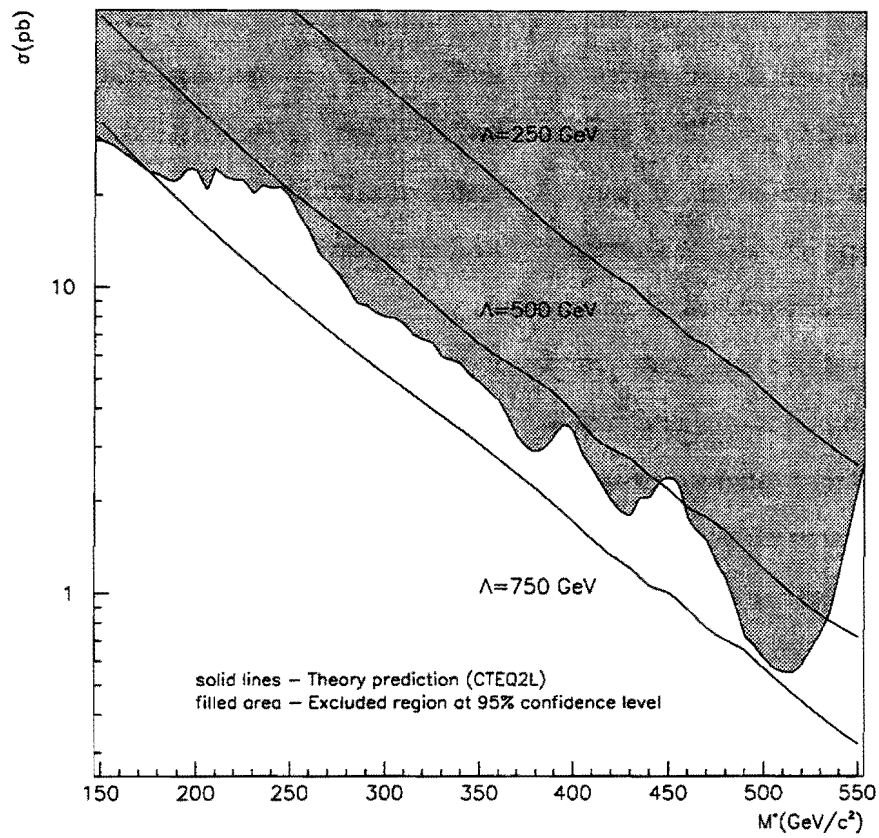

Figure 9.3: The upper limit at the 95% confidence level on the $Q^* \rightarrow \gamma q$ cross section shown with the theoretical prediction at different values of the compositeness scale, $\Lambda = 250, 500, 750$ GeV.

CHAPTER 10
CONCLUSION

This analysis examines the photon-jet invariant mass distribution of photon events produced in $p\bar{p}$ collisions at Fermilab's Tevatron accelerator during the 1992-93 collider run, measured by the DØ detector, representing an integrated luminosity $\mathcal{L} = 14.7pb^{-1}$. The results show excellent agreement with a next-to-leading logarithm calculation of prompt photon production by Owens *et al.* [78]. Other DØ prompt photon measurements presented are all well described by QCD next-to-leading order theoretical calculations.

The collider run just completed has improved statistics by a factor of 5-10. New prompt photon analyses which are in progress at DØ include measurements of the prompt photon cross section at forward rapidity, in the range 1.6-2.5; the diphoton cross section, sensitive to parton k_T; the photon+jet triple differential cross section, sensitive to the parton distribution functions and to next-to-leading order terms; the photon signed angular distribution ($\eta_\gamma \times \frac{\eta_{jet}}{|\eta_{jet}|}$), sensitive to the parton distribution functions; and energy flow studies around the photon and jet, sensitive to fragmentation functions. Plans are in progress to measure the prompt photon cross section at $\sqrt{s} = 600$ GeV, and possibly 1200 GeV also, since cross section ratios at different $\sqrt{s}$ will reduce sensitivity to renormalization and factorization scales.

The photon-jet mass distribution was used in a new particle search for excited quark states, which are a predicted manifestation of quark compositeness. A mass fitting analysis reveals no significant evidence for the process $Q^* \rightarrow \gamma q$, according to predictions of the leading-order model of Baur *et al.*,[14]. A lower limit of 531 GeV/c^2 was established at the 95% confidence level for the mass of excited quark states,

subject to the choices for input parameters used in the theoretical model and to all assumptions made about prior probabilities.

APPENDIX A
INTRODUCTORY THEORETICAL BACKGROUND

This appendix is a summary of information from the sources [111],[112],[113],[114]. For further detail, see these references.

A.1 Symmetries

The mechanisms of physics are intimately related to principles of symmetry. An understanding of observed symmetries leads to predictions about the constituents of matter and physical interactions.

The equations of motion for a system of particles are derived from Lagrange's equation (see [115]).

$$\frac{d}{dt}(\frac{\partial L}{\partial \dot{q}_i}) - \frac{\partial L}{\partial q_i} = 0, \tag{A.1}$$

where q_i are the space coordinates of particles, t is time, $\dot{q}_i = \frac{dq}{dt}$, and the Lagrangian L is given by,

$$L \equiv T - V. \tag{A.2}$$

where T is kinetic energy, and V is potential energy.

Generalizing to a continuous system, discrete particle coordinates $q_i(t)$ are replaced by a "field" $\phi(x)$, which may be described in this context as a system of continuously varying coordinates, expressed as a function of the continuous paramters $x = (\vec{x}, t)$. The Lagrangian is replaced by a Lagrange density $\mathcal{L}$[1] related to the

[1]The symbol $\mathcal{L}$ is also used for "luminosity". The difference may be inferred from context.

Lagrangian by,

$$L = \int d^3x \; \mathcal{L} \tag{A.3}$$

An appropriate choice of $\mathcal{L}$ contains all the information necessary to specify the interactions between the particles of a system.

Invariance of a Lagrangian under continuous field transformations; such as translations, time displacements, and rotation; implies the existence of conserved quantities; such as momentum, energy, and angular momentum. The description of this relation is Noether's theorem.

For example, the QED (Quantum Electrodynamics) Lagrangian which describes the electromagnetic interaction of a charged particle in a field $\psi(x)$ is invariant under a phase transformation

$$\psi(x) \rightarrow e^{i\alpha}\psi(x). \tag{A.4}$$

The family of phase transformations $U(\alpha) \equiv e^{i\alpha}$ forms the unitary symmetry group, $U(1)_{em}$. The invariance of the Lagrangian under an infinitesimal phase translation, $\psi(x) \rightarrow \psi'(x) = (1 + i\alpha)\psi(x)$, is given by:

$$\delta\mathcal{L} = \mathcal{L}(\psi') - \mathcal{L}(\psi) = 0. \tag{A.5}$$

When expanded, this requires

$$\partial_\mu[\frac{\partial\mathcal{L}}{\partial(\partial_\mu\psi)}\psi - \bar{\psi}\frac{\partial\mathcal{L}}{\partial(\partial_\mu\bar{\psi})}] = 0. \tag{A.6}$$

The term in brackets is proportional to $j^\mu_{em}(= \bar{\psi}\gamma^\mu Q\psi)$, the electromagnetic current. Thus, a current is conserved

$$\partial_\mu j^\mu_{em} = 0, \tag{A.7}$$

and electric charge,

$$q = \int d^3x e j^\circ_{em} = e\int d^3x\bar{\psi}\gamma^\circ Q\psi \tag{A.8}$$

is a conserved quantity, from the invariance of $\mathcal{L}$ under $U(1)_{em}$ symmetry. The charge operator Q is said to be the "generator" of $U(1)_{em}$ transformations, with an eigenvalue of $Q = -1$ for the electron.

A.2 Gauges

The symmetry by which $\mathcal{L}$ is invariant under phase transformations requires that the phase α be unmeasurable, and therefore arbitrary. This property is called "global gauge invariance", where gauge is synonymous with phase. More generally, α may vary in space-time, as $\alpha(x)$, and the field ϕ transforms as,

$$\phi \rightarrow e^{i\alpha(x)}\phi. \tag{A.9}$$

The property of invariance under this phase transformation is "local gauge invariance". The relativistic Lagrangian describing a free particle,

$$\mathcal{L} = i\bar{\psi}\gamma^{\mu}\partial_{\mu}\psi - m\bar{\psi}\psi \tag{A.10}$$

is not invariant under a local phase transformation without some form of modification.

A "covariant derivative" D_{μ} must be constructed to preserve the gauge invariance of the Lagrangian.

$$D_{\mu} = \partial_{\mu} - ieA_{\mu} \tag{A.11}$$

The "gauge field" A_{μ} which is introduced transforms as

$$A_{\mu} \rightarrow A_{\mu} + \frac{1}{e}\partial_{\mu}\alpha(x). \tag{A.12}$$

An excitation of the gauge field is manifested as a physical particle, the "quantum" of the field, which is called a gauge boson. In this case, the gauge particle is the photon. A photon field "couples" to particles which have electric charge and mediates the electromagnetic force which acts on them.

Local gauge invariance prohibits the inclusion of a mass term in the kinetic energy part of the Lagrangian, so the gauge particle must be massless. Mass causes unrenormalizable divergences in the integrals which predict measurable physical

quantities, such as the cross section and decay rate. Such calculations are the goal of any meaningful theory. This property becomes a problem when interpreting the $SU(2)$ symmetry of the weak force, which is mediated by very massive gauge bosons.

A.3 Spontaneous Symmetry Breaking

To generate mass, the symmetry of a Lagrangian must be spontaneously broken. As an example, consider the Lagrangian for a self-interacting real scalar field ϕ.

$$\mathcal{L} = \frac{1}{2}(\partial_\mu\phi)(\partial^\mu\phi) - V(\phi) \tag{A.13}$$

$$V(\phi) = (\frac{1}{2}\mu^2\phi^2 + \frac{1}{4}\lambda\phi^4) \tag{A.14}$$

The potential energy is shown in Fig. A.1. The solution where $\mu^2 > 0$ corresponds to exact symmetry. The vacuum expectation value for the field is $\langle\phi\rangle = 0$. If $\mu^2 < 0$, then the potential has two minima at $\langle\phi\rangle = \pm v$, where $v = \sqrt{-\mu^2/\lambda}$. The Lagrangian is rewritten in terms of a new field, centered at one of the minima,

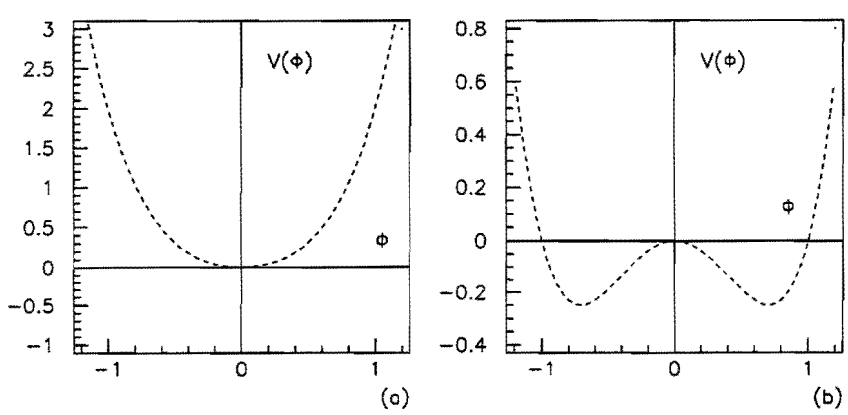

Figure A.1: $V(\phi) = \frac{1}{2}\mu^2\phi^2 + \frac{1}{4}\lambda\phi^4$ for (a) $\mu^2 > 0$ and (b) $\mu^2 < 0$

$\phi'(x) = \phi(x) + v$. A perturbative expansion of the new Lagrangian about the minimum reveals that the mass terms have the correct sign. The broken symmetry has generated a massive scalar field ϕ' corresponding to quantum fluctuations about the minimum potential.

A.4 The Higgs Mechanism

The same symmetry breaking technique may be applied to a complex scalar field $\phi = \frac{1}{\sqrt{2}}(\phi_1 + i\phi_2)$, which is described by a Lagrangian that has a U(1) global gauge symmetry. For the $\mu^2 < 0$ solution, a circle of infinitely many degenerate minima is found for $V(\phi) < 0$ in the ϕ_1, ϕ_2 plane. A problem arises, because in addition to generating a massive gauge field, an unwanted massless scalar field is produced, corresponding to "orbital" vacuum excitations in the equipotential well of minima. The field is massless because there is no restoring force to this mode. The quantum of this field is called a Goldstone boson. Massless scalar particles have not been experimentally observed.

To alleviate this situation, a gauge is chosen which introduces a real scalar field $h(x)$. Rather than the transformations of (A.9) and (A.12), we substitute

$$\phi \rightarrow \sqrt{\frac{1}{2}}(v + h(x))e^{i\theta(x)/v}, \tag{A.15}$$

and

$$A_\mu \rightarrow A_\mu + \frac{1}{ev}\partial_\mu \theta \tag{A.16}$$

With this choice of gauge, the Lagrangian contains a vector gauge boson which interacts with a massive scalar field $h(x)$. The degree of freedom which produced the Goldstone boson becomes the longitudinal polarization of the gauge particle. This is the "Higgs mechanism".

A.5 The Standard Model

In the framework of elementary particle physics, the symmetry group and the Lagrangian which describes the interactions of the most fundamental particles is $SU(2) \times U(1) \times SU(3)$. The description of particle interactions provided by this Lagrangian, with spontaneous breaking of the $SU(2) \times U(1)$ symmetry as described, is called the "Standard Model".

A.5.1 The Electroweak Sector

The electromagnetic and weak interactions are unified in the $SU(2) \times U(1)$ symmetry group which describes "electroweak" interactions. The generators of the group $SU(2)$ are the components of weak isospin T, and the conserved quantum numbers are $T = \frac{1}{2}$ and $T_3 = \pm\frac{1}{2}$. The generator of $U(1)$ is weak hypercharge Y, defined by its relation to electric charge Q (the generator of $U(1)_{em}$),

$$Q = T^3 + \frac{1}{2}Y. \tag{A.17}$$

The gauge group contains an isotriplet of vector fields W^a_μ $(a = 1, 2, 3)$ which couple with strength g to the weak isospin current J^a_μ, and a single vector field B_μ which couples with strength $g'/2$ to the hypercharge current j^Y_μ. The linear combination of fields

$$W^\pm_\mu = \sqrt{\frac{1}{2}}(W^1_\mu \mp iW^2_\mu) \tag{A.18}$$

have quanta $W^\pm$, the massive gauge bosons which mediate charged current interactions. The SU(2) symmetry group is non-Abelian, meaning that its generators do not commute. A result of the non-Abelian nature of the group is that the gauge particles are self-coupling. A mixing of W^3_μ and B_μ produces the mass eigenstates

$$A_\mu = B_\mu \cos\theta_W + W^3_\mu \sin\theta_W \qquad (massless) \tag{A.19}$$

$$Z_\mu = -B_\mu \sin\theta_W + W^3_\mu \cos\theta_W \qquad (massive) \tag{A.20}$$

where θ_W is the Weinberg angle (determined by experiment). The quantum of A_μ is the photon, which mediates electromagnetic current (j_μ^{em}) interactions, and the quantum of Z_μ is the Z°, which mediates weak neutral current (J_μ^{NC}) interactions.

The electroweak neutral current interaction is given by,

$$-igJ_\mu^3(W^3)^\mu - i\frac{g'}{2}j_\mu^Y B^\mu = -i(g\sin\theta_W J_\mu^3 + g'\cos\theta_W\frac{j_\mu^Y}{2})A^\mu - i(g\cos\theta_W J_\mu^3 - g'\sin\theta_W\frac{j_\mu^Y}{2})Z^\mu, \tag{A.21}$$

where the first term is $-ie(j^{em})^\mu)A_\mu$, the electromagnetic interaction. The electromagnetic current is related to the weak isospin and weak hypercharge currents by,

$$j_\mu^{em} = J_\mu^3 + \frac{1}{2}j_\mu^Y. \tag{A.22}$$

and the coupling strengths are related by,

$$g\sin\theta_W = g'\cos\theta_W = e \tag{A.23}$$

The electroweak neutral current (J_μ^{NC}) is given by,

$$J_\mu^{NC} = J_\mu^3 - \sin^2\theta_W j_\mu^{em} \tag{A.24}$$

The Higgs mechanism is incorporated into $SU(2)\times U(1)$ symmetry breaking to allow massive vector gauge particles without unwanted Goldstone bosons. An extra result of the Higgs mechanism is the introduction of a massive scalar particle H°.

A.5.2 The Strong Interaction (QCD)

The generators of $SU(3)$ may be represented by the Gell-Mann matrices, λ_a (a=1-8). The conserved quantities in this symmetry group are three charges; which are called "color" charges red, green, and blue; in analogy with the three primary colors of light. The Lagrangian which describes color interactions is given by,

$$\mathcal{L} = \bar{q}_j(i\gamma^\mu\partial_\mu - m)q_j, \tag{A.25}$$

Leptons	e electron	μ muon	τ tau
neutrinos	ν_e	ν_μ	ν_τ
Quarks	u up	c charm	t top
	d down	s strange	b bottom
Gauge Bosons	g gluon	strong nuclear force	
	γ photon	electromagnetic force	
	$W^\pm$ and Z	weak force	
	H° Higgs		

Table A.1: The particles of the Standard Model.

where $q_{1,2,3}$ are the fields which generate color. To preserve local gauge invariance of the Lagrangian, eight gauge fields are introduced, G^a_μ (a=1-8). The quanta of the gauge fields are massless particles called gluons, which couple to particles with color charge and mediate the "strong" interaction between them. The $SU(3)$ group is non-Abelian, so the gluons are self-coupling.

The fundamental particles included in the Standard Model are listed in Table A.1. These particles combine to form all other particles in nature. For each particle, there is a complementary antiparticle with opposite quantum numbers, although some particles are their own antiparticle. The most recent of these particles to be discovered is the top quark, announced on March 2, 1995 in independent observations by the CDF and DØ experiments at Fermilab. The tau neutrino and Higgs boson have yet to be directly observed. The particles interact with fields of the electromagnetic, weak and strong forces, each of which is mediated by one or more gauge bosons. The last remaining force in nature, gravity, is of negligible strength at the length scale of experimental particle physics.

Combinations of three quarks in a bound state form baryons, such as the proton and neutron. Combinations of a quark and antiquark form mesons. Baryons and mesons are collectively called hadrons, which may interact by the strong nuclear force. The rule which describes quark combinatorics in these particles is that all free particle states must be unchanged by rotations in color space, i.e. they are "colorless" combinations. No exceptions to this rule have been observed. Leptons do not interact strongly. Charged leptons interact by the electromagnetic or weak force. The neutrinos, or neutral leptons, interact weakly. The photon, $W^{\pm}$, Z°, and gluons are all gauge bosons of spin 1. The Higgs boson has spin-0.

Notice in Table A.1 that there are three "generations" of quarks and leptons in the Standard Model. Each successive generation's particles are more massive than the preceding. It is necessary to have an equal number of lepton and quark weak isospin doublets to preserve the renormalizability of the gauge theory of weak interactions. Most of the matter in the universe is made from the particles in the first generation, which are the lightest. The u and d quarks make up protons and neutrons, of which the nucleus of an atom is composed. The proton and neutron are almost degenerate in mass, and are loosely considered as two isospin states of the same nucleon, forming the SU(2) symmetry group of isospin.

BIBLIOGRAPHY

[1] J. Thompson, "Introduction to Colliding Beams at Fermilab", DØ internal note #2367, released as FERMILAB-TM-1909.

[2] D.H. Perkins, *Introduction to High Energy Physics*, Third Edition, (Addison-Wesley, 1987)ch. 1.

[3] V.D. Barger and R.J.N. Phillips *Collider Physics*, (Addison-Wesley, 1987)ch. 1.

[4] F. Halzen and A. Martin, *Quarks and Leptons: An Introductory Course in Modern Particle Physics*, (John Wiley & Sons, New York, 1984)ch. 1.

[5] P.D.B. Collins, A.D. Martin, and E.J. Squires, *Particle Physics and Cosmology*, (John Wiley & Sons, New York, 1989)ch. 9.

[6] *The Random House Dictionary of the English Language*, (Random House, 1980).

[7] R.P. Feynman, Phys. Rev. Lett. **23**, (1969)1415.

[8] R.P. Feynman *et al.*, *High Energy Collisions, Third International Conference held at SUNY Stony Brook, New York*, (Gordon and Breach, New York, 1969)237.

[9] M. Fritzsch, M. Gell-Mann, and H. Leutwyler, "Advantages of the Color Octed Gluon Picture", Phys. Lett. **47B**, (1973)365.

[10] Particle Data Group, *Particles and Fields*, Phys. Rev. D, (1992)III.54.

[11] A. De Rujula, L. Maiani, and R. Petronzio, "Search for Excited Quarks", Phys. Lett. **140B**, (1984)253.

[12] J. Kühn and P. Zerwas, "Excited Quarks and Leptons", Phys. Lett. **147B**, (1984)189.

[13] U. Baur, I. Hinchliffe, and D. Zeppenfeld, "Excited Quark Production at Hadron Colliders", Int. J. Mod. Phys. A, Vol. 2, No. 4, (1987)1285.

[14] U. Baur, M. Spira, and P.M. Zerwas, "Excited-Quark and -Lepton Production at Hadron Colliders", Phys. Rev. **D42**, (1990)815.

[15] F. Abe *et al.*, "Inclusive Jet Cross Section in $\bar{p}p$ Collisions at $\sqrt{s} = 1.8TeV$", Phys. Rev. Lett. **68**, (1992)1104.

[16] The DØ Collaboration, *Design Report, The D0 Collaboration at the Fermilab Antiproton-Proton Collider*, (1984), unpublished.

[17] P. Grannis, "Specifications for the DØ Detector", DØ internal note #560, unpublished.

[18] S. Abachi et al, "The DØ Detector", Nucl. Instr. and Meth. **A338** (1994)184-253.

[19] A.R. Clark, "The DØ Vertex Chamber: Status Report", DØ internal note #776, unpublished.

[20] E. Oltman, "DØ Vertex Drift Chamber Construction and Test Results", DØ internal note #1169, unpublished.

[21] J.F. Detoeuf *et al.*, "The DØ Transition Radiation Detector", Nucl. Inst. and Meth. **A265**, (1988).

[22] J.F. Detoeuf *et al.*, "Status of the Transition Radiation Detector for the DØ Experiment", Nucl. Inst. and Meth. **A279**, (1989).

[23] A. Pluquet, "Extracts from Alain Pluquet's Thesis - Electron Identification with the TRD", DØ internal note #2330, unpublished.

[24] F. Feinstein, *Etude D'un Detecteur a Rayonnement De Transition Pour L'Experience DØ Au FNAL*, PhD Thesis, (1992).

[25] A. Pluquet, *Electron Identification with the TRD*, PhD Thesis, (1993).

[26] F. Sauli, "Principles of Operation of Multiwire Proportional and Drift Chambers", CERN Report 77-09 (1977). Reprinted in T. Ferbel, *Experimental Techniques in High Energy Physics*, (Addison-Wesley, Reading, Mass., 1987).

[27] V.L. Ginzberg and I.M. Frank, IETP 16, (1946)15.

[28] W.W.M. Allison and P.R.S. Wright, "The Physics of Charged Particle Identification: dE/dx, Cerenkov and Transition Radiation", *Formula and Methods in Experimental Data Evaluation, Vol.2: Articles on Physics and Detectors.* ed. R.K. Bock *et al.*, (The European Physical Society, CERN, 1984). Reprinted in T. Ferbel, *Experimental Techniques in High Energy Physics*, (Addison-Wesley, Reading, Mass., 1987).

[29] T. Behnke, *The Central Drift Chamber for the DØ Experiment: Design, Construction, and Test*, PhD Thesis, (1992).

[30] S. Rajagopalan, *The dE/dx Capabilities of the DØ Tracking System*, PhD Thesis, (1992).

[31] D. Pizzuto, *DØ Central Tracking Chamber Performance Studies*, PhD Thesis, (1992).

[32] J. Bantly, *The DØ Detector Forward Drift Chamber Performance and Physics Capability in the 1990 FNAL Testbeam Run*, PhD Thesis, (1992).

[33] Particle Data Group, *Review of Particle Properties*, Phys. Lett. B (1990),III.13-16,22.

[34] M. Paterno, D. Chakraborty, M. Fatyga, "CCEM Module Sampling Fractions and Uniformity of Response", DØ internal note #1375, unpublished.

[35] W.G.D. Dharmaratna, T. Heuring, "CCEM Response vs. η - Test Beam Load 2", DØ internal note #1577, unpublished.

[36] W.G.D. Dharmaratna, "Reconstruction of the Calorimeter Response-Test Beam Load 2", DØ internal note #1731, unpublished.

[37] Q. Zhu, *Measurement of the W Boson Mass in Proton-Antiproton Collisions at s=1.8 TeV*, PhD thesis, (1994)64.

[38] M. DeMarteau, private communication.

[39] N. Graf, "Improvements to the Calorimeter Electron Position Algorithm", DØ internal note #1352, unpublished.

[40] D.H.Perkins, *Introduction to High Energy Physics*: Third Edition, (Addison-Wesley, Reading, Mass., 1987)46.

[41] A. White, "Inter-Cryostat Detector, Part I", DØ internal note #770, unpublished.

[42] T. Geld, *The DØ Intercryostat Detector: Design Considerations, Test Beam Studies, and Initial Performance*, PhD Thesis, (1993).

[43] M.L. Good, W. Guryn, M. Howard, "Massless Gaps for the Central Calorimeter", DØ internal note #635, unpublished.

[44] T. Diehl, "Milestones Passed in CRC II WAMUS Triggering + Tracking" DØ internal note #1365, unpublished.

[45] Institute of High Energy Physics, Serpukhov, "SAMUS: Small Angle Muon Spectrometers", DØ internal note #768, unpublished.

[46] D. Denisov, "Small Angle Muon System for the DØ Detector at Fermilab", DØ internal note #1367, unpublished.

[47] N. Amos *et al.*, "Luminosity Calculations for DØ", DØ internal note #2031, unpublished.

[48] D.H.Perkins, *Introduction to High Energy Physics*: Third Edition, (Addison-Wesley, Reading, Mass., 1987)33.

[49] Perkins, *Introduction to High Energy Physics*: Second Edition, (Addison-Wesley, Reading, Mass., 1982)165-175.

[50] N. Amos *et al.*, "A Luminosity-Independent Measurement of the $\bar{p}p$ Total Cross Section at $\sqrt{s} = 1.8$ TeV",Phys. Lett., **243B**, 158(1990).

[51] F. Abe *et al.*. "Measurement of Small Angle $\bar{p}p$ Elastic Scattering at $\sqrt{s} = 546$ and 1800 GeV", FERMILAB-Pub-93/232-E (1993), submitted to Phys Rev D.

[52] F. Abe *et al.*. "Measurement of $\bar{p}p$ Single Diffractive Dissociation at $\sqrt{s} = 546$ and 1800 GeV", FERMILAB-Pub-93/233-E (1993), submitted to Phys Rev D.

[53] F. Abe *et al.*. "Measurement of the $\bar{p}p$ Total Cross Section at $\sqrt{s} = 546$ and 1800 GeV", FERMILAB-Pub-93/234-E (1993), submitted to Phys Rev D.

[54] F. Nang, private communication.

[55] K. McFarland, "Design and Testing of a Calibration System for the Level-0 Trigger at DØ", DØ internal note #840, unpublished.

[56] R. Partridge, "The Level 0 Trigger", DØ internal note #1218, unpublished.

[57] Particle Data Group, *Particles and Fields*, Phys. Rev. D, (1992)III.84.

[58] M. Abolins, *et al.*, "The Level 1 Calorimeter Trigger for DØ", DØ internal note #706, unpublished.

[59] P. Laurens, "First Level Trigger Data Block Description", DØ internal note #967, unpublished.

[60] J. Linnemann, "Level 2 Filtering", DØ internal note #907, unpublished.

[61] D. Cutts, "DØ Level-2/Data Acquisition in a High Luminosity Environment", DØ internal note #711, unpublished.

[62] P. Bhat, S. Fuess, and H. Prosper, "DØ Analysis Computing Model for Run 1b DACPB Report 1", DØ internal note #1929, unpublished.

[63] S. Youssef, "A Family of Cluster Algorithms", DØ internal note #375, unpublished.

[64] S. Youssef, "Clustering with Local Equivalence Relations", DØ internal note #541, unpublished.

[65] S. Linn and S. Youssef, "Clustering to Improve EM Resolution", DØ internal note #655, unpublished.

[66] T.C. Awes *et al.*, Nucl. Instr. and Meth. **A311**, (1992)130.

[67] N.J. Hadley, "Cone Algorithm for Jet Finding", DØ internal note #904, unpublished.

[68] HBOOK Reference Manual Version 4.20, CERN Program Library entry Y250, (©1993, CERN)17-36.

[69] PAW Reference Manual Version 2.03, CERN Program Library entry Q121, (©1993, CERN).

[70] R. Hirosky, "A Data-based Estimate of Jet Reconstruction Efficiencies", DØ internal note #2369, unpublished.

[71] R. Hirosky, "Jet Efficiencies and Seed Tower Distributions in the DØCone Algorithm", DØ internal note #2405, unpublished.

[72] D. Elvira, G. Blazey, and R. Astur, "A Study of Standard Jet Cuts and their Efficiencies Using DØ Collider Data", DØ internal note #1763, unpublished.

[73] C. Bormann and I. Adam, "Discrimination Between Low Energy Electrons and π^0's Using 'SPREAD"', DØ internal note #2297, unpublished.

[74] R. Englemann *et al.*, Nucl. Instr. and Meth. **A216**, (1983)45.

[75] J. Chiu, D. Kewley, and G. Blazey, "Improvement of Electron Energy Resolution by the Covariance χ^2 Approach", DØ internal note #775, unpublished.

[76] J. Chiu, D. Kewley, and G. Blazey, "Improving Energy Resolution of Calorimeters Using a Covariance Matrix Approach", DØ internal note #914, unpublished.

[77] M. Narain, "Electron Identification in the DØ Detector", DØ internal note #1548A, unpublished.

[78] H. Baer, J. Ohnemus, and J. Owens, FSU-HEP-900214, (1990).

[79] S. Fahey, *Direct Photon Production at* $\sqrt{s} = 1.8$ *TeV*, PhD Thesis, (1995).

[80] P. Rubinov, *The Center-of-Mass Angular Distribution of Direct Photons at* $\sqrt{s} = 1.8$ *TeV Observed with the DØ Detector*, PhD Thesis, (1995).

[81] J. Owens, Rev. Mod. Phys. **Vol. 59, No. 2.**, (1987), p. 494-495.

[82] S.Keller and J. Owens, Phys. Lett. **269B**, (1991), p. 445-449.

[83] S. Linn and C. Shaffer, "The Photon Di-Jet Cross Section", DØ internal note #2507, unpublished.

[84] J. Owens, private communication.

[85] A.G. Frodesen, O. Skjeggestad, and H. Töfte, *Probability and Statistics in Particle Physics*, (Universitetsforlaget, Oslo, Norway, 1979)259.

[86] J.R.Taylor, *An Introduction to Error Analysis*, (University Science Books, 1982)225.

[87] Particle Data Group, *Particles and Fields*, Phys. Rev. D, (1992)III.37.

[88] MINUIT - Function Minimization and Error Analysis. CERN Program Library Entry **D506** (©1992, CERN).

[89] R. Fletcher and M.J.D. Powell, "A Rapidly Converging Descent Method for Minimization", Comput. J. **6**, (1963)163.

[90] W.C. Davidson, "Variance Algorithms for minimization", Comput. J. **10**, (1968)406.

[91] H.U. Bengtsson and T. Sjöstrand, Computer Physics Commun. **46** (1987)43.

[92] T. Sjöstrand, Computer Physics Commun. **39** (1986)347.

[93] T. Sjöstrand and M. Bengtsson, Computer Physics Commun. **43** (1987)367.

[94] CERN Application Software and Databases Group, "GEANT - Detector Description and Simulation Tool", CERN Program Library Long Writeup **W5013**.

[95] A.G. Frodesen, O. Skjeggestad, and H. Töfte, "Probability and Statistics in Particle Physics". (Universitetsforlaget, Oslo, Norway, 1979)424.

[96] F. Abe *et al.*, "Search for Excited Quarks in $p\bar{p}$ Collisions at $\sqrt{s}$=1.8 TeV", FERMILAB-Conf-93/205-E 4(1993).

[97] A.G. Frodesen, O. Skjeggestad, and H. Töfte, "Probability and Statistics in Particle Physics". (Universitetsforlaget, Oslo, Norway, 1979)406.

[98] A.G. Frodesen, O. Skjeggestad, and H. Töfte, *Probability and Statistics in Particle Physics*, (Universitetsforlaget, Oslo, Norway, 1979)24-29.

[99] E.T. Jaynes, *Probability Theory: The Logic of Science*, fragmentary edition of 1995, (©1995, E. Jaynes)418.

[100] R.J. Barlow, "Statistics: A Guide to the Use of Statistical Methods in the Physical Sciences", (John Wiley and Sons, New York, 1989).

[101] W.T. Eadie *et al.*, "Statistical Methods in Experimental Physics", (North-Holland, 1982).

[102] H. Jeffreys, "Theory of Probability",(Clarendon Press, Oxford, 1939).

[103] R.T. Cox, Am. J. Phys. **14**(1946)1.

[104] E.T.Jaynes, "Probability and Statistics",http://www.math.albany.edu.8008/JaynesBook.html

[105] A. Garrett, Ockham's Razor, Physics World (May 1991)39.

[106] H.W. Lewis, Am. J. Phys. **50**(1982)1164.

[107] S. Steenstrup, Am. J. Phys. **52**(1984)1146.

[108] H.W. Lewis, Am. J. Phys. **53**(1985)592.

[109] H.B. Prosper, Am. J. Phys. **61**(1993)1.

[110] K.S. Koelbig, "DGMLT, Gaussian Quadrature for Multiple Integrals", CERN Program Library entry D110, (CERN, submitted 1988).

[111] F. Halzen and A. Martin, *Quarks and Leptons: An Introductory Course in Modern Particle Physics*, (John Wiley & Sons, New York, 1984)ch.12-15.

[112] P.D.B Collins, A.D. Martin, and E.J. Squires, *Particle Physics and Cosmology*, (John Wiley & Sons, New York, 1989)ch.2,3,4.

[113] C. Quigg, *Gauge Theories of the Strong, Weak, and Electromagnetic Interactions*, (Benjamin/Cummings, Menlo Park, California, 1982)66-82.

[114] I.J.R. Aitchison and A.J.G. Hey, *Gauge Theories in Particle Physics*, (Adam Hilger Ltd., Bristol, 1982).

[115] H. Goldstein, *Classical Mechanics*, (Addison-Wesley, 1922)16-21.

BIOGRAPHICAL SKETCH

Robert Wayne Madden

e-mail: madden@fnald0.fnal.gov

World Wide Web personal page: http://d0sgi0.fnal.gov/ ~madden/rmadden.html

Education

1985-1988 Florida Southern College, Lakeland, Florida

Bachelor of Science

Physics

1989-1995 Florida State University, Tallahassee, Florida

Doctor of Philosophy

Physics

DØ Publications

1. S. Abachi *et al.*,"The DØDetector", Nucl. Instr. and Meth. **A338**, 185 (1994).

2. S. Abachi *et al.*,"First Generation Leptoquark Search in $\overline{p}$-p Collisions at $\sqrt{s} = 1.8$ TeV", Phys. Rev. Letters **72**, 965 (1994).

3. S. Abachi *et al.*,"Search for the Top Quark in $\overline{p}$-p Collisions at $\sqrt{s} = 1.8$ TeV", Phys. Rev. Letters **72**, 2138 (1994).

4. S. Abachi *et al.*,"Rapidity Gaps between Jets in $\overline{p}$-p Collisions at $\sqrt{s}$ = 1.8 TeV", Phys. Rev. Letters **72**, 2332 (1994).

5. S. Abachi *et al.*,"Search for High Mass Top Quark Production in $\overline{p}$-p Collisions at $\sqrt{s}$ = 1.8 TeV", Phys. Rev. Letters **74**, 2422 (1995).

6. S. Abachi *et al.*,"Observation of the Top Quark", Phys Rev. Letters **74**, 2632 (1995).

7. S. Abachi *et al.*,"Inclusive μ and b-Quark Production Cross Sections in $p\overline{p}$ Collisions at $\sqrt{s}$ = 1.8 TeV", Phys. Rev. Letters **74**, 3548 (1995).

8. S. Abachi *et al.*,"Search for Squarks and Gluinos in $\overline{p}$-p Collisions at at $\sqrt{s}$ = 1.8 TeV", Phys. Rev. Letters **75** 618, 1995.

9. S. Abachi *et al.*,"Search for W Boson Pair Production in $\overline{p}$-p Collisions at at $\sqrt{s}$ = 1.8 TeV", Phys. Rev. Letters **75**, 1023, 1995.

10. S. Abachi *et al.*,"Measurement of the $ZZ\gamma$ and $Z\gamma\gamma$ Couplings in $\overline{p}$-p Collisions at $\sqrt{s}$ = 1.8 TeV", Phys. Rev. Letters **75**, 1028, 1995.

11. S. Abachi *et al.*,"Measurement of the $WW\gamma$ Gauge Boson Coupling in $\overline{p}$-p Collisions at $\sqrt{s}$ = 1.8 TeV", Phys. Rev. Letters **75**, 1034, 1995.

12. S. Abachi *et al.*,"W and Z Boson Production in $\overline{p}$-p Collisions at $\sqrt{s}$ = 1.8 TeV", Phys. Rev. Letters **75**, 1456 (1995).

13. S. Abachi *et al.*,"A Study of the Strong Coupling Constant Using W + Jets Processes", Phys. Rev. Letters, **75**, 3226 (1995).

14. S. Abachi *et al.*,"Top Quark Search with the DØ1992 – 93 Data Sample", accepted for publication in Phys. Rev. **D** (Nov. 1, 1995).

15. S. Abachi *et al.*,"Transverse Energy Distributions within Jets in $\overline{p}$-p Collisions at 1.8 TeV", Phys. Letters **B357**, 500 (1995).

16. S. Abachi *et al.*,"Search for Heavy W Bosons in 1.8 TeV $p\overline{p}$ Collisions", Phys. Letters **B358**, 405 (1995).

17. S. Abachi *et al.*,"Second Generation Leptoquark Search in $\overline{p}$-p Collisions at 1.8 TeV", accepted for publication in Phys. Rev. Letters.

18. S. Abachi *et al.*,"Studies of Topological Distributions of Inclusive Three- and Four-Jet Events in $p\overline{p}$ Collisions at $\sqrt{s}$= 1800 GeV with the DØDetector", submitted to Phys. Rev. **D**.

19. S. Abachi *et al.*,"Jet Production via Strongly-Interacting Color-Singlet Exchange in $\overline{p}$-p Collisons", submitted to Phys. Rev. Letters.